Doctoral Thesis

Development of a New Monte Carlo Code for High-Fidelity Power Reactor Analysis

Hyunsuk Lee

Department of Nuclear Engineering
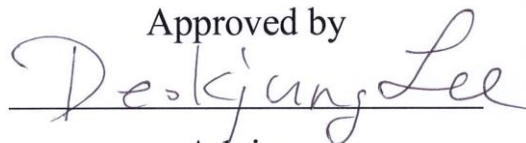
Graduate School of UNIST

2019

Development of a New Monte Carlo Code for Large-Scale Power Reactor Analysis

A dissertation

submitted to the Graduate School of UNIST

in partial fulfillment of the

requirements for the degree of

Doctor of Philosophy

Hyunsuk Lee

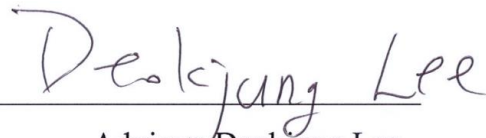12. 04. 2018

Approved by

_____

Advisor

Deokjung Lee

Development of a New Monte Carlo Code for Large-Scale Power Reactor Analysis

Hyunsuk Lee

This certifies that the dissertation of Hyunsuk Lee is approved.
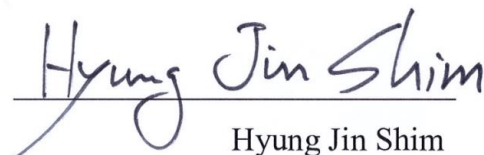
12. 04. 2018

Advisor: Deokjung Lee

Hee Reyoung Kim

Eisung Yoon

Hyun Chul Lee

Hyung Jin Shim

Development of a New Monte Carlo Code for

Large-Scale Power Reactor Analysis

by

Hyunsuk Lee

Abstract

The high-fidelity multiphysics simulation using transport codes are being mainstream in the reactor physics society. Monte Carlo neutron transport code is one of the most promising candidates of neutronics code of multiphysics simulation since it has advantages of using continuous energy cross section and explicit geometry modeling. Most of the methods required for the Monte Carlo multiphysics simulation has been developed and studied well individually. However, Monte Carlo method have not been able to be applied for large-scale multiphysics simulation such as Pressurized Water Reactor analysis because of the limited computing power, memory storage and especially lack of Monte Carlo codes adapted for large-scale power reactor simulation. Development of Monte Carlo multiphysics code is a challenging due to two aspect: implementing various state of the art techniques into one single code system and making it feasible running simulations on practical computing machines.

A new Monte Carlo multiphysics code named MCS was developed for large-scale power reactor analysis. Various state-of-the art techniques were implemented to make it practical tool for multiphysics simulation including thermal hydraulics, depletion, equilibrium xenon, eigenvalue search, on-the-fly cross section generation, hash-indexing, parallel fission bank. The high performance of MCS was achieved and demonstrated. The test result confirmed that the overhead of massive number of tallies is only a one percent up to 13M tally bins, and the parallel efficiency was maintained above 90% up to 1,120 processors when solving power reactor simulation.

The fundamental study of power reactor analysis was performed to decide calculation condition including burnup sensitivity, mesh sensitivity, history sensitivity against pressurized water reactor benchmark problem BEAVRS Cycle 1. Finally, capability of power reactor analysis was demonstrated against BEAVRS Cycle 1 and 2.

Thesis Supervisor: Deokjung Lee

Title: Associated Professor of Nuclear Science and Engineering

Contents

List of Figures

List of Tables

I. Introduction

1.1. Background

The two-step method has been widely used for the reactor analysis thanks to the short computing time with reasonable accuracy. Two-step method has five steps including the library generation steps as shown in Figure I-1. It starts with the reconstruction of cross sections from the evaluated nuclear data file [1]. The data processing code NJOY [2] is typically used in this step to generate the point-wise cross sections. After that the point-wise cross sections are condensed to the multi-group cross sections by using the solution of zero-dimensional slowing down calculation with variation of background cross sections.
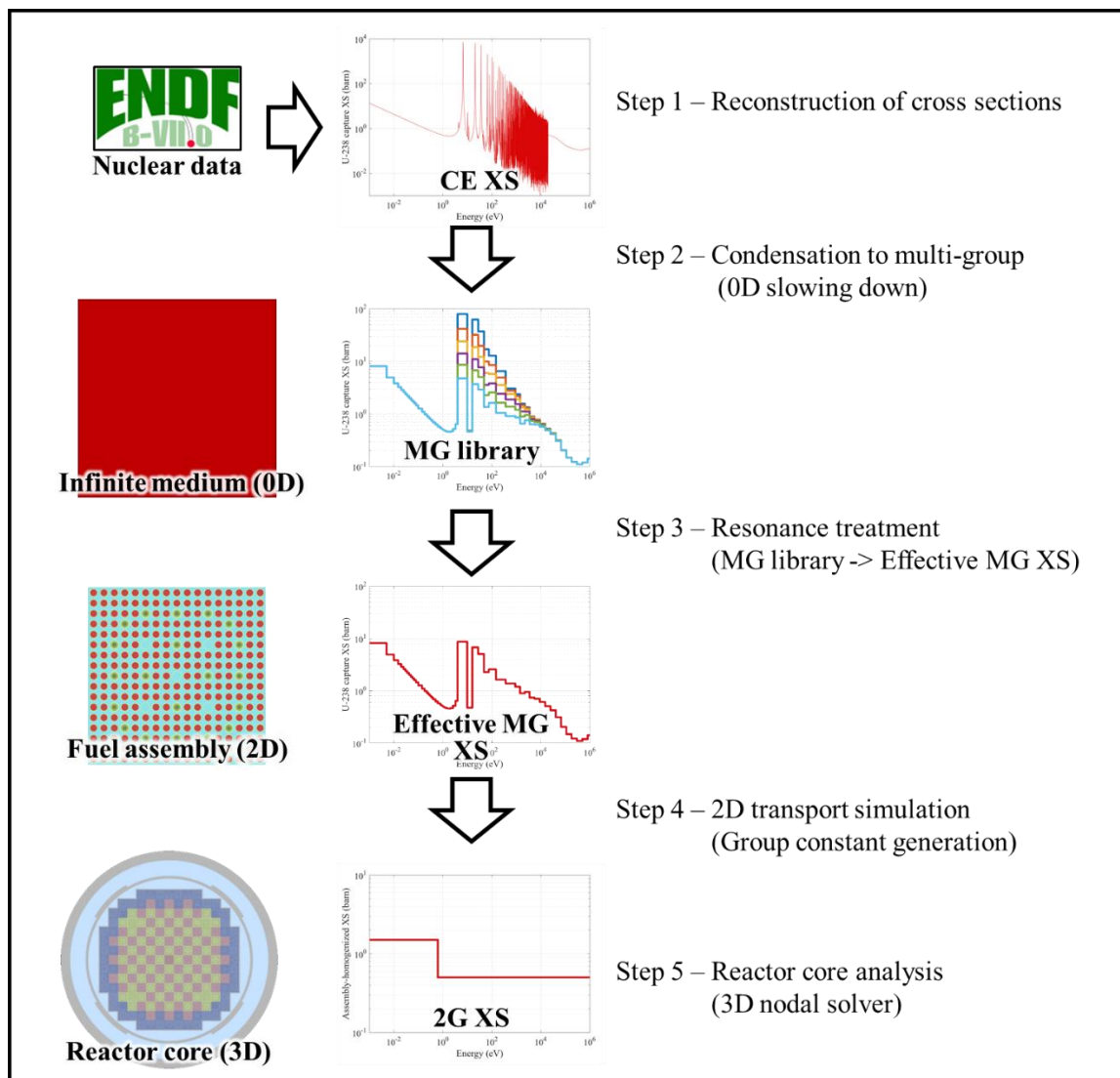
Figure I-1: Conventional two-step method procedure including library generation.

1

Next step is to estimate the effective multi-group cross section for a given problem. The estimated effective cross sections are used in two-dimensional lattice physics code for group constant generation which will be used for core calculation. Finally, three-dimensional reactor core analysis will be conducted by employing nodal diffusion code using group constants from lattice code. This conventional procedure is called two-step method since two neutronics simulations are employed in this scheme: lattice physics code for group constant generation and nodal diffusion code for reactor analysis. Over last decades, reactor physics society was focusing on accuracy enhancement of two-step method.

The high-fidelity multiphysics simulation is becoming a main stream of reactor physics society with the demand of reliable reactor analysis and the increase of computational resources. It was not achievable mission because of lack of computing power and memory storage. It has been only recently started the researches on high-fidelity multiphysics simulation and currently there are many researchers have focused on this area to solve the three-dimensional core geometry directly by adopting transport method as shown in Figure I-2. Unlikely two-step method, there is no homogenization and geometry approximation in three-dimensional transport simulation which makes it more reliable.
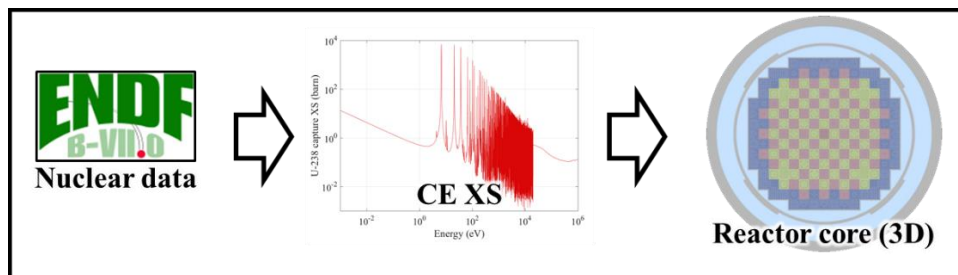
Figure I-2: Three-dimension transport simulation procedure.

The fundamental challenges of high-fidelity multiphysics large-scale reactor simulation is that it requires immense amount of computing time and memory requirement to accurately model the very complex geometry of reactor. According to the challenges of high-fidelity simulations described in the papers [3][4][5], it requires 4 Tera bytes memory only for the burnup related variables including isotopic number density, reaction rates as shown in Table I-1. In addition to the memory issue, it requires tremendous computing time to satisfy the convergence criteria of the solution.

The Consortium for the Advanced Simulation of Light water reactors (CASL) [6] project team leads the high-fidelity simulation area under support of Department of Energy (EOC). At the present time, they have a lot of progress on multiphysics simulation with deterministic transport solver MPACT [7][8][9].

2

Table I-1: Memory Requirement for LWR Burnup Simulation.

Number of Fuel Pins	~50,000
Axial Mesh	~400
Radial Mesh	~10
Number of Nuclides	~300
Number of Reaction Types	~9
Data Type	8 bytes
Memory Requirement	~4.32 TB

At the same time, there have been efforts to apply Monte Carlo method on multiphysics simulation. Much research has been conducted on techniques essential for multiphysics simulation, and most of the issues have already been solved. The remaining issue of Monte Carlo multiphysics simulation is to develop Monte Carlo code combining all the features and make it feasible running on practical work station.

There are many excellent Monte Carlo codes used widely for various purpose such as MCNP [10], Serpent [11], McCARD [12], and OpenMC [13]. However, there was no Monte Carlo code able to perform power reactor simulation practically at the time when we started this research. Thus, we have decided to develop a new Monte Carlo code named MCS targeting large-scale power reactor simulation since 2013 [14]. In 2017, we have published the first solution of BEAVRS benchmark considering cell-wise burnup and thermal hydraulics feedbacks [15].

1.2.   Objective of Thesis

The target of this thesis is development of Monte Carlo multiphysics simulation. The objectives of this thesis are as below:

1. Development of a new Monte Carlo code MCS
2. Demonstration of power reactor simulation capability
3. Sensitivity study of power reactor simulation

In section II, general features of a new Monte Carlo code MCS is described. The developed code has all common features required for the neutronics transport simulation, and it is tested against several benchmark cases. The parallel efficiency and tally efficiency are also presented in this section.

In section III, the inter-cycle correlation of Monte Carlo simulation for high dominance problem is studied. The inter-cycle correlation breaks the assumption of central limit theorem leading the under estimation of statistical uncertainty. The model to estimate the variance bias depending on tally batch size is derived, and numerical tests is performed on large-scale reactor benchmark.

In section IV, the feedbacks required for the power reactor simulation are discussed: depletion, thermal hydraulics feedback, on-the-fly temperature feedback, and critical boron search. The depletion capability is implemented by adopting CRAM method. In addition to the depletion capability, equilibrium xenon feedback capability is studied to prevent the unphysical oscillation induced by the statistical uncertainty of xenon number density. The thermal hydraulics feedback function is implemented by using closed channel code TH1D. The thermal hydraulics feedback is tested against VERA benchmark hot full power assembly problem comparing the solution of MPACT and MC21.

In section V, the large-scale power reactor simulation is studied. The sensitivity study is performed to decide calculation condition including burnup step, mesh structure for feedbacks. The variance overestimation is also studied induced by multiphysics feedback. Finally, the accuracy of MCS is tested against BEAVRS benchmark by comparing measured data and two step code STREAM/RAST-K.

II. The MCS Monte Carlo Code

2.1. Transport Equation

MCS solves time-independent Boltzmann neutron transport equation which can be written as follows [16]:

$$T\Phi = \frac{1}{k}F\Phi \ , \tag{II.1}$$

$$
\begin{aligned}
T &= \mathbf{\Omega}\cdot\nabla\Phi(\mathbf{r},E,\mathbf{\Omega}) + \Sigma_t(\mathbf{r},E)\Phi(\mathbf{r},E,\mathbf{\Omega}) \\
&\quad - \int dE'\int d\mathbf{\Omega}'\Sigma_s(\mathbf{r},E'\to E,\mathbf{\Omega}'\to\mathbf{\Omega})\Phi(\mathbf{r},E',\mathbf{\Omega}') \ ,
\end{aligned}
\tag{II.2}
$$

$$F = \frac{1}{4\pi}\frac{\chi(\mathbf{r},E)}{k}\int dE'\int d\mathbf{\Omega}\,\nu(\mathbf{r},E')\Sigma_f(\mathbf{r},E')\Phi(\mathbf{r},E',\mathbf{\Omega}) \ , \tag{II.3}$$

where $\Phi(\mathbf{r},E,\mathbf{\Omega})$ is the angular flux, $\Sigma_t(\mathbf{r},E)$ is the total cross section, $\Sigma_f(\mathbf{r},E)$ is the fission cross section, $\nu(\mathbf{r},E')$ is the average number of neutron production per fissions, $\chi(\mathbf{r},E)$ is the fission spectrum, $\Sigma_s(\mathbf{r},E'\to E,\mathbf{\Omega}\to\mathbf{\Omega}')$ is the scattering cross section, and k is the multiplication factor.

The Boltzmann equation in (II.1) can be re-written as following by multiplying FT^{-1}

$$S = \frac{1}{k}HS \ , \tag{II.4}$$

$$S = F\Phi \ , \tag{II.5}$$

$$H = FT^{-1} \ , \tag{II.6}$$

where S is the fission source density and H is fission matrix. The fission source density at cycle i can be calculated with following equation

$$S^i = \frac{1}{k^{i-1}}HS^{i-1} \ . \tag{II.7}$$

2.2. Program Flow

MCS reads the input file and initialize the problem including data structure of geometry, materials, tallies, cross sections, depletion. After initialization, it performs criticality simulation as following steps described in the Figure II-1.

1. Sample initial neutron or restore neutron from fission bank.
2. Performs particle transport repeatedly until finish tracking N (number of histories) particles.
3. Save the tally result (sum and sum^2)to estimate the average and standard deviation.
4. Repeat the steps 1-2 during inactive cycles.
5. Repeat the steps 1-3 during active cycles.
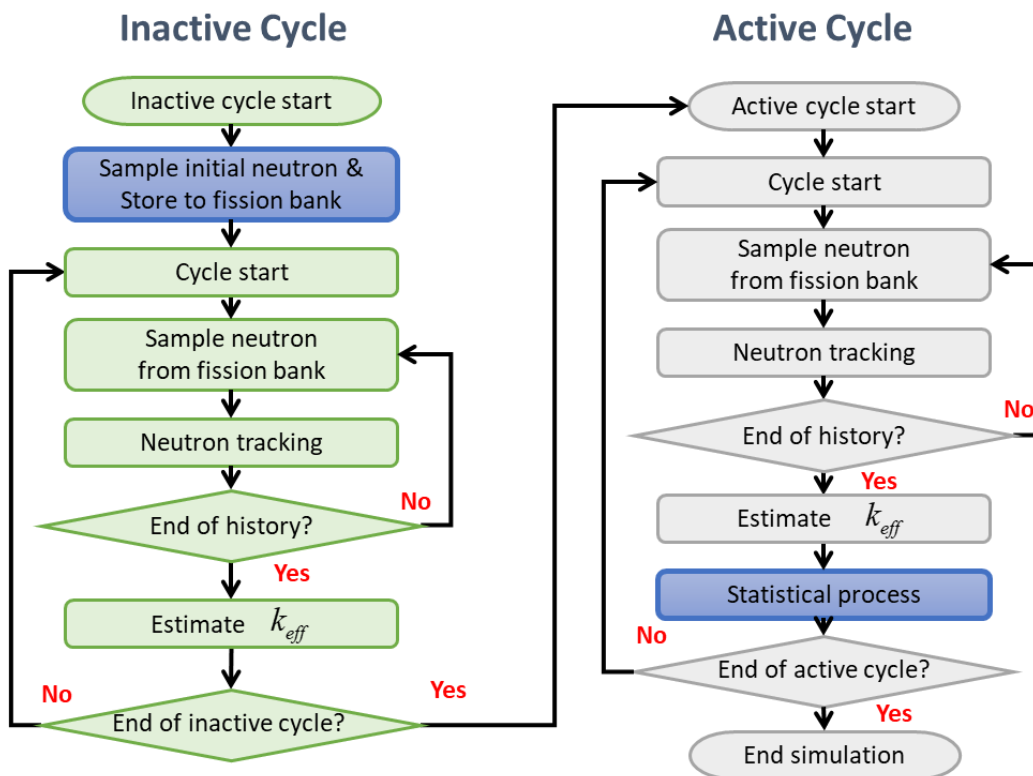
Figure II-1: Program flow of MCS criticality simulation.

Particle transport is performed one at a time in any case as following steps:

1. Sample the particle information including position, direction, energy, weight, time.
2. Initialize the random number seed.
3. Search the cell index where the particle is positioned.
4. Calculates the cross sections of material where the particle is positioned.

5. Sample the distance to collision:

The distance to the next collision is sampled as shown in Figure II-2 with macro total cross section Σ_t by following equation:

$$d_{col} = -\frac{\ln(\xi)}{\Sigma_t} \quad , \tag{II.8}$$

where ξ is pseudo-random number sampled from uniform distribution on [0,1].
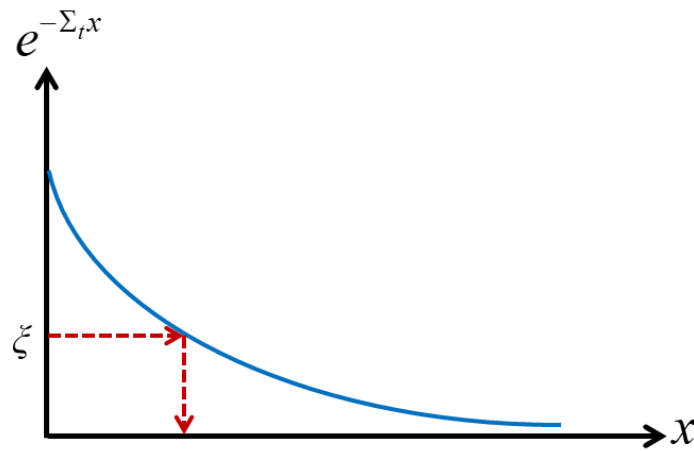
Figure II-2: Sampling distance to collision.

6. Calculate distance to nearest surface d_{sur}.
7. If $d_{col} > d_{sur}$ as shown in Figure II-3, move particle position to the surface boundary and repeat the procedure from step 3.
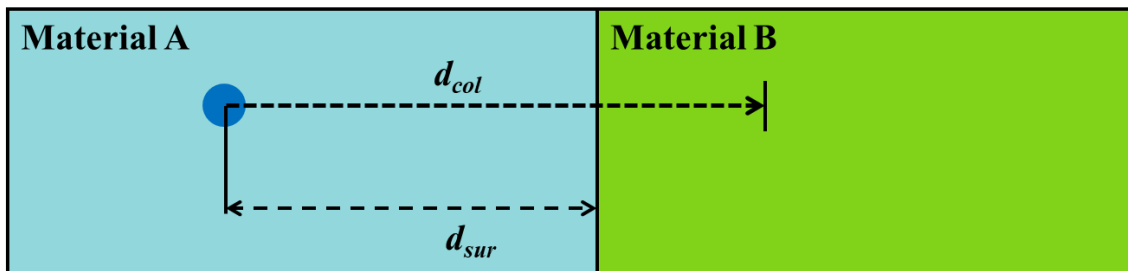
Figure II-3: Geometry tracking when $d_{col} > d_{sur}$.

8. If $d_{col} < d_{sur}$ as shown in Figure II-4, move particle position to the collision site and proceed the collision simulation.

7
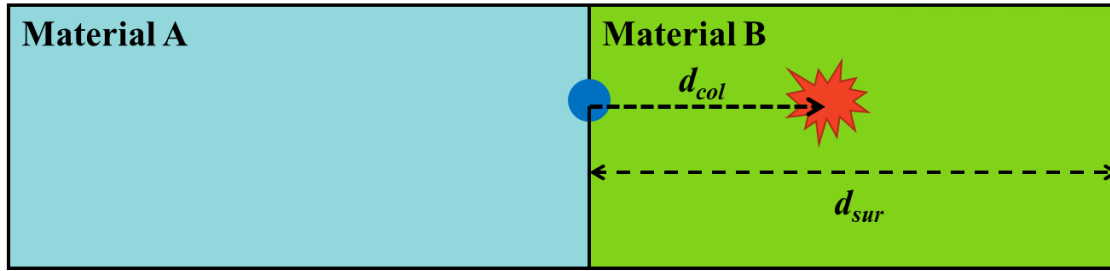
Figure II-4: Geometry tracking when $d_{col} < d_{sur}$.

9. Once the collision is decided, the collision nuclide is sampled with the probability as shown in Eq. (II.9) proportional to the macro total cross section of each nuclide i

$$P(i) = \frac{\Sigma_{t,i}}{\Sigma_t} \quad , \tag{II.9}$$

10. Once the nuclide is sampled, the reaction type x is sampled with the probability proportional to the micro cross sections of x as shown in Eq. (II.10)

$$P(x) = \frac{\sigma_x}{\sigma_t} \quad , \tag{II.10}$$

11. If the scattering reaction is decided, sample the outgoing energy and direction and repeat from the step 4. If absorption reaction is decided, terminate the particle tracking. If fission reaction is decided, save the fission neutron information into fission bank and terminate the particle tracking.

12. Repeat the steps from 1-11 until finish tracking all the particles.

2.3. Pseudo-Random Number Generation

The pseudo-random number generation algorithm Linear Congruential Generator (LCG) is adopted in MCS. The LCG starts with the initial random seed ξ_0, and calculates the sequence of random numbers as following equation:

$$\xi_{i+1} = g\xi_i + c \mod M \quad , \tag{II.11}$$

$$rn_{i+1} = \frac{\xi_{i+1}}{M} \quad , \tag{II.12}$$

where g, c, and M are constants. The randomness and period of random number generator is depending on those constants. Thus, the constants must be chosen very carefully, and the randomness must be tested. The verified constants which are a default constant in MCNP is adopted in MCS: $g=5^{19}$, $\xi_0=5^{19}$, $c=0$, and $M=2^{48}$ [17]. In addition to the randomness of pseudo-random number, it is important to be able to skip the random number sequence for the reproducibility in a parallel simulation. The number of skip numbers is called stride, and the stride value used in MCS is 152,917. The random number seed k step ahead can be calculated as Eq. (II.13) [18]:

$$\xi_{i+1} = g^k \cdot \xi_0 + c \cdot \frac{g^k - 1}{g - 1} \mod M \quad . \tag{II.13}$$

2.4. Geometry

MCS employs constructive solid geometry (CSG) to build arbitrarily complex geometry. In a CSG system, any type of geometry can be defined by bounding surfaces that can be defined in equation. For example, the sphere surface centered at (x_0, y_0, z_0) with radius R can be defined in equation as

$$(x - x_0)^2 + (y - y_0)^2 + (z - z_0)^2 = R^2 \ . \tag{II.14}$$

The positive or negative space shown in Figure II-5 can be defined with surface by assigning sign. The positive space is where the $f(x,y,z)$ is positive, and the negative space is where it is negative

$$f(x, y, z) = (x - x_0)^2 + (y - y_0)^2 + (z - z_0)^2 - R^2 \ . \tag{II.15}$$
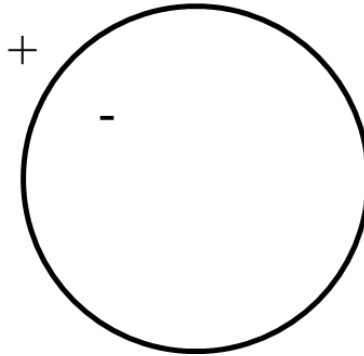
Figure II-5: Example of sphere spaces.

MCS supports universe-based geometry modeling like MCNP. This function helps users to model the repeated structure such as pin and assembly in the pressurized water reactor. Three types of geometry definitions are available in MCS:

- Cell: cell is constructed with the surface defining single component. The cell can be filled with material, universe, or lattice.
- Universe: universe is a set of cells. The universe is constructed with multiple number of cells. The universe must fill the cell to be exist on the geometry model. The universe can fill the cell repeatedly just like the material.
- Lattice: lattice is a set of universes in a regular pattern such as rectangular or hexagonal array.

Figure II-6 shows the hierarchy structure of reactor core geometry. Pin is a universe composed of fuel, gap, cladding, and water cells. The pin universe is repeatedly used to construct assembly lattice. Finally, the assembly lattice is used to construct the core geometry.
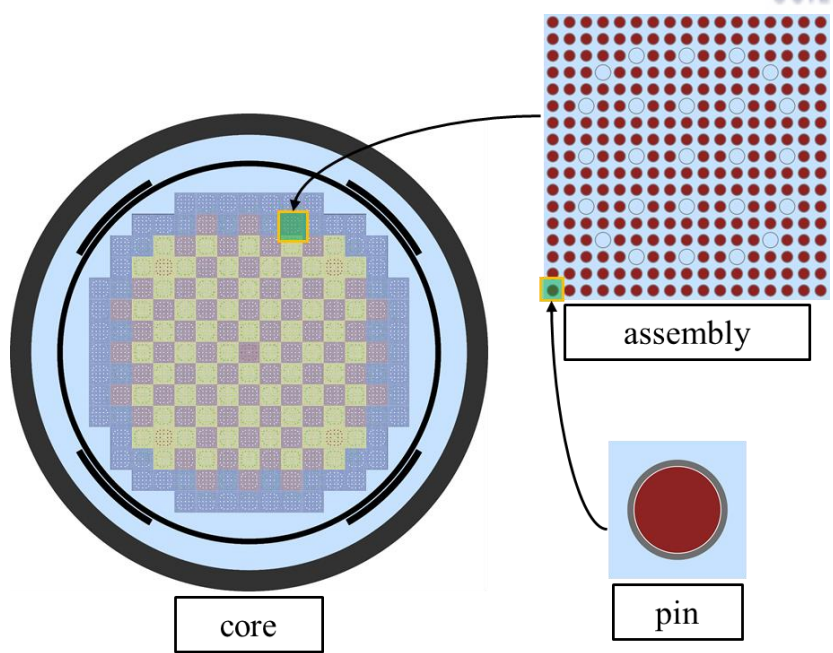
Figure II-6: Hierarchy structure of reactor core geometry.

2.5. Nuclear Physics

MCS can simulate the neutron energies ranging 10^{-11} MeV to 20 MeV. The data governing the neutron-nuclei interaction can be found as ENDF format file in the nuclear data libraries [19]. To be used in MCS, the ENDF format file data is processed first by the nuclear data processing code NJOY [20] into the ACE format files. ACE format file contains many data including cross sections, fission energy spectrum, energy distribution of secondary particle, angle distribution of secondary particle, average number of fission neutrons.

MCS can treat all the common nuclear physics including fission reaction, (*n,xn*) scattering, disappearance reactions, elastic scattering, and inelastic scattering reactions. Following functions are implemented to sample the energy and angle of secondary neutron [21]:

- Sampling angle from isotropic angle distribution
- Sampling angle from equiprobable angle bin distribution
- Sampling angle from tabular angular distribution
- ACE law 1 – tabular equiprobable energy bins
- ACE law 3 – inelastic level scattering
- ACE law 4 – continuous tabular distribution
- ACE law 7 – Maxwell fission spectrum
- ACE law 9 – Evaporation spectrum
- ACE law 11 – Energy-dependent Watt spectrum
- ACE law 44 – Kalbach-Mann correlated scattering
- ACE law 61 – correlated energy and angle distribution
- ACE law 66 – n-body phase space distribution

Data in ACE file is tabulated over relative energy which is depending on the velocity of neutron and velocity of target nuclei. If the neutron energy is relatively large enough to ignore the energy of target nucleus, MCS uses the energy of neutron as relative energy, and assume target at rest. However, the motion of target must be considered if the energy of neutron of comparable with it of target. MCS uses the free-gas approximation if the neutron energy is less than 400kT or the target is ^{1}H, and uses Fast Effective Scattering Kernel [22] or Doppler Broadening Rejection Correction [23] methods if the energy is in range of 0.4eV to 210KeV and the atomic weight of target is larger than 200. In addition, MCS uses $S(\alpha,\beta)$ data for bound scattering in thermal range. For the unresolved energy range, MCS uses probability table to consider the self-shielding effect [24].

2.6. Tallies

The tally capability in MCS is expressed in Eq. (II.16):

$$R = \int_r dr \int_\Omega d\Omega \int_E dE F(r,\Omega,E) Q(r,\Omega,E) \psi(r,\Omega,E) \ , \qquad \text{(II.16)}$$

where W is the total weight of neutron, w_j is the weight of neutron, F is the filter, Q is the scoring quantity.

$$R = \frac{1}{W} \sum_{Event} w_j F(r,\Omega,E) Q(r,\Omega,E) \ . \qquad \text{(II.17)}$$

For criticality simulations, MCS tallies the following essential global parameters by default: Shannon entropy calculated from the cell-wise fission source distribution, total power, core average flux, leakage, and k_{eff} values as given by the collision estimator, track-length estimator and absorption estimator. User can also specify how and what to tally using the following input options: scoring quantity, estimator, energy bin, time bin, filter, mesh and indices.

2.7. Convergence Check

If the fission source distribution is not converged, the solution can be biased. That is why Monte Carlo codes has inactive cycle for the source convergence. Therefore, enough number of inactive cycles must be used, and the convergence of fission source must be checked. The global parameter such as k_{eff} converges faster than the fission source distribution, and the fission source distribution is hard to be checked. MCS calculates the Shannon entropy [25] and center of mass by default to check source convergence. Shannon entropy is single value represent the distribution and the center of mass is center position of fission neutrons. Both quantities are calculated with the fission neutron sites.

MCS uses the fission source distribution of cells to calculate the Shannon entropy H as following:

$$S_i = \frac{\text{Number of source in cell } i}{\text{Total number of fission sources}} \quad , \tag{II.18}$$

$$H = -\sum_{i=1}^{N} S_i \log_2 S_i \quad , \tag{II.19}$$

where N is the number of cells.

The center of neutron site (x_c, y_c, z_c) can be calculated with the position of all neutrons stored in fission bank:

$$\left(x_c, y_c, z_c\right) = \frac{1}{N}\sum_{i=1}^{N}\left(x_i, y_i, z_i\right) \quad . \tag{II.20}$$

where (x_i, y_i, z_i) is position of ith neutron.

14

2.8. Statistics

All results of Monte Carlo simulation including effective multiplication factor, reaction rate, and flux are an estimated mean and standard deviation as a result of random sampling. In order to understand the result of Monte Carlo simulation correctly, it is very important to understand how the values are estimated. Two key concepts must be explained first Law of Large Numbers (LLN) and Central Limit Theorem (CLT). Law of large Numbers (LLN) is obvious but important theorem. LLN states that the average of samples will converge to the expected value μ as n gets larger:

$$\lim_{n \to \infty} P\left(\left| \overline{X}_n - \mu \right| < \varepsilon \right) = 1 \quad , \tag{II.21}$$

$$\overline{X}_n = \left(X_1 + X_2 ... + X_n \right) / n \quad , \tag{II.22}$$

where ε is an arbitrary positive number. LLN guarantees that the Monte Carlo result with infinite number of samples will be converges to the true value. CLT states that the distribution of sample average converges to the normal distribution as sample size n approaches to infinity as shown in Eq. (II.23) if samples are independent and identically distributed.

$$\sqrt{n} \left(\left(\frac{1}{n} \sum_{i=1}^{n} X_i \right) - \mu \right) \xrightarrow{d} N\left(0, \sigma^2 \right) \quad . \tag{II.23}$$

Most of the Monte Carlo codes, two terminologies are frequently used: history and cycle (or batch). History means the number of particles simulated per one cycle. The standard deviation is estimated with the sample Q which is the average of samples during each cycle as followings:

$$\sigma^2 \left[\overline{Q} \right] = \frac{1}{N-1} \left(\frac{1}{N} \sum_{i=1}^{N} Q_i^2 - \overline{Q}^2 \right) \quad , \tag{II.24}$$

$$Q_i = \frac{1}{M} \sum_{m=1}^{M} q_m \quad , \tag{II.25}$$

where N is the number of cycles and M is the number of histories.

2.9.   Numerical Tests

MCS is neutron transport code capable of criticality calculation. All general features are implemented in MCS including collision kernel, transport kernel, tally kernel, migration kernel. In this section, the accuracy of MCS is tested comparing other codes and measured data.

2.9.1.   ICSBEP

MCS was tested for critical safety analysis with 23 selected critical benchmarks from the International Criticality Safety Benchmark Evaluation Project (ICSBEP). Selected problems have very simple geometry constructed with one or few spheres. The simulations were performed with ENDF/B-VII.0 library using two codes: MCNP6, and MCS. In this case, the probability-table capability was verified together with the collision kernel. MCS and MCNP6 were simulated two times each with and without probability-table option to verify the probability table function together with collision kernel. Table II-1 and Figure II-7 show the multiplication factor with probability table. The result of MCS is compared with the result of MCNP and measured data. The MCS results match well within 2sigma with MCNP6, and it matches well with measured data too. Figure II-8 shows the effective multiplication factor without probability table and Figure II-9 shows the effect of probability table. As shown in the figures, MCS result matches well with MCNP.
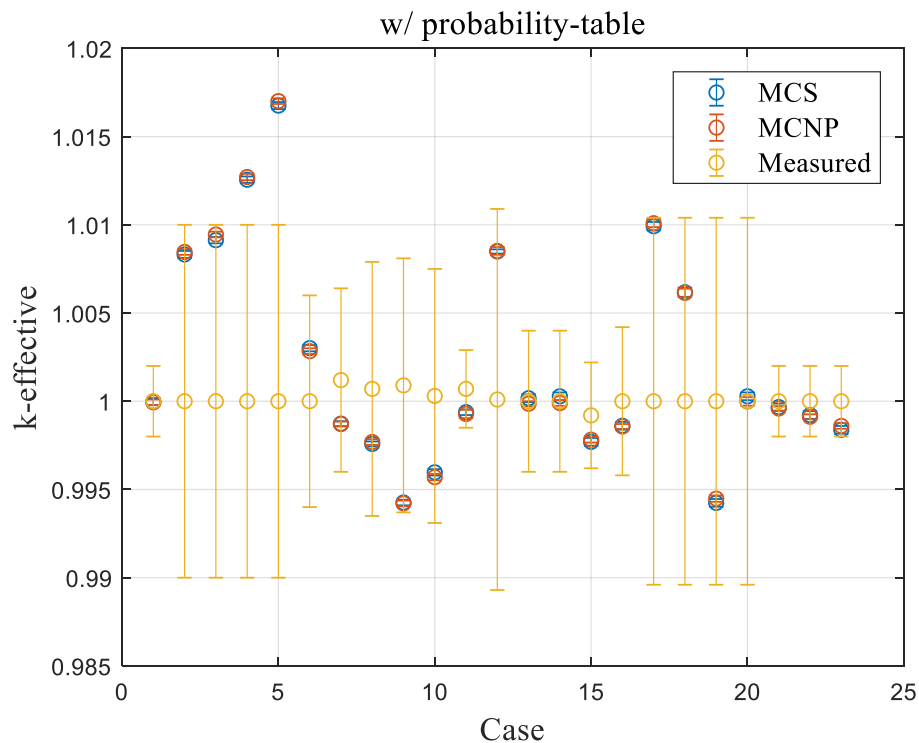
Figure II-7: Effective multiplication facot for ICSBEP benchmark.

Table II-1: Effective Multiplication Factor for ICSBEP Benchmark.

#	Case	Measured	Uncertainty	MCS	SD	MCNP	SD
1	HEU-MET-FAST-001	1.00000	0.00100	0.99998	0.00010	0.99994	0.00008
2	HEU-MET-FAST-003, case2-1	1.00000	0.00500	1.00832	0.00010	1.00846	0.00008
3	HEU-MET-FAST-003, case2-2	1.00000	0.00500	1.00913	0.00009	1.00945	0.00008
4	HEU-MET-FAST-003, case2-3	1.00000	0.00500	1.01256	0.00009	1.01271	0.00009
5	HEU-MET-FAST-003, case2-4	1.00000	0.00500	1.01676	0.00010	1.01701	0.00008
6	HEU-MET-FAST-028	1.00000	0.00300	1.00301	0.00009	1.00284	0.00008
7	HEU-SOL-THERM-013, case 1	1.00120	0.00260	0.99873	0.00007	0.99871	0.00007
8	HEU-SOL-THERM-013, case 2	1.00070	0.00360	0.99758	0.00007	0.99769	0.00008
9	HEU-SOL-THERM-013, case 3	1.00090	0.00360	0.99426	0.00008	0.99421	0.00008
10	HEU-SOL-THERM-013, case 4	1.00030	0.00360	0.99597	0.00009	0.99570	0.00009
11	IEU-MET-FAST-015	1.00070	0.00110	0.99938	0.00008	0.99928	0.00012
12	IEU-SOL-THERM-002	1.00010	0.00540	1.00849	0.00006	1.00852	0.00011
13	PU-MET-FAST-001	1.00000	0.00200	1.00017	0.00011	0.99986	0.00007
14	PU-MET-FAST-002	1.00000	0.00200	1.00028	0.00011	0.99990	0.00008
15	PU-MET-FAST-019	0.99920	0.00150	0.99770	0.00011	0.99782	0.00008
16	PU-MET-FAST-022	1.00000	0.00210	0.99861	0.00011	0.99857	0.00007
17	PU-SOL-THERM-001-case16-1	1.00000	0.00520	1.00992	0.00012	1.01009	0.00011
18	PU-SOL-THERM-001-case16-5	1.00000	0.00520	1.00618	0.00013	1.00614	0.00012
19	PU-SOL-THERM-011-case18-1	1.00000	0.00520	0.99424	0.00011	0.99448	0.00009
20	PU-SOL-THERM-011-case18-6	1.00000	0.00520	1.00028	0.00011	0.99999	0.00012
21	U233-MET-FAST-001	1.00000	0.00100	0.99967	0.00010	0.99959	0.00007
22	U233-MET-FAST-002	1.00000	0.00100	0.99922	0.00011	0.99912	0.00007
23	U233-MET-FAST-003	1.00000	0.00100	0.99838	0.00011	0.99860	0.00008
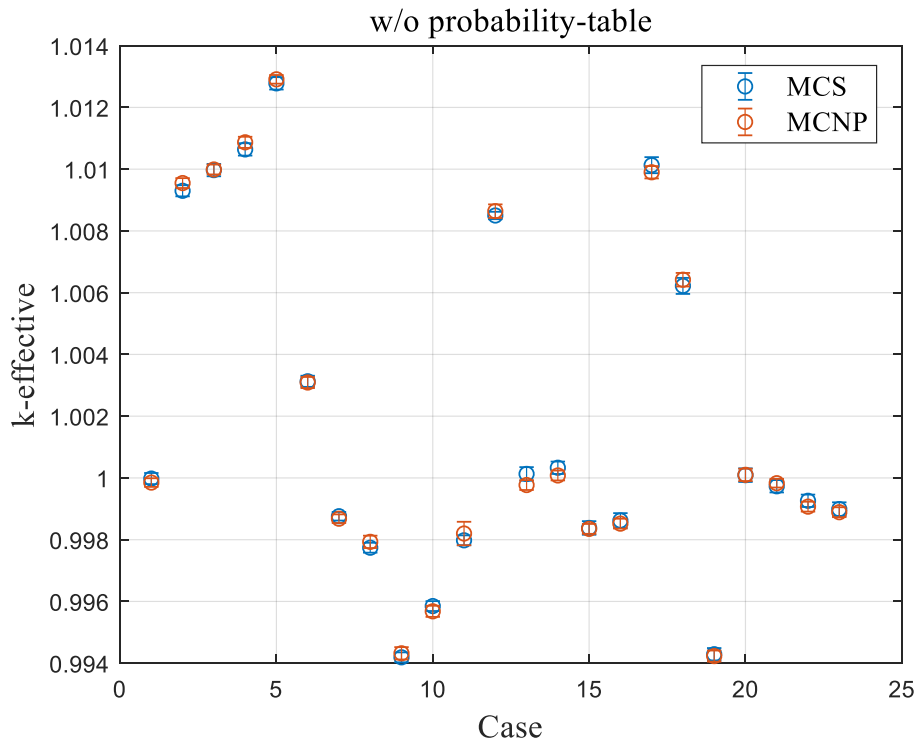
Figure II-8: Effective multiplication factor for ICSBEP benchmark without probabilit-table.
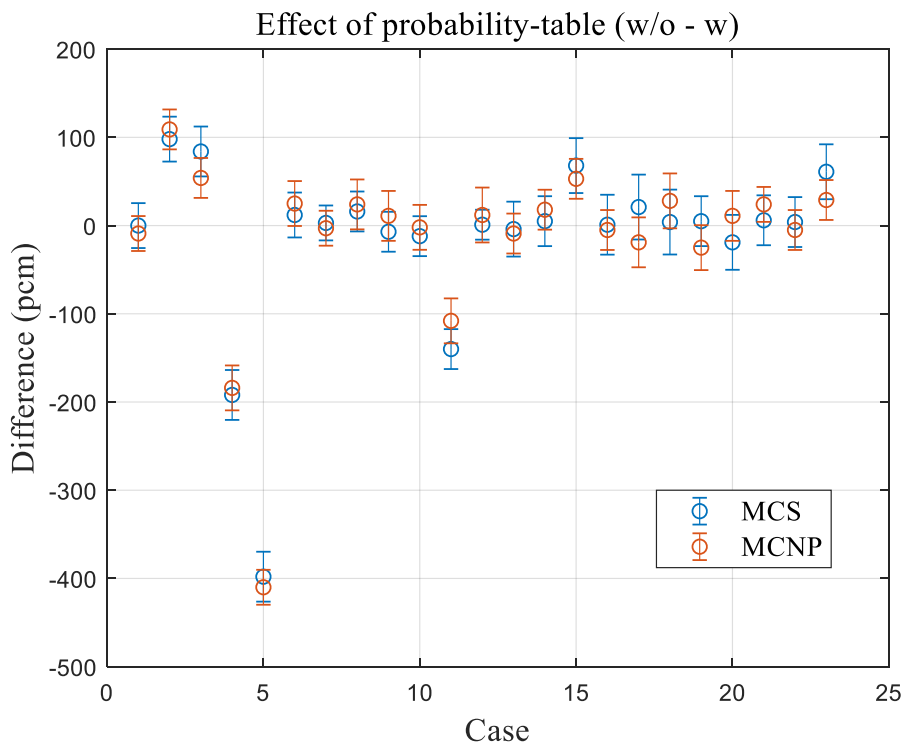
Figure II-9: Effect of probability table option for ICSBEP benchmark.

2.9.2. INDC Benchmark

INDC benchmark is benchmark designed to see how accurately we can calculate thermal systems [27]. The benchmark problem is artificial pin problem composed of fuel and water regions as shown in Figure II-10. Three problems are in the benchmark with fuel radius of 1/2 inch, 1/4 inch, and 1/8 inch. The pin pitch is 5.08cm and coolant density is 1g/cm^3 for all three cases. The fuel density for three cases are presented in Table II-2.
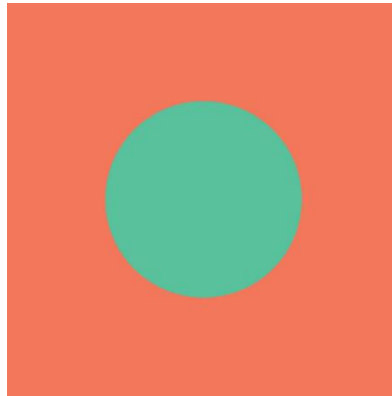
Figure II-10: Configuration of INDC benchmark half inch pin.

Table II-2: Fuel Composition for INDC Benchmark.

Case	ZA	Density (#/barn-cm)
1/2″ pin	92235	4.6614E-04
	92238	4.7099E-02
1/4″ pin	92235	1.6653E-03
	92238	4.5915E-02
1/8″ pin	92235	3.3589E-02
	92238	1.4395E-02

The ENDF-VII.0 library is used for both MCNP6 and MCS simulations. All three cases were solved with and without thermal scattering data to verify the thermal scattering kernel. Table II-3 shows the effective multiplication factor for INDC benchmark. Total six cases are in the table with and without thermal scattering data for three pin geometries. All six cases show good agreement within 2sigma. Half inch problem was selected for further comparison. The flux distribution was tallied with 616 energy groups. The standard deviation of group-wise flux is less than 0.2% for most of the energy range. Figure II-11 shows the energy spectrum of MCS and MCNP for half inch problem. The flux spectrum also matches perfectly.

Table II-3: Effective Multiplication Factor for INDC Benchmark.

Case	MCNP	SD	MCS	SD	Diff. (pcm)
1/2″ no S(α,β)	1.01649	0.00004	1.01658	0.00004	-9
1/2″ S(α,β)	0.96812	0.00004	0.96806	0.00004	6
1/4″ pin no S(α,β)	1.01320	0.00016	1.01359	0.00017	-39
1/4″ pin S(α,β)	0.92197	0.00017	0.92214	0.00019	-17
1/8″ pin no S(α,β)	1.01320	0.00021	1.01327	0.00024	-7
1/8″ pin S(α,β)	0.90950	0.00021	0.90895	0.00023	55
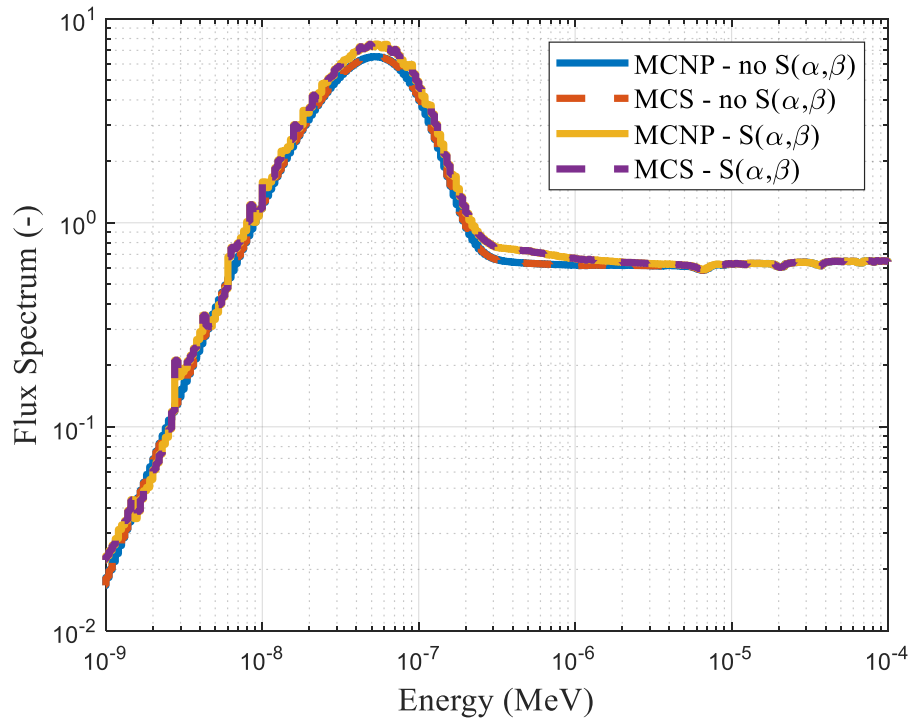
Figure II-11: Flux spectrum for INDC half inch problem.

2.9.3. The Doppler-Defect Benchmark

The Doppler-defect benchmark [28] is the problem designed to verify the capability to estimate the Doppler coefficient. This benchmark is selected to verify the Doppler Broadening Rejection Correction (DBRC) function together with free gas scattering kernel. There are three subsets of benchmark with same pin geometry as shown in Figure II-12: UO_2 fuel ranging from natural enrichment to 5.0 wt.%, reactor-recycle MOX fuel ranging 1 wt.% to 8 wt.% PuO_2, weapons-grade MOX ranging 1 wt.% to 6 wt.% PuO_2.
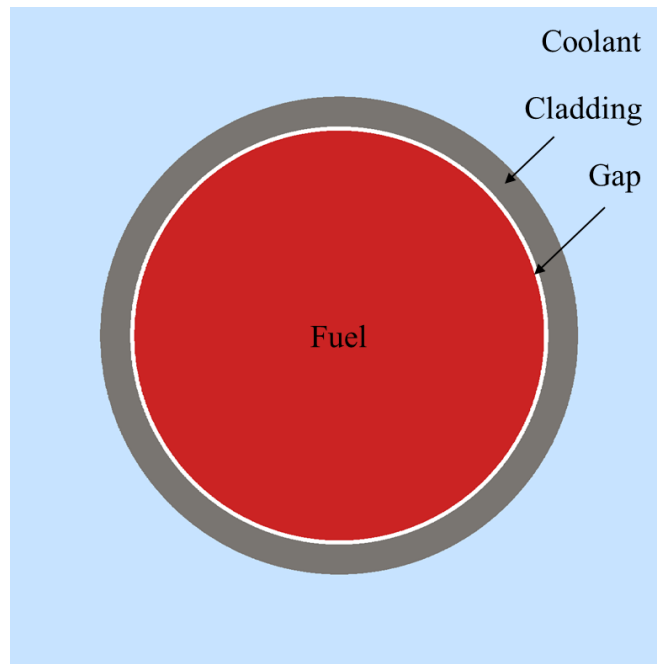
Figure II-12: Configuration of Doppler-defect benchmark.

This benchmark contains the pairs of Hot Zero Power (HZP) and Hot Full Power (HFP) specifications. In HZP state, the temperatures for fuel, gap, cladding, and coolant are 600K identically. In HFP state, the fuel temperature is 900K, and the remaining regions are 600K as HZP. The simulations were performed two times for each case with and without DBRC option by using ENDF-VII.0 library. The Doppler coefficient was calculated as follow:

$$DC = \frac{\Delta \rho_{Dop}}{\Delta T_{Fuel}} ,$$

(II.26)

$$\Delta \rho_{Dop} = \frac{1}{k_{HZP}} - \frac{1}{k_{HFP}} .$$

(II.27)

Figure II-13 shows the Doppler coefficient estimated by MCS and Serpent with 1sigma for UO$_2$ fuel problem. MCS and serpent matches very well within standard deviation for all cases. Figure II-14 and Figure II-15 show the Doppler coefficient for reactor-recycle MOX fuel and weapons-grade MOX fuel. MCS shows good agreement also for those cases. Table II-4 show the multiplication factor for all three cases with and without DBRC. As shown in the table, the effective multiplication factors are also match well within standard deviation for all cases verifying the accuracy of MCS.
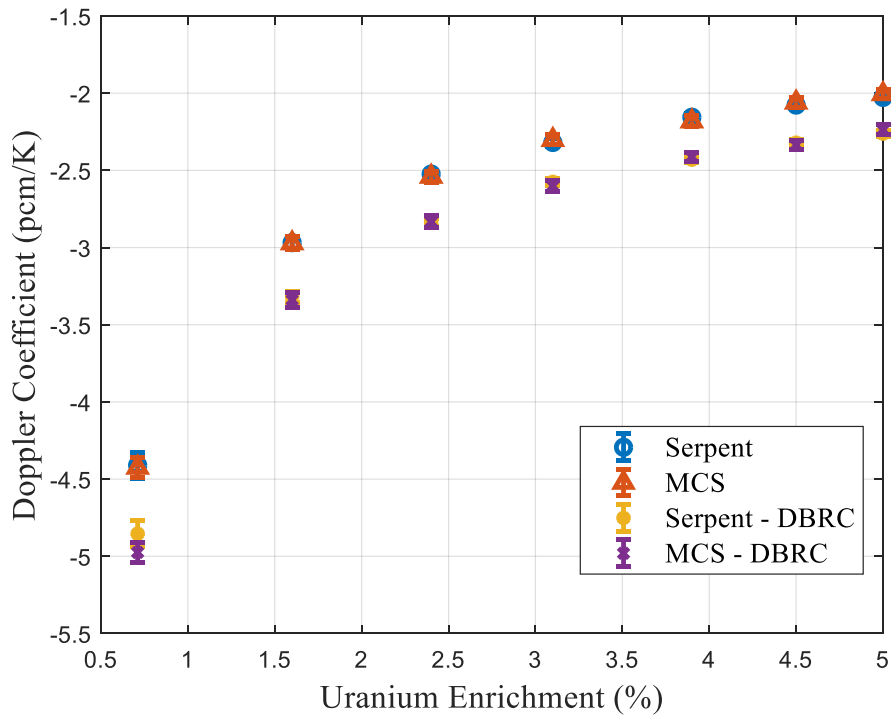
Figure II-13: Doppler coefficient for Doppler-defect benchmark UO$_2$ fuel.
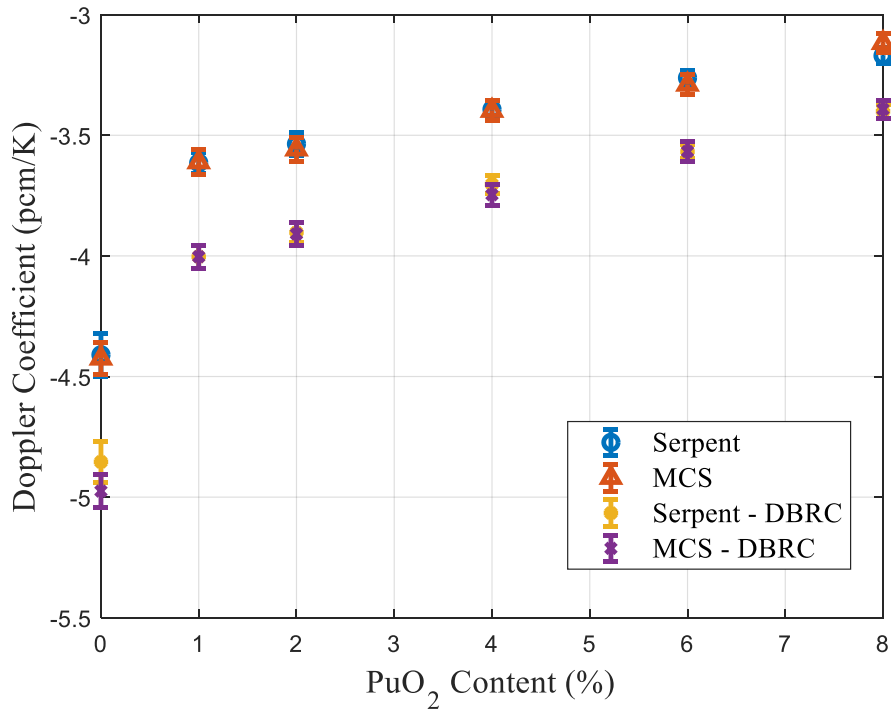
Figure II-14: Doppler coefficient for Doppler-defect benchmark reactor-recycle MOX fuel.
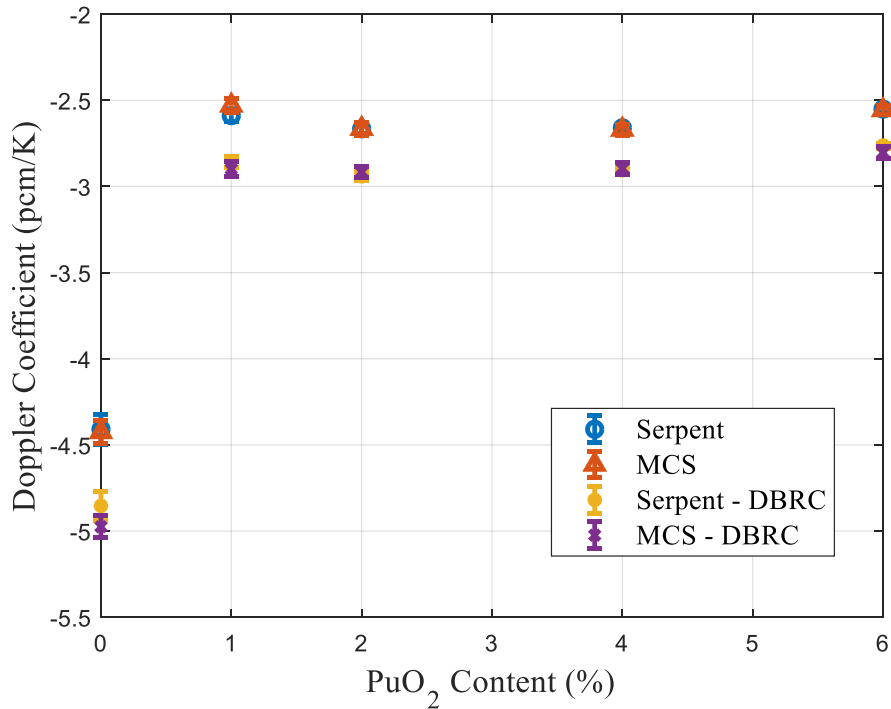
Figure II-15: Doppler coefficient for Doppler-defect benchmark weapons-grade MOX fuel.

Table II-4: Effective Multiplication Factor for Doppler-Defect Benchmark.

Case (enrichment wt.%)		HZP				HFP				HZP - DBRC				HFP - DBRC			
		Serpent	SD	MCS	SD	Serpent	SD	MCS	SD	Serpent	SD	MCS	SD	Serpent	SD	MCS	SD
UO$_2$	0.711	0.66561	0.00004	0.66562	0.00003	0.65980	0.00004	0.65979	0.00003	0.66513	0.00004	0.66525	0.00003	0.65875	0.00004	0.65871	0.00003
	1.6	0.96077	0.00003	0.96082	0.00004	0.95262	0.00004	0.95266	0.00004	0.96019	0.00003	0.96031	0.00004	0.95110	0.00004	0.95116	0.00005
	2.4	1.09901	0.00003	1.09906	0.00005	1.08994	0.00003	1.08993	0.00004	1.09831	0.00004	1.09842	0.00005	1.08813	0.00003	1.08826	0.00005
	3.1	1.17695	0.00004	1.17694	0.00004	1.16739	3.00000	1.16745	0.00005	1.17620	0.00003	1.17632	0.00005	1.16561	0.00003	1.16562	0.00006
	3.9	1.23967	0.00004	1.23972	0.00005	1.22981	0.00003	1.22974	0.00006	1.23891	0.00003	1.23895	0.00005	1.22782	0.00003	1.22794	0.00005
	4.5	1.27503	0.00003	1.27507	0.00005	1.26498	0.00003	1.26510	0.00005	1.27433	0.00003	1.27439	0.00005	1.26312	0.00003	1.26311	0.00005
	5	1.29947	0.00003	1.29943	0.00006	1.28928	0.00003	1.28935	0.00005	1.29859	0.00003	1.29865	0.00006	1.28725	0.00003	1.28743	0.00006
Recycle-MOX	0	0.66561	0.00004	0.66562	0.00003	0.65980	0.00004	0.65979	0.00003	0.66513	0.00004	0.66525	0.00003	0.65875	0.00004	0.65871	0.00003
	1	0.94479	0.00004	0.94467	0.00005	0.93521	0.00004	0.93510	0.00005	0.94390	0.00004	0.94390	0.00004	0.93332	0.00005	0.93332	0.00005
	2	1.02058	0.00005	1.02064	0.00005	1.00965	0.00005	1.00964	0.00006	1.01968	0.00004	1.01967	0.00005	1.00765	0.00005	1.00762	0.00005
	4	1.07575	0.00004	1.07581	0.00005	1.06410	0.00005	1.06414	0.00005	1.07475	0.00004	1.07485	0.00005	1.06207	0.00005	1.06202	0.00005
	6	1.10448	0.00004	1.10455	0.00006	1.09267	0.00004	1.09264	0.00005	1.10348	0.00004	1.10353	0.00005	1.09060	0.00004	1.09065	0.00006
	8	1.12793	0.00004	1.12784	0.00005	1.11596	0.00005	1.11607	0.00005	1.12696	0.00004	1.12705	0.00005	1.11415	0.00004	1.11427	0.00005
Weapon-MOX	0	0.66561	0.00004	0.66562	0.00003	0.65980	0.00004	0.65979	0.00003	0.66513	0.00004	0.66525	0.00003	0.65875	0.00004	0.65871	0.00003
	1	1.09052	0.00004	1.09039	0.00005	1.08136	0.00004	1.08144	0.00005	1.08971	0.00004	1.08974	0.00006	1.07963	0.00004	1.07951	0.00005
	2	1.18106	0.00004	1.18112	0.00006	1.17001	0.00003	1.17007	0.00005	1.18014	0.00004	1.18016	0.00005	1.16798	0.00004	1.16810	0.00005
	4	1.24974	0.00003	1.24984	0.00005	1.23740	0.00004	1.23745	0.00005	1.24880	0.00003	1.24883	0.00006	1.23535	0.00003	1.23543	0.00006
	6	1.28641	0.00003	1.28644	0.00005	1.27387	0.00003	1.27387	0.00005	1.28546	0.00002	1.28549	0.00006	1.27191	0.00003	1.27174	0.00006

2.9.4. BEAVRS Cycle 1 HZP

The Benchmark for Evaluation And Validation of Reactor Simulations (BEAVRS) [29] is a benchmark published at MIT computational Reactor Physics Group in 2013. The benchmark provides measured data of critical boron concentration, detector signals, temperature coefficient together with detailed specifications of reactor core. BEAVRS is Westinghouse type pressurized water reactor contains 193 fuel assemblies composed of 17×17 pins. Figure II-16 shows the radial and axial configuration of BEAVRS core with D bank control rod inserted.
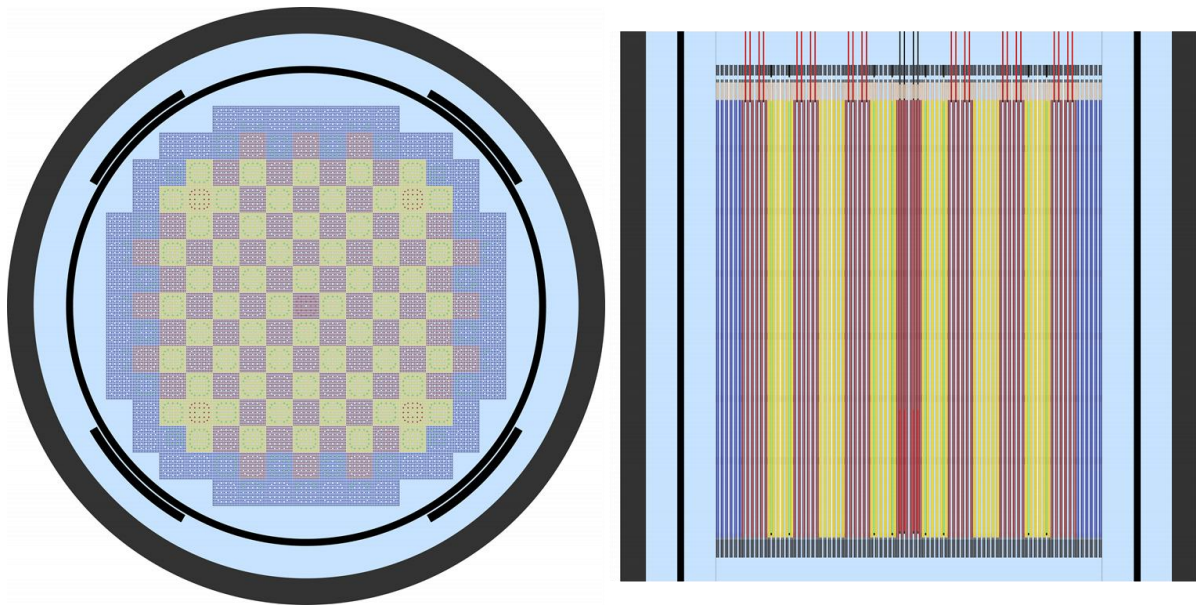
Figure II-16: Configuration of BEAVR core generated by MCS.

The Hot Zero Power (HZP) condition of 566K was analyzed by employing ENDF/B-VII.1 nuclear data. The multiplication factor was calculated with 300 subcycles, 2 inactive cycles, 20 active cycles, and 10,000 histories per subcycle. Initial source neutrons were equally distributed inside of core. Table II-5 presents the multiplication factor with variation of boron concentration and rod positions. Table II-6 shows the control rod worth calculated by following equation:

$$\rho = \frac{1}{k_{out}} - \frac{1}{k_{in}} \ .$$

(II.28)

The rod worth for various rod are compared with measured data, SurperMC [30], nTRACER , MC21, and OpenMC [31]. The MCS result matches well for all cases within 10-50 pcm different.

25

Table II-5: Multiplication Factors with Variation of Boron and Rod Position for BEAVRS Cycle 1 HZP.

Rod	Inserted Rod	Boron Concentration (pcm)	Out		In	
			k-effective	SD	*k-effective*	SD
D	NONE	938.5	1.00340	0.00009	0.99578	0.00009
C	D	856	1.00752	0.00009	0.99555	0.00009
B	D, C	748	1.00963	0.00009	0.99717	0.00009
A	D, C, B	748	0.99566	0.00009	0.99004	0.00009
SE	D, C, B, A	597	1.00938	0.00009	1.00404	0.00009
SD	D, C, B, A, SE	597	1.00404	0.00009	0.99602	0.00009
SC	D, C, B, A, SE, SD	597	0.99602	0.00009	0.98505	0.00009

Table II-6: Control Rod Bank Worth for BEAVRS Cycle 1 HZP.

Rod	measured	MCS	SuperMC	MC21	nTRACER	OpenMC
D	788	763	779	773	776	771
C	1203	1193	1266	1260	1210	1234
B	1171	1237	1180	1172	1230	1197
A	548	570	567	574	535	556
SE	461	527	532	544	455	501
SD	772	802	791	786	-	844
SC	1099	1118	1114	1122	-	1049

The three-group flux with the boundary energy of $1eV$ and $200KeV$ and one group fission source distribution at all rod out condition was calculated with mesh tally function. The mesh size is same as pin size with axial 10 equally divided meshes. Figure II-17 shows the three-group flux and fission reaction rate distribution.

The isothermal temperature coefficient was calculated with two temperature points at 566.6K and 580K. MCS run had 200 inactive, 2000 active and 2,500,000 histories for each calculation. The ITC results are summarized in Table II-7. The difference between measured data and calculated data was 0-17%.
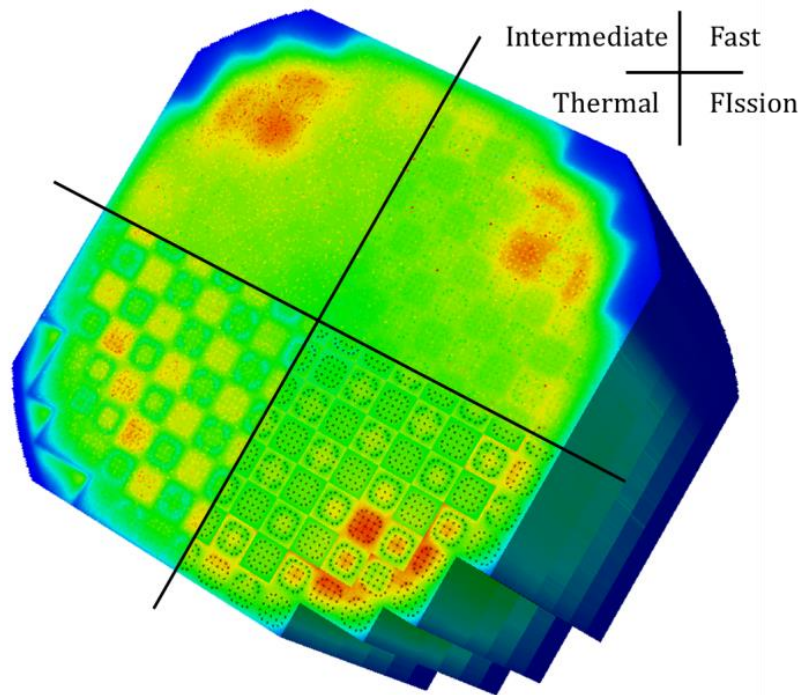
Figure II-17: Three group flux and fission distribution for BEAVRS Cycle 1 HZP.

Table II-7: Isothermal Temperature Coefficient for BEAVRS Cycle 1 HZP.

Rod	Measured	MCS	Diff. (%)	nTRACER	Diff. (%)
ARO	-1.75	-1.46	16.75%	-1.83	-4.57%
D in	-2.75	-2.78	-1.13%	-3.29	-19.64%
C in	-8.01	-7.99	0.21%	-7.99	0.25%

The detector signal is calculated by inserting very small amount of ^{235}U gas into instrument tube and tallying fission reaction rate. The calculated detector signal has standard deviation around 1% in all positions. The RMS error of tallied result and measured data are 5% and the distribution is presented in Figure II-18.

	R	P	N	M	L	K	J	H	G	F	E	D	C	B	A
1	Tallied Measured C/E-1 (%)						0.739 / 0.777 / -4.946			0.719 / 0.699 / 2.826					
2			0.640 / 0.645 / -0.814			1.197 / 1.171 / 2.248		1.234 / 1.223 / 0.883							
3								0.925 / 0.898 / 2.974		0.961 / 0.965 / -0.413		1.167 / 1.171 / -0.354		0.668 / 0.689 / -3.112	
4		0.865 / 0.875 / -1.190	1.103 / 1.115 / -1.109					1.192 / 1.115 / 6.878							
5					1.309 / 1.165 / 12.398				1.174 / 1.129 / 3.953		1.284 / 1.247 / 2.971		1.365 / 1.321 / 3.328		
6	0.719 / 0.670 / 7.266		0.959 / 0.920 / 4.255			1.201 / 1.101 / 9.086		1.095 / 1.042 / 5.112						1.264 / 1.239 / 1.987	
7				0.969 / 0.924 / 4.822			1.053 / 1.008 / 4.446			0.937 / 0.892 / 5.064			1.276 / 1.204 / 5.952		
8	0.727 / 0.730 / -0.469		0.915 / 0.899 / 1.824		0.936 / 0.918 / 1.990		0.822 / 0.774 / 6.240			1.125 / 1.088 / 3.433		1.203 / 1.175 / 2.414	0.947 / 0.966 / -1.977	1.261 / 1.295 / -2.614	
9		0.882 / 0.837 / 5.423							1.045 / 1.017 / 2.749		1.193 / 1.175 / 1.556				0.838 / 0.845 / -0.823
10					0.980 / 0.964 / 1.658		0.932 / 0.920 / 1.338					1.249 / 1.290 / -3.191			
11	0.549 / 0.576 / -4.747				1.216 / 1.263 / -3.752			0.942 / 0.969 / -2.780			1.318 / 1.330 / -0.883				0.605 / 0.631 / -4.089
12					1.220 / 1.223 / -0.241				0.955 / 1.034 / -7.683			1.334 / 1.438 / -7.236			
13		0.829 / 0.857 / -3.325			1.345 / 1.339 / 0.411			0.919 / 0.984 / -6.572						0.689 / 0.792 / -12.957	
14			0.679 / 0.700 / -2.969				0.820 / 0.919 / -10.727			1.270 / 1.357 / -6.403		0.938 / 1.050 / -10.670			
15					0.558 / 0.602 / -7.251			0.723 / 0.837 / -13.669							

Figure II-18: Detector Signal Comparison for BEAVRS Cycle 1 HZP.

2.10. Parallel Algorithm

Monte Carlo simulation is always suffering from computing time. Therefore, parallel simulation capability is one of the most important features of Monte Carlo codes. Most of the Monte Carlo codes employ master-slave algorithm. In the framework of master-slave algorithm, all processors are the slaves but one mater processor. Master processor does not solve the problem but manage the workload of slaves. Master sends the work to slaves and slaves send back the simulation result to master. The master-slave algorithm can be efficient in the view point of load balancing, but it may suffer from the communication overhead when large number of processors is used. To overcome the communication overhead, parallel fission bank algorithm was proposed [32]. In the framework of parallel fission bank, all processors are slaves, and they communicate with neighbor processors directly not through master. Therefore, the communication overhead does not increase as number of processors increases.

The parallel efficiency of MCS large-scale power reactor simulation is tested against BEAVSR benchmark quarter core geometry at End of Cycle (EOC) which has 251 nuclides in each fuel cells. All feedbacks require for power reactor simulation described in section IV including depletion, equilibrium xenon, thermal hydraulics are employed with 5 axial meshes per fuel pin. The computing time was measured with various number of processors up to 1,120 processors. Each processor was assigned to solve 10,000 particles every cycle. Thus, the total number of histories per cycle is 10,000 times number of processors in this test simulation. The parallel efficiency is calculated based on the computing time 28 processors. As shown in the Figure II-19, the efficiency is maintained above 90% up 1,120 processors.
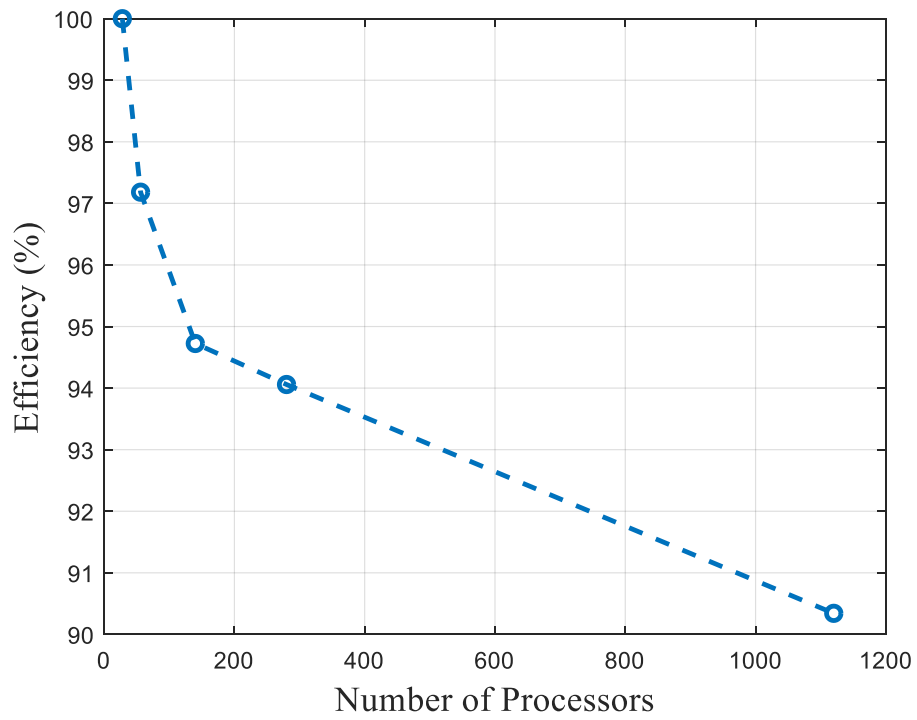
Figure II-19: Parallel efficiency for BEAVRS benchmark at EOC.

2.11. Hash-Indexing

The tally bin searching time can grow as *O(n)* with number of tally cells if sequential search algorithm is used as implemented in MCNP. The searching time is reasonably small if the number of cells is small. However, MC codes would spend most of simulation time searching tally bin index if number of tally bins are large as in core calculation. To overcome this issue, MC codes adopts hash-indexing algorithm. RMC shows the 8.45% overhead with 6M tally bins [33]. OpenMC shows 13% overhead with 8M tally bins [34][35]. The hash-indexing for tally bin searching is implemented into MCS.

Two types of cells exist in MCS. Normal cell filled with a material and universe cell filled with universe or lattice. The number of normal cells in universe *u* can be counted as follows

$$N(u) = NC + \sum_{i=1}^{UC} N(uid_u(i)) \quad , \tag{II.29}$$

where *NC* is number of normal cells, *UC* is number of universe cells in the universe, *uid* is the function returns the global universe index. For the lattice universe, the accumulated number of normal cells should be prepared. The accumulated normal cell for k^{th} universe in lattice *j*, $AC_j(k)$, is the number of normal cells in the universe from 1 to k-1th universe in the lattice. For example, there are two universes, U_1 and U_2 as shown in Figure II-20. There are three normal cells in U_1 and two cells in U_2. Those universes are used to constructed the lattice geometry as presented in Figure II-21. There are four universes in the lattice. The first universe is U_2, and the accumulated normal cell, *AC*, is 0 since it is first component. The second universe is U_1, and the *AC* is 2 since there are two normal cells in first universe. The third universe is U_1, and the *AC* is 5 (2 + 3). The last universe is U_2, and *AC* is 8 (2 + 3 + 3). The index of unique cell can be calculated by using *N(u)* and *AC*. Let's say the particle is positioned at the red dot in the figure. The particle is in third element of lattice. Therefore, the index is 8 (=*AC* + cell index in universe).
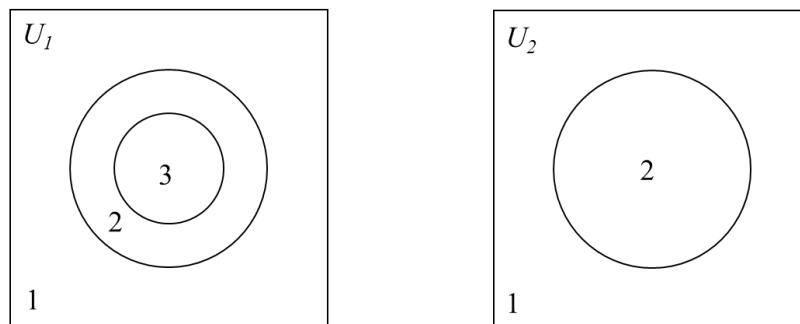
Figure II-20: Cell index in universe.

Particle Position
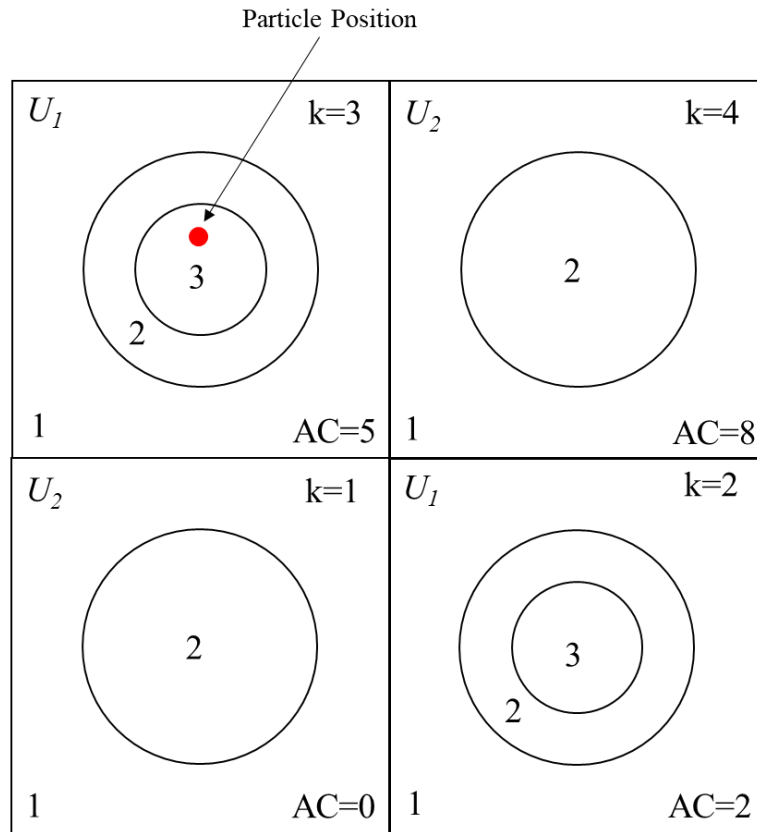
Figure II-21: Cell index in lattice.

Fortunately, all information required to calculate the cell index including universe id and cell id is already used in the Monte Carlo simulation for particle transport. Therefore, the index can be calculated by using pre-generated AC and $N(u)$ easily. The index calculation time is $O(L)$ where L is number of levels used to construct geometry. Most of the cases, the geometry is constructed within 5 levels. Thus, the computing portion to calculate index is reasonably small. As explained in above, the base index can be calculated very efficiently. In addition to the capability to calculate base index, MCS pre-generates the 1D array contains the tally bin index information. MCS can read the tally bin index corresponding base index.

The tally performances of MCS is tested against the Monte Carlo performance benchmark [36], a core containing 63,624 fuel cells. Figure II-22. shows the core configuration and base index image for Performance Benchmark core geometry. The different color represents the different index. Thus, it can be easily confirmed the cell mesh from the color. Prior to the tally performance evaluation, the tracking performance is evaluated and compared against MCNP6.1 [37]. The simulation was performed on Linux cluster with single processor (Intel Xeon X5690 @ 3.47 GHz). MCNP and MCS run had 100 inactive cycles, 400 active actives and 10,000 neutron histories per cycle by employing identical ACE

format files for the fair comparison. The effective neutron multiplication factor and number of particle histories treated per second are shown in Table II-8. For this configuration, MCS and MCNP6.1 produce the same multiplication factor, MCS being about 55% faster than MCNP6.1.
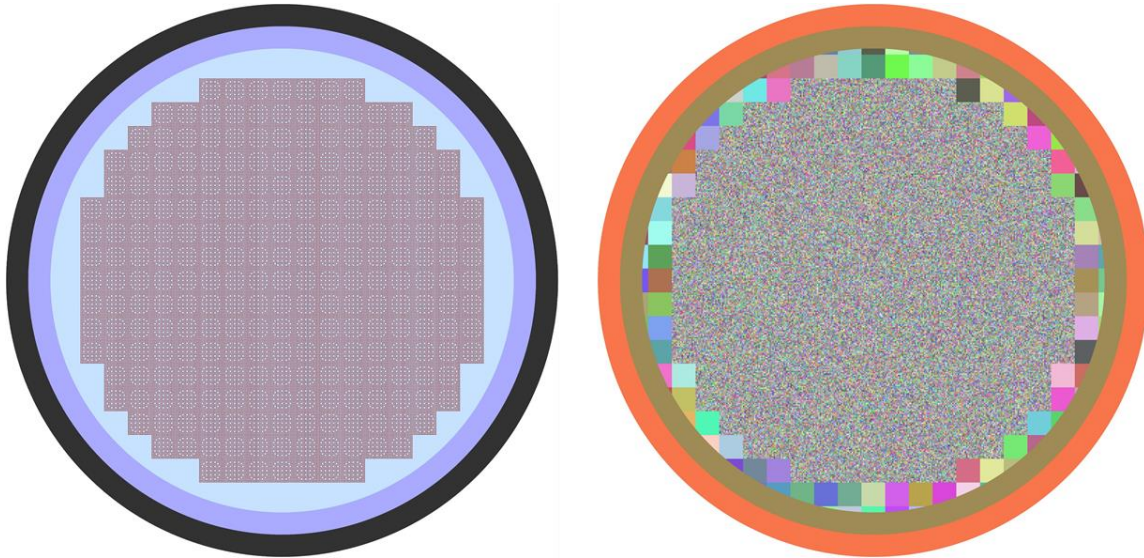
Figure II-22: Configuration of Monte Carlo performance benchmark core (left) and base index (right).

Table II-8: Multiplication Factor and Particle Per Second for Monte Carlo Performance Benchmark.

Code	*k-effective*	SD	Particle Per Second
MCS	0.99983	0.00033	2,799
MCNP6.1	0.99961	0.00032	1,572

Further test is performed to check the efficiency of MCS handle massive tallies. In this test, the particle per second is measured under various number of axial nodes per fuel pin and the number of tallies per fuel cell. The number of tally bins is number of fuel pins (63,624) times the number of axial nodes (varying from 2 to 200 nodes). In each case, the simulations were repeated with different number of tally quantities from 0 to 20. All simulations were performed on Linux cluster with 36 processors. Figure II-23 shows the number of particles treated per second in a single processor. As shown in the figure, the tally overhead of MCS is independent of number of tally bins due to hash searching algorithm. The overhead is 1.5% when tallying one quantity, and it is 10% when tally 20 tally quantities. The overhead is from tally bin searching time and tally scoring. The tally scoring overhead can be estimated by dividing 10% to 20 which is 0.5% per one quantity, and the tally bin searching overhead is therefore 1%.
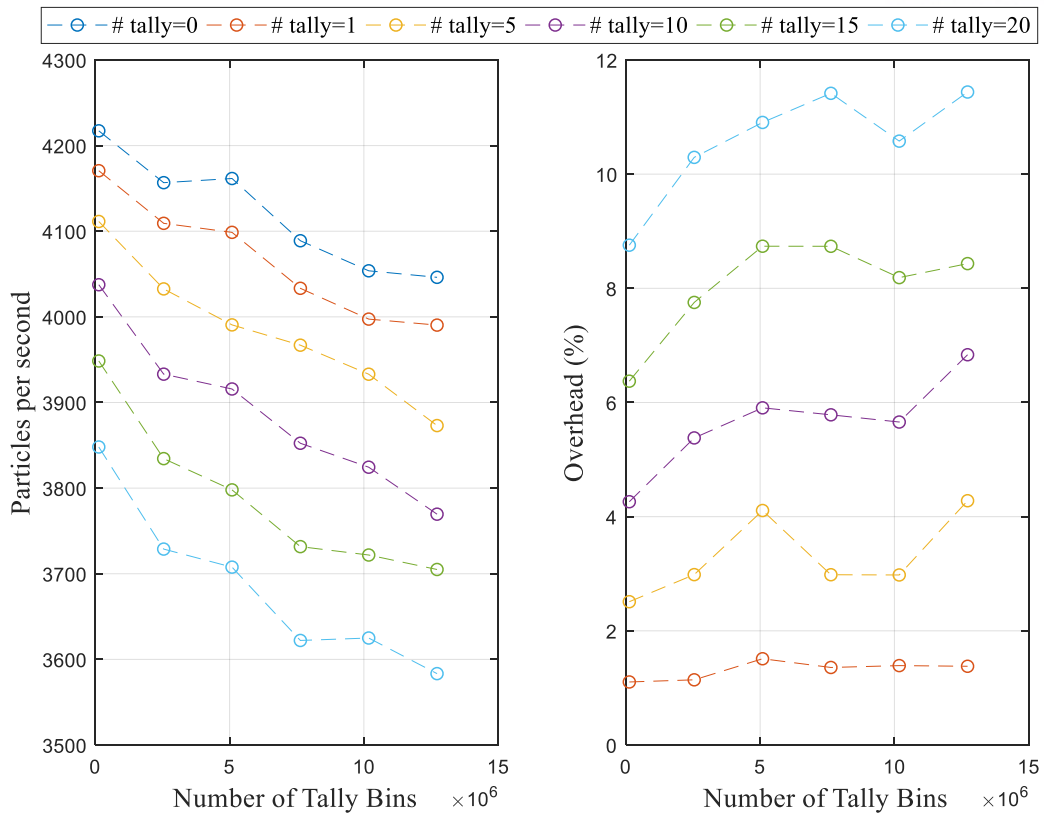
Figure II-23: Particle per second and overhead for Monte Carlo performance benchmark.

III. Inter-Cycle Correlation

3.1. Introduction

The Monte Carlo codes estimates the result based on the Low of Large Numbers (LLN) and Central Limit Theorem (CLT) as described in section 2.8. The key assumption of CLT is that the samples are independent. However, the samples of Monte Carlo simulations are dependent since the fission sources for cycle *i* are sampled during cycle *i-1* simulation. In case of low dominance problem, the inter-cycle correlation is weak enough to assume independent correlation. However, the assumption is not valid for high dominance problem. In case of high dominance problem, the inter-cycle correlation is too strong enough to break the Independent Identically Distributed (IID) assumption for CLT. Due to the positive inter-cycle correlation,

- Monte Carlo code underestimates the standard deviation.
- The convergence trend of standard deviation does not follow $1/\sqrt{N}$.

There have been many researches to understand the effect of inter-cycle correlation on standard deviation, and to estimate the real standard deviation. Gelbard and Prael developed a mathematical model of deviation in terms of stochastic errors propagate cycle by cycle [38]. This model has been used for predicting effect of inter-cycle correlation on multiplication factor. Brissenden and Garlick proposed superhistory powering method [39]. The superhistory method runs multiple number of generations without renormalization of fission source distribution which reduces the variance bias. Gelbard and Prael proposed the batch method [40] which uses average value over several cycles to estimate the variance. Ueki [41] devised the *k*-tally lag covariance method to estimate the bias of the sample variance. Shim [42] proposed the method to estimate the variance bias using covariance of fission source distribution computed cycle-by-cycle error propagation model. Miao [43] developed equation to predict the convergence behavior of correlated standard deviation in terms of autocorrelation coefficient. To summarize the researches above

- Variance bias can be estimated if lag *k* covariance (or autocorrelation coefficient) is known.
- The variance bias can be reduced by adopting superhistory method or batch method.

On the other hands, the studies to improve tally efficiency of MC tally by incorporating deterministic solver such as Coarse Mesh Finite Different (CMFD) [44][45][46] method, Fission Matrix Method (FMM), Low-Ordered Operator (LOO) [47]. The conclusion of those researches is

- Efficiency of tally can be improved by a factor of 2-3 in terms of figure of merit by choosing proper number of cycle and histories per cycle.

- Tremendous number of histories must be used to prevent divergence or bias of deterministic solver.

3.2. Inter-Cycle Correlation of Tally

3.2.1. *Underestimation of Variance in Tally*

The sample mean, $\overline{Q}$, of MC tallied quantity during N active cycles is calculated by

$$\overline{Q} = \frac{1}{N}\sum_{i=1}^{N} Q^i \;,$$

(III.1)

where Q^i is the tally quantity at cycle i. The sample variance of $\overline{Q}$ is calculated by

$$\sigma_S^2\left[\overline{Q}\right] = \frac{1}{N(N-1)}\sum_i^N \left(Q^i - \overline{Q}\right)^2 \;,$$

(III.2)

The expected sample variance known as apparent variance is defined by

$$\sigma_A^2\left[\overline{Q}\right] = E\left[\sigma_S^2\left[\overline{Q}\right]\right] = \frac{1}{N}\left(E\left[\left(Q^i\right)^2\right] - E\left[\overline{Q}^2\right]\right)$$

$$= \frac{1}{N}\sigma^2\left[Q^i\right] - \frac{1}{N-1}\frac{1}{N^2}\sum_i\sum_{j\neq i}\mathrm{cov}\left[Q^i, Q^j\right] \;.$$

(III.3)

The covariance of cycle i and j depends on the cycle difference, k, during stationary cycle. Eq. (III.3) can be simplified as below

$$\sigma_A^2\left[\overline{Q}\right] = \frac{1}{N}\sigma^2\left[Q^i\right] - \frac{2}{N-1}\frac{1}{N^2}\sum_{k=1}^{N-1}(N-k)\mathrm{cov}_k\left[Q^i\right] \;.$$

(III.4)

The real variance of $\overline{Q}$ is defined by

$$\sigma^2\left[\overline{Q}\right] = \frac{1}{N}\sigma^2\left[Q^i\right] + \frac{2}{N^2}\sum_{k=1}^{N-1}(N-k)\mathrm{cov}_k\left[Q^i\right] \;.$$

(III.5)

The variance bias is the difference of real and apparent variance which is obtained by subtracting Eq. (III.5) from (III.4) as follows:

$$\sigma^2\left[\overline{Q}\right] - \sigma_A^2\left[\overline{Q}\right] = \frac{2}{N-1}\frac{1}{N}\sum_{k=1}^{N-1}(N-k)\mathrm{cov}_k\left[Q^i\right] \;.$$

(III.6)

The real to apparent ratio can be approximately determined by assuming apparent variance to sample variance as follows:

$$\frac{\sigma^2\left[\overline{Q}\right]}{\sigma_A^2\left[\overline{Q}\right]} = 1 + \frac{2}{N-1}\frac{1}{N}\sum_{k=1}^{N-1}(N-k)\frac{\mathrm{cov}_k\left[Q^i\right]}{\sigma_A^2\left[\overline{Q}\right]}$$
$$\cong 1 + \frac{2}{N-1}\frac{1}{N}\sum_{k=1}^{N-1}(N-k)\frac{\mathrm{cov}_k\left[Q^i\right]}{\sigma_S^2\left[\overline{Q}\right]} \qquad (\text{III.7})$$

The tally quantity at cycle i is the average of M histories, and it should be noted that there is no correlation between particles in the same cycle. Thus, the covariance of Q^i is proportional to the $1/M$ as follows:

$$M_1\,\mathrm{cov}_k\left[Q_{M_1}^i\right] = M_2\,\mathrm{cov}_k\left[Q_{M_2}^i\right] = C_k \qquad (\text{III.8})$$

The real to apparent ratio also can be expressed in terms of autocorrelation coefficient, ρ_k, for large N as follows:

$$\frac{\sigma^2\left[\overline{Q}\right]}{\sigma_A^2\left[\overline{Q}\right]} \cong 1 + \frac{2}{N-1}\frac{1}{N}\sum_{k=1}^{N-1}(N-k)\frac{\mathrm{cov}_k\left[Q^i\right]}{\sigma_S^2\left[\overline{Q}\right]}\frac{N\,\sigma_S^2\left[\overline{Q}\right]}{\sigma^2\left[Q^i\right]}$$
$$= 1 + \frac{2}{N-1}\sum_{k=1}^{N-1}(N-k)\rho_k \qquad (\text{III.9})$$

3.2.2. Numerical Test

Numerical test is performed using a one-dimensional homogenous slab geometry employing one group cross sections as shown in Table III-1. The thickness of slab is 10 cm, and the reflective boundaries are imposed on both sides. The analytic solution of fundamental mode is easily calculated as flat flux and k-infinity of 1.2. The nu-fission reaction at left half region was tallied and studied in this section.

Table III-1: One Group Cross Sections for Simple Slab Problem.

Total (1/cm)	Scattering (1/cm)	Nu-fission	Absorption
1.0	0.6	0.48	0.4

The inter-cycle covariance was estimated by employing 100 inactive cycles, 100,000 active cycles, and 100,000 histories per cycle. Figure III-1 shows the estimated covariance by using sampled quantity from cycle 1 to N. As shown in the figure, it requires tremendous number of samples more than 10^4 cycles. Because of this poor convergence of covariance, it is almost impossible to tally in practical simulation. Figure III-2 and Figure III-3 show the covariance and autocorrelation coefficients estimated using 10^5 samples.
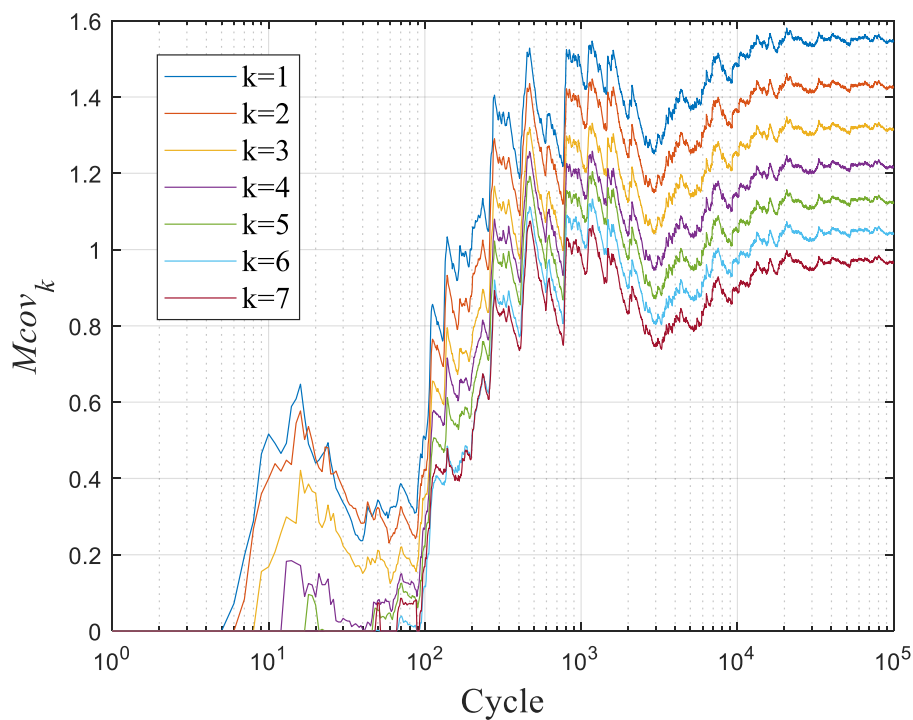
Figure III-1: Covariance convergence of nu-fission in half region for 1D1G problem.
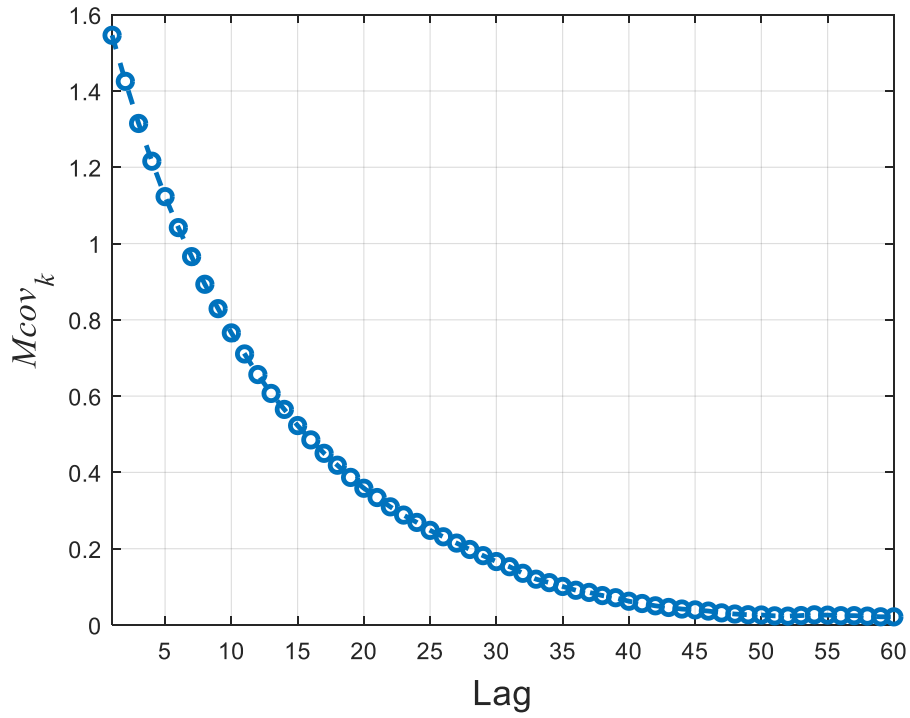
Figure III-2: Covariance of nu-fission in half region for 1D1G problem.
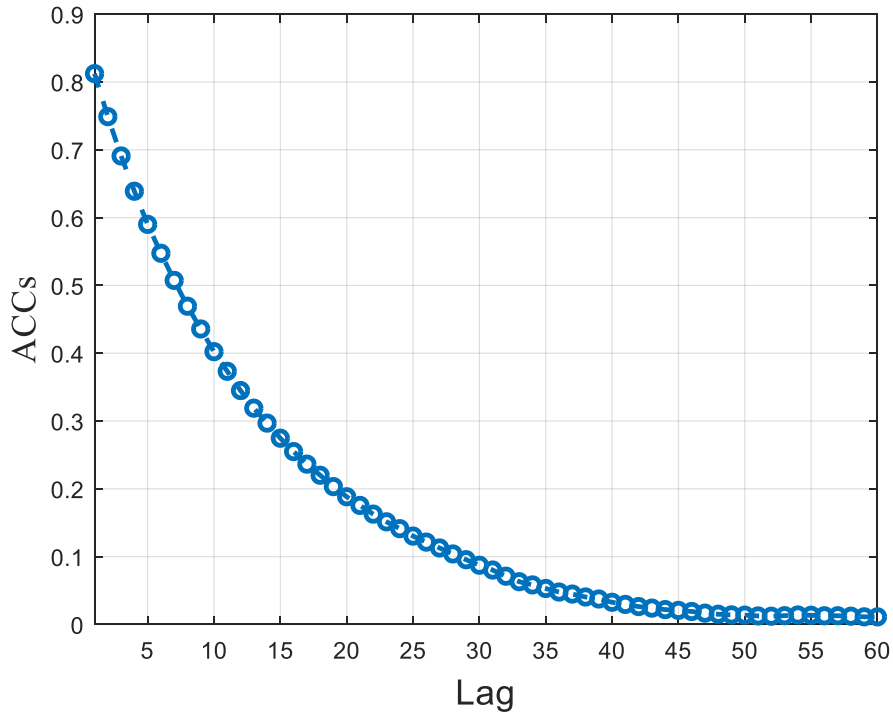
Figure III-3: ACCs of nu-fission in half region for 1D1G problem.

Eqs. (III.7) and (III.9) are tested comparing real variance measured from 100 independent simulations. Each simulation employed 200 inactive cycles, 1,000 active cycles, and 90,000 histories per cycle. Figure III-4 shows the convergence trend of apparent standard deviation and three real standard deviation: measured with 100 simulations, estimated using covariance and apparent standard deviation as Eq. (III.7), and estimated using autocorrelation coefficient as Eq. (III.9). As shown in the figure, real standard deviation estimated using Eq. (III.7) matches very well for all cycles, and the real standard deviation estimated using Eq. (III.9) matches after about 100 cycles. Figure III-5 shows the real to apparent standard deviation for three real standard deviations.
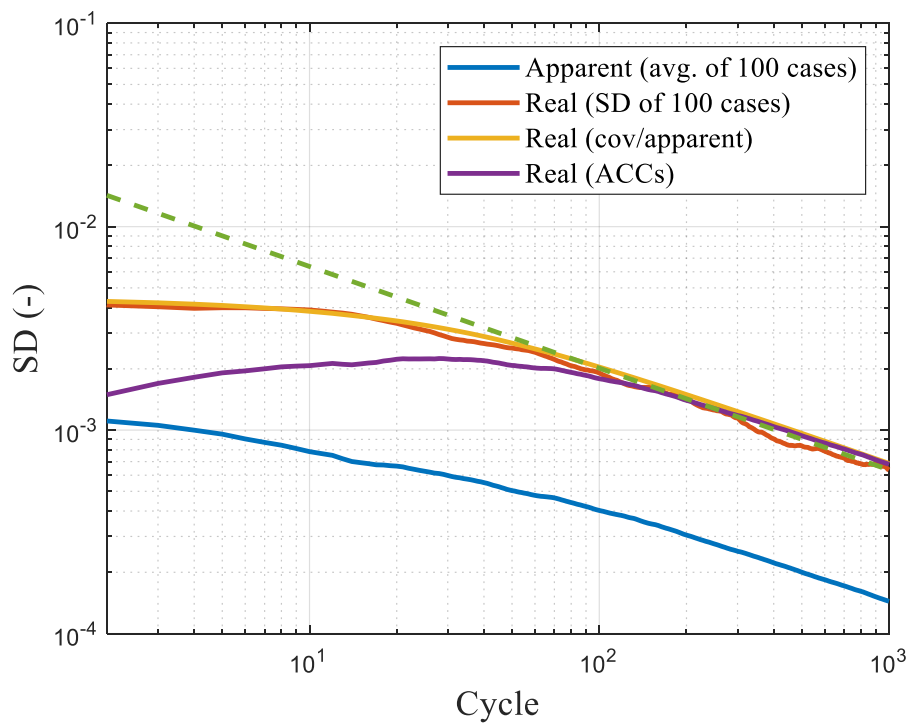
Figure III-4: Real and apparent standard deviation of nu-fission in half region for 1D1G problem.
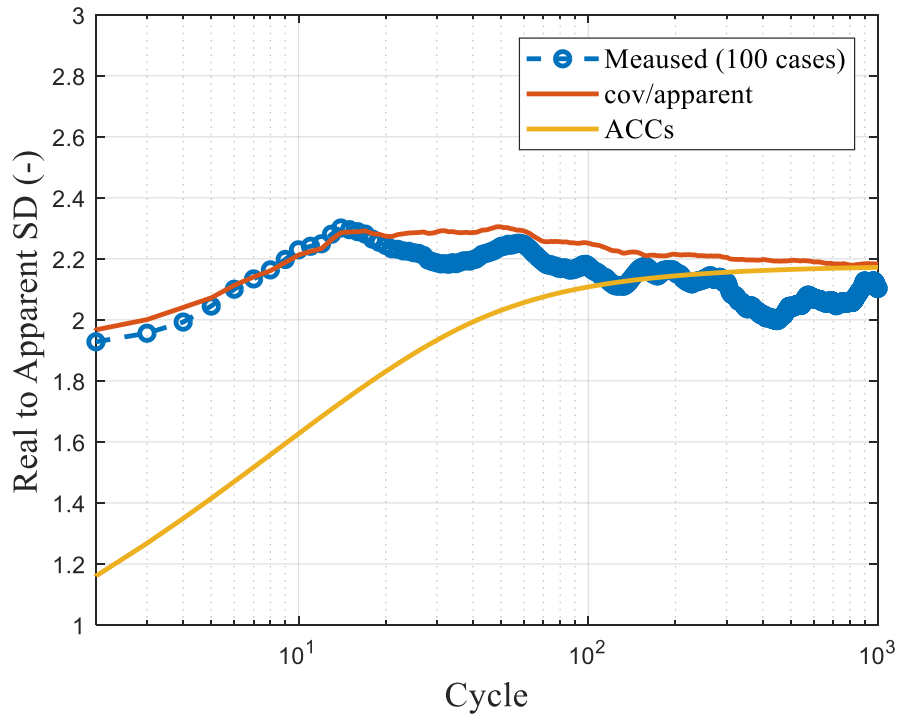
Figure III-5: Real to apparent standard deviation of nu-fission in half region for 1D1G problem.

3.3. Subcycle Method

MCS uses subcycle method to reduce the gap between apparent standard deviation and real standard deviation. Subcycle method simply runs more cycles in one cycle. It should be noted that the subcycle method would produce almost identical solution as batch method. When subcycle is employed, the tally quantity at cycle *i* is the average of tally quantity during *L* subcycle as follows:

$$Q^i = \frac{1}{L}\sum_{l=1}^{L} Q^{i,l} \quad .$$

(III.10)

Figure III-6 shows the program flow of subcycle method in MCS. During the subcycle, MCS only runs the particle transport without statistical process and feedbacks.

Algorithm Subcycle Program Flow
do i_cycle = 1, n_cycles
do i_sub_cycle = 1, n_subcycles
synchronize neutron bank
do i_history = 1, n_histories
initialize particle
transport particle
end do
end do
estimate the result and do statistics
perform feedbacks if requries
end do

Figure III-6: Program flow of subcycle.

3.3.1. Underestimation of Variance with Subcycle

The tally quantity at cycle i by employing L subcycle, Q_L^i, can be expressed as follow:

$$Q_L^i = \frac{1}{L}\sum_{l=1}^{L} Q^{i,l} = \frac{1}{L}\sum_{g=L(i-1)+1}^{iL} Q^g \quad, \tag{III.11}$$

where g is the global subcycle index. The covariance of cycle Q_L^i can be expressed with the covariance of cycle Q^i as follows:

$$\begin{aligned}
\mathrm{cov}_k\left[Q_L^i\right] &= E\left(\sum_i\left(\frac{1}{L}\sum_{l=1}^{L}Q^{i,l} - \overline{Q}\right)\left(\frac{1}{L}\sum_{l=1}^{L}Q^{i+k,l} - \overline{Q}\right)\right)\\
&= \frac{1}{L^2}E\left(\sum_i\left(\sum_{l=1}^{L}Q^{i,l} - L\overline{Q}\right)\left(\sum_{l=1}^{L}Q^{i+k,l} - L\overline{Q}\right)\right)\\
&= \frac{1}{L^2}E\left(\sum_i\left(\sum_{l=1}^{L}Q^{L(i-1)+l} - L\overline{Q}\right)\left(\sum_{l=1}^{L}Q^{L(i+k-1)+l} - L\overline{Q}\right)\right)\\
&= \frac{1}{L^2}\left(\sum_{i=1}^{L-1}i\left(\mathrm{cov}_{L(k-1)+1}\left(Q^i\right) + \mathrm{cov}_{2L(k)+1-i}\left(Q^i\right)\right) + L\,\mathrm{cov}_{L(k)}\left(Q^i\right)\right)\\
&= \frac{1}{ML^2}\left(\sum_{i=1}^{L-1}i\left(C_{L(k-1)+1} + C_{2L(k)+1-i}\right) + LC_{M(k)}\right)
\end{aligned} \tag{III.12}$$

where M is the number of histories per one subcycle. The covariance decreases as lag k increase exponentially. The covariance after lag S can be ignored for large S. For subcycle L larger than S, the covariance of lag k ($k>2$) can be negligible, and the covariance of lag 1 can be expressed as follows:

$$\mathrm{cov}_1\left[Q_L^i\right] \cong \frac{1}{ML^2}\sum_{i=1}^{S}i\left(C_{L(k-1)+1} + C_{2L(k)+1-i}\right) = \frac{A}{ML^2} \quad. \tag{III.13}$$

The Eq. (III.6) can be simplified for sufficiently large L as follows:

$$\sigma^2\left[\overline{Q}\right] - \sigma_A^2\left[\overline{Q}\right] = \frac{2}{N}\mathrm{cov}_1\left[\overline{Q}^i\right] \cong \frac{2}{N}\frac{A}{ML^2} \quad. \tag{III.14}$$

The real to apparent variance is expressed as follows:

$$\frac{\sigma^2\left[\overline{Q}\right]}{\sigma_A^2\left[\overline{Q}\right]} = \frac{\sigma^2\left[\overline{Q}\right]}{\sigma^2\left[\overline{Q}\right] - \dfrac{2}{N}\dfrac{A}{ML^2}} \quad . \tag{III.15}$$

It should be noted that the real variance and the summation of C_k, A, are independent of number of subcycle and histories per subcycle.

45

3.3.2. Numerical Tests

Numerical test is performed using same 1D1G problem in the section 3.2.2. As explained, real to apparent ratio is depending on number of subcycle L and it can be estimated using Eqs. (III.7) and (III.15). Figure III-7 shows estimated real to apparent standard deviation by using two equations. As shown in the figure, Eq. (III.15) matches very well for $L > 50$.
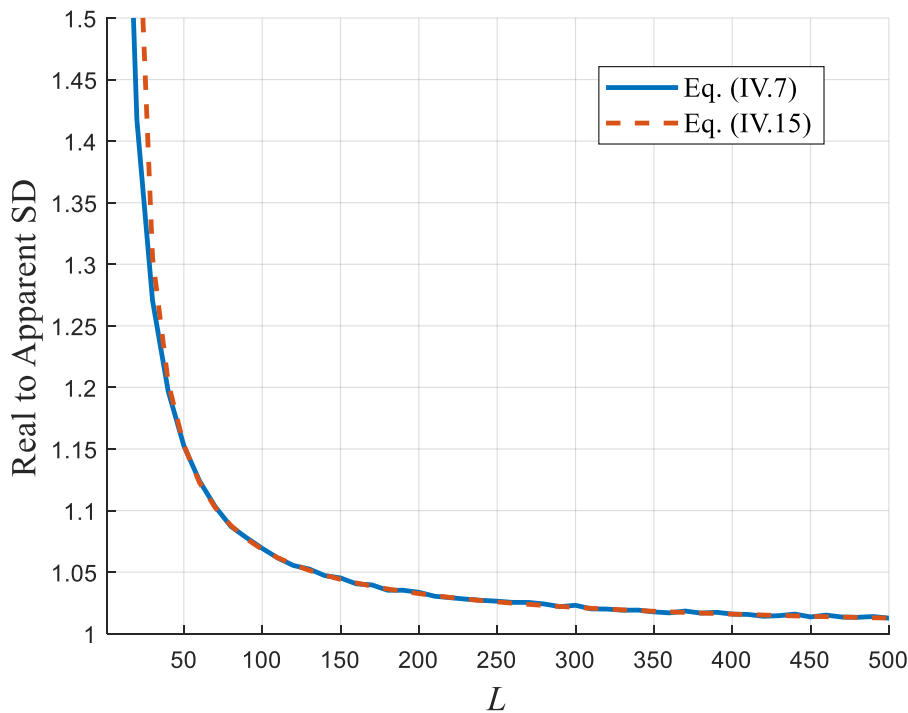
Figure III-7: Real to apparent standard deviation depending on subcycle length L.

The real to apparent standard deviation is compared with measured value from 100 independent simulation employing four different calculation parameters:

- C1: 200 inactive cycles, 1,000 active cycles, 1 subcycles, 90,000 histories per subcycle
- C2: 200 inactive cycles, 1,000 active cycles, 30 subcycles, 3,000 histories per subcycle
- C3: 200 inactive cycles, 1,000 active cycles, 100 subcycles, 900 histories per subcycle
- C4: 200 inactive cycles, 1,000 active cycles, 900 subcycles, 100 histories per subcycle

Figure III-8 shows the real to apparent SD. Solid line represent the measured ratio and the dashed line represent the estimated value by Eq. (III.15). As shown in the figure, estimated ratio matches well with measured value after about 100 cycles.

46
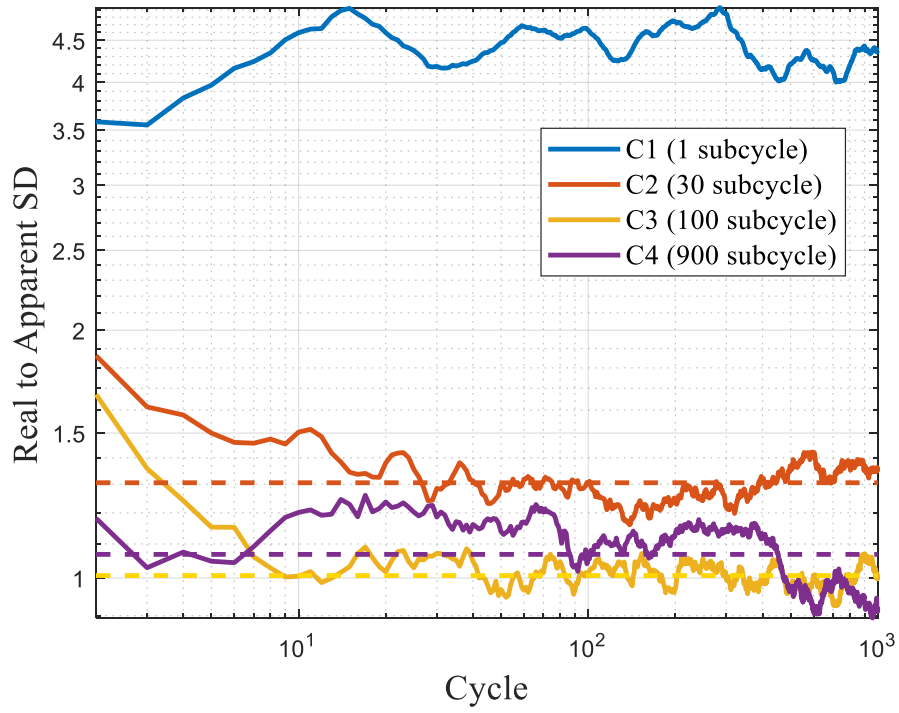
Figure III-8: Real to apparent standard deviation with different number of subcycles for 1D1G problem.

3.4. Study on BEAVRS

Prior to the power reactor simulation, impact of inter-cycle correlation on BEAVRS quarter core geometry is examined to decide number of subcycles. The simulation conditions were as below

- Geometry: BEAVRS quarter core.
- State: Beginning of Cycle (BOC), Hot Zero Power (HZP).
- Library: ENDF-VII.0.
- Temperature: 600K for all regions.
- # of axial meshes per pin: 10.
- # of radial mesh per pin: 1.
- Tallies: assembly wise power, pin wise power, and mesh wise power.
- # of simulation for estimation of real and apparent variance: 35.

The simulation was performed by employing 200 inactive cycles, 300 active cycles, 1 subcycle, 300,000 histories per subcycle (total histories in active cycles = $300 \times 300,000 = 90,000,000$). As revealed from previous researches, the ratio of real and apparent is getting larger with bigger mesh size. Three sizes of meshes were selected for testing: assembly wise, pin wise, and mesh wise (10 meshes per pin). Figure III-9 shows the probability distribution of real and apparent standard deviation. As shown in the figure, distribution of apparent standard deviation has three peaks which cannot be explained while real standard deviation shows smooth trend. This may be the impact of higher order eigen modes, but it should be studied in future. Figure III-10 shows the probability distribution of real to apparent ration. It should be noted that the mean value of the real to apparent ratio is little above than 1.0 which means that there is impact on inter-cycle correlation even for the mesh wise tally. Figure III-11 shows the probability density of real and apparent standard deviation for pin-wise power. In this case, both shows smooth distribution, but the apparent distribution shows smaller value and smaller deviation than real standard deviation. This difference is from the inter-cycle correlation, and the impact of the correlation is bigger with bigger size mesh. Figure III-12 shows the distribution of real to apparent standard deviation for pin-wise mesh. As shown in the figure, the real standard deviation tends to be larger than apparent at the boundaries. Figure III-13 presents the apparent and real standard deviation together with real to apparent ratio for assembly-wise power. As expected, it shows biggest different between two standard deviation. The maximum 6.4 times bigger real variance is observed than apparent variance.
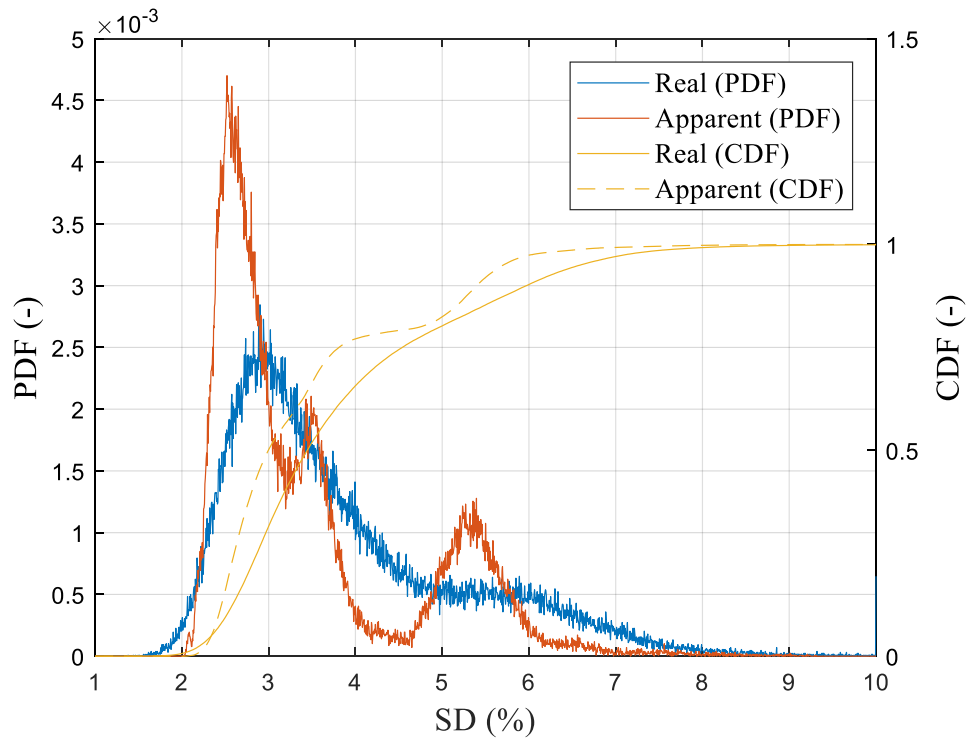
Figure III-9: Probability density of real and apparent standard deviation with one subcycle for mesh-wise power.
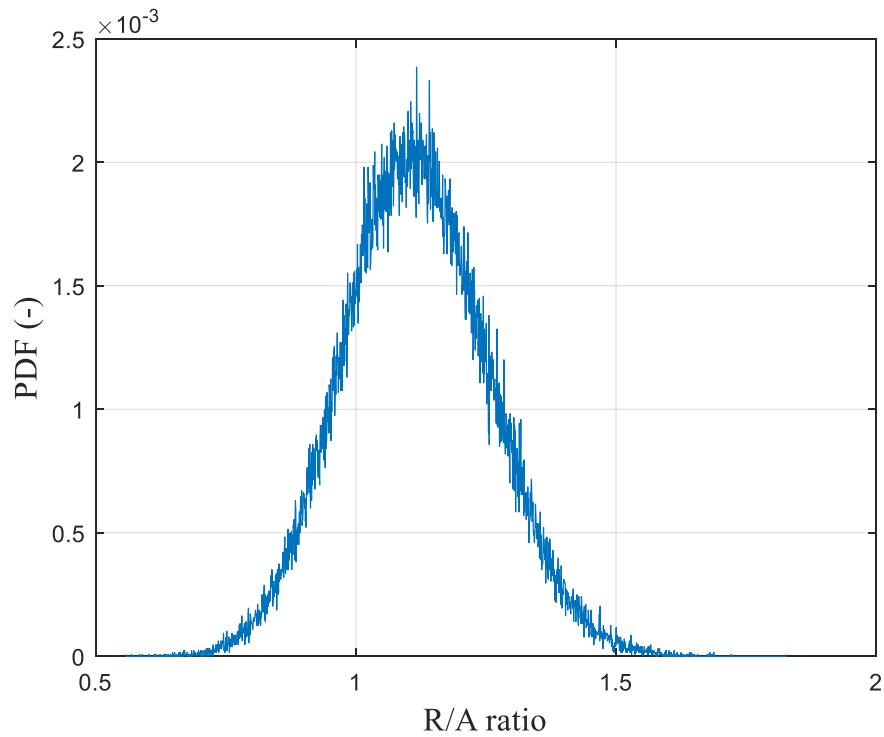
Figure III-10: Probability density of real to apparent ratio with one subcycle for meh-wise power.
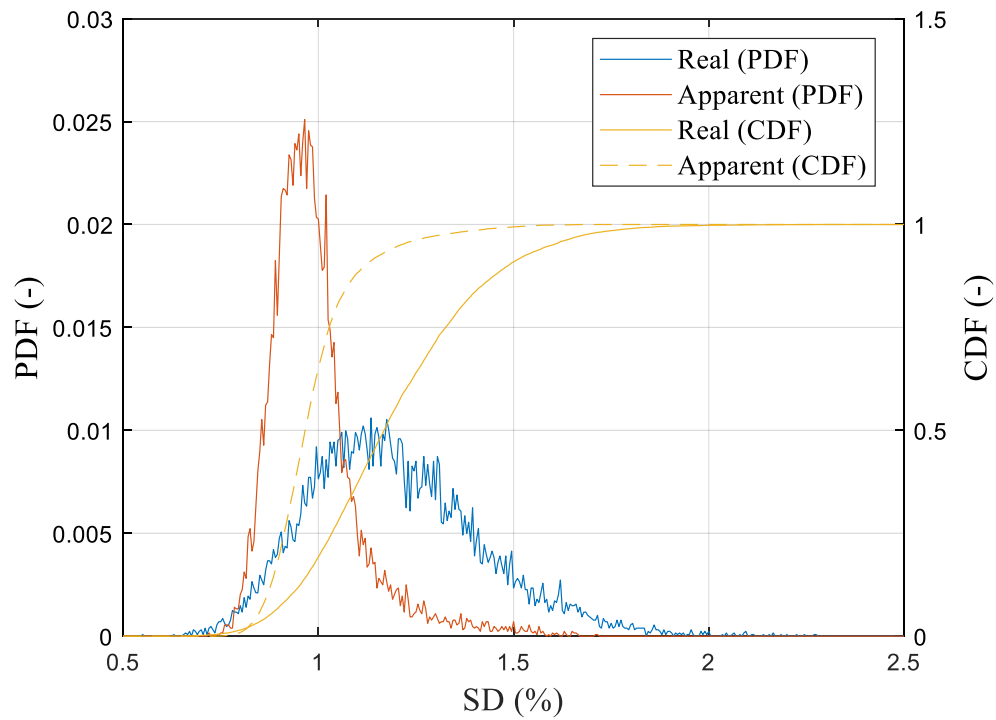
Figure III-11: Probability density of real and apparent standard deviation with one subcycle for pin-wise power.
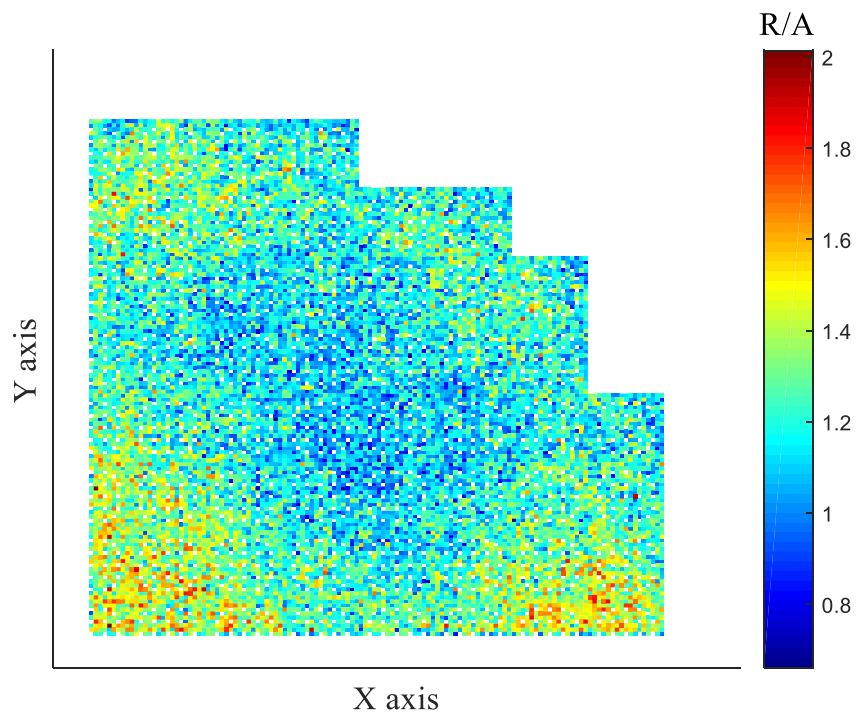
Figure III-12: Real to apparent ratio distribution for pin-wise power with one subcycle.

50

Figure III-13 data (each cell: Apparent (%) / Real (%) / R/A):

Legend: Apparent (%) · Real (%) · R/A

R/A	
Max	6.43
Min	2.66
RMS	4.21

0.20 / 1.09 / 5.40	0.16 / 0.93 / 5.87	0.15 / 0.79 / 5.38	0.15 / 0.65 / 4.35				
0.18 / 0.98 / 5.51	0.14 / 0.85 / 6.19	0.13 / 0.64 / 5.10	0.12 / 0.55 / 4.55	0.12 / 0.58 / 4.65	0.14 / 0.69 / 5.09		
0.17 / 0.83 / 4.80	0.13 / 0.68 / 5.25	0.12 / 0.49 / 4.17	0.11 / 0.38 / 3.44	0.11 / 0.50 / 4.56	0.11 / 0.65 / 5.74	0.14 / 0.69 / 5.03	
0.17 / 0.75 / 4.39	0.13 / 0.56 / 4.44	0.11 / 0.38 / 3.35	0.10 / 0.28 / 2.66	0.10 / 0.41 / 4.11	0.11 / 0.50 / 4.66	0.12 / 0.59 / 4.92	
0.17 / 0.73 / 4.25	0.13 / 0.64 / 4.98	0.11 / 0.47 / 4.09	0.11 / 0.32 / 2.97	0.10 / 0.34 / 3.25	0.11 / 0.44 / 4.05	0.12 / 0.59 / 4.97	0.15 / 0.70 / 4.77
0.18 / 0.96 / 5.28	0.13 / 0.81 / 6.11	0.12 / 0.61 / 5.07	0.12 / 0.53 / 4.63	0.11 / 0.40 / 3.50	0.12 / 0.46 / 3.90	0.12 / 0.65 / 5.31	0.15 / 0.72 / 4.99
0.20 / 1.10 / 5.55	0.15 / 0.97 / 6.43	0.13 / 0.86 / 6.37	0.13 / 0.68 / 5.16	0.13 / 0.53 / 4.17	0.13 / 0.57 / 4.38	0.13 / 0.77 / 5.73	0.16 / 0.81 / 5.19
0.27 / 1.17 / 4.34	0.20 / 1.10 / 5.53	0.18 / 0.98 / 5.43	0.17 / 0.79 / 4.50	0.17 / 0.67 / 3.86	0.17 / 0.66 / 3.80	0.18 / 0.79 / 4.48	0.20 / 0.84 / 4.23

Figure III-13: Real to apparent standard deviation for assembly-wise power with one subcycle.

The Auto Correlation Coefficients (ACCs) of assembly-wise power for selected 6 assembly positions shown in the Figure III-14 (D03, G04, A05, D06, G07, and A08) are shown in the Figure III-15. The ACCs from lag 1 to 100 are presented in. As shown in the figure, the ACCs at lag 1 is about 0.75 represent strong correlation. The ACCs decreases as lag increases, and ACCs is almost negligible for $k > 60$. Figure III-16 shows the convergence trends of RMS real and apparent standard deviation of assembly power. As expected, the deviation of real and apparent standard deviation is large.

Figure III-14: Selected positions for ACCs calculation.
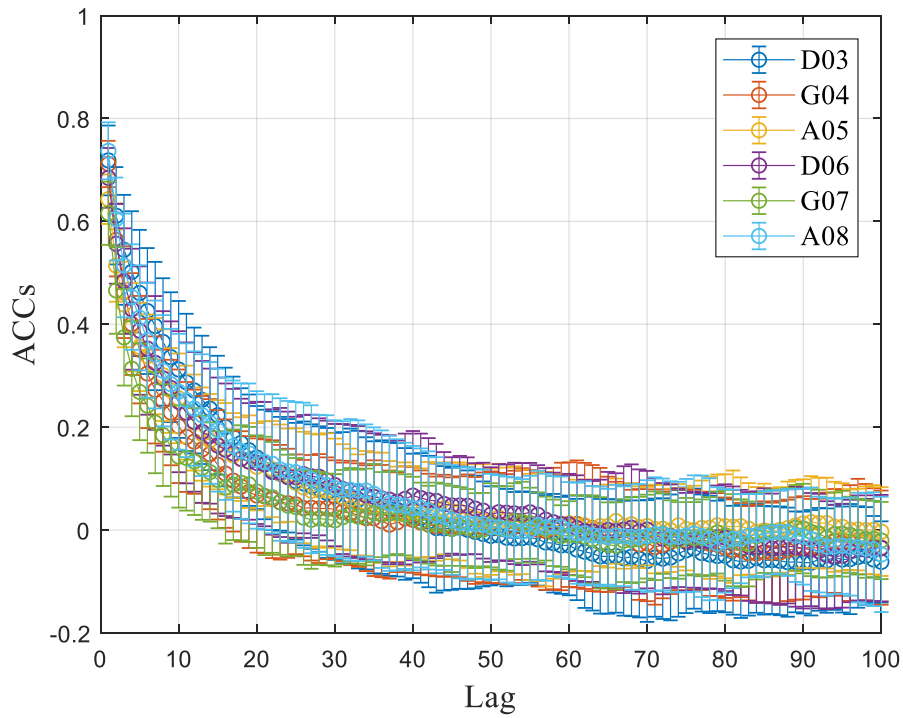
Figure III-15: ACCs for selected 6 assembly-wise powers one subcycle.
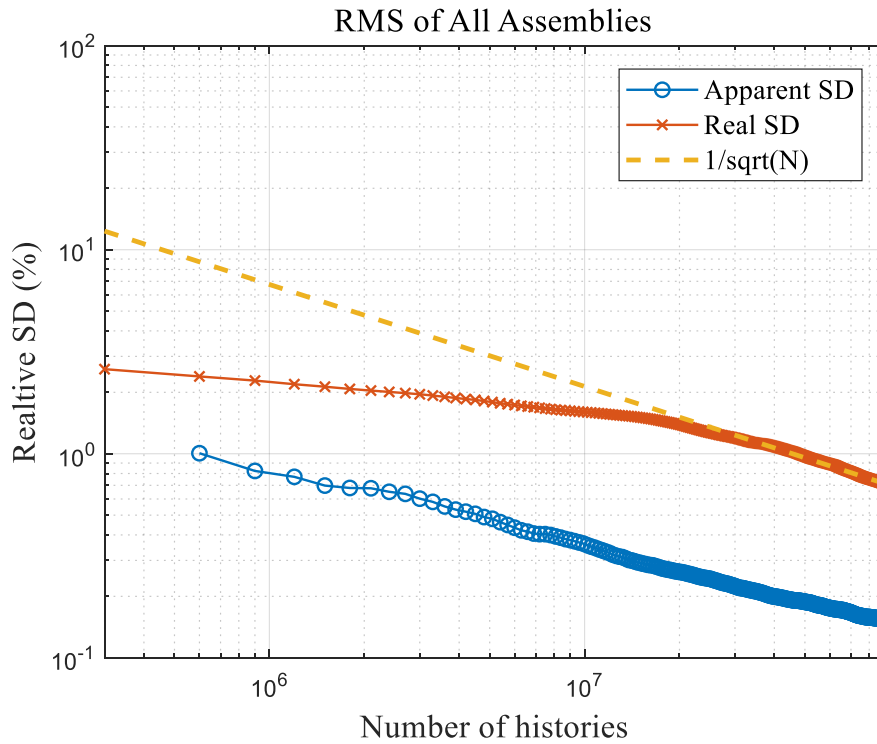
Figure III-16: Convergence of RMS real and apparent standard deviation of assembly-wise power.

To summarize the result with one subcycle:

- The apparent standard deviation is similar with it of real for mesh-wise tally.

- The real to apparent standard deviation increases as size of mesh increases (mesh → pin → assembly).

- The assembly-wise power standard deviation is underestimated 6.4 times.

- Two peaks are found which should be studied further in the future in the figure of probability density distribution of mesh-wise tally apparent standard deviation.

The real to apparent ratio depending on number of subcycle can be estimated by using measured variance and covariance with one subcycle as Figure III-7. The target real to apparent standard deviation 1.05 which requires at least 120 subcycles. However, 300 subcycle is chosen considering uncertainty of standard deviation and covariance used to estimate.
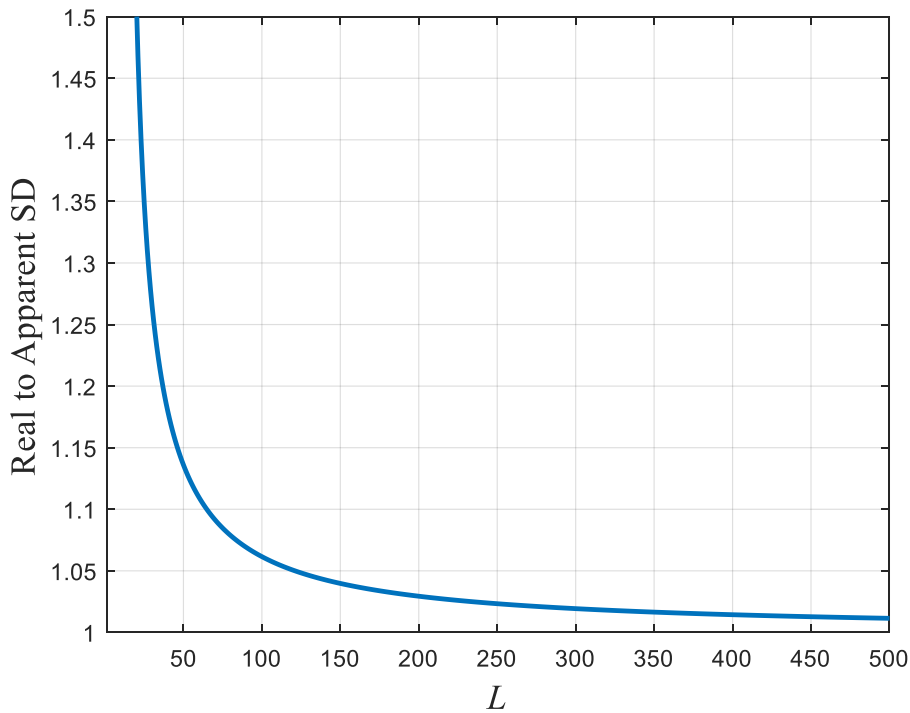
Figure III-17: Real to apparent ratio depending on L for BEAVRS quarter core.

The simulation is performed again by employing 200 inactive cycles, 300 active cycles, 300 subcycle, 1,000 histories per subcycle. (total histories in active cycles = $300\times300*1,000=90,000,000$) The standard deviation of mesh-wise power in Figure III-18 and Figure III-19 show similar trend as with one subcycle but the average ratio is moved to 1.0 represent the smaller inter-cycle correlation. Figure III-20 shows probability density of pin-wise power standard deviation. Unlikely previous case, the apparent standard deviation shows similar distribution with real standard deviation. The real to apparent ration also show smoother distribution as shown in Figure III-21 as expected.
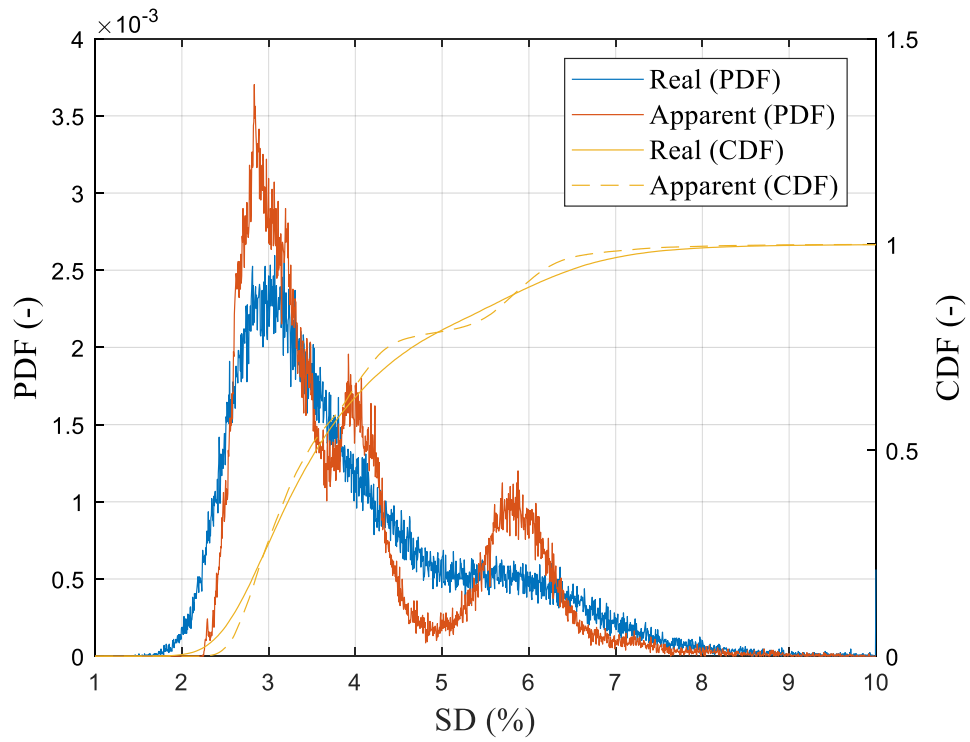
Figure III-18: Probability density of real and apparent standard deviation with 300 subcycles for mesh-wise power.
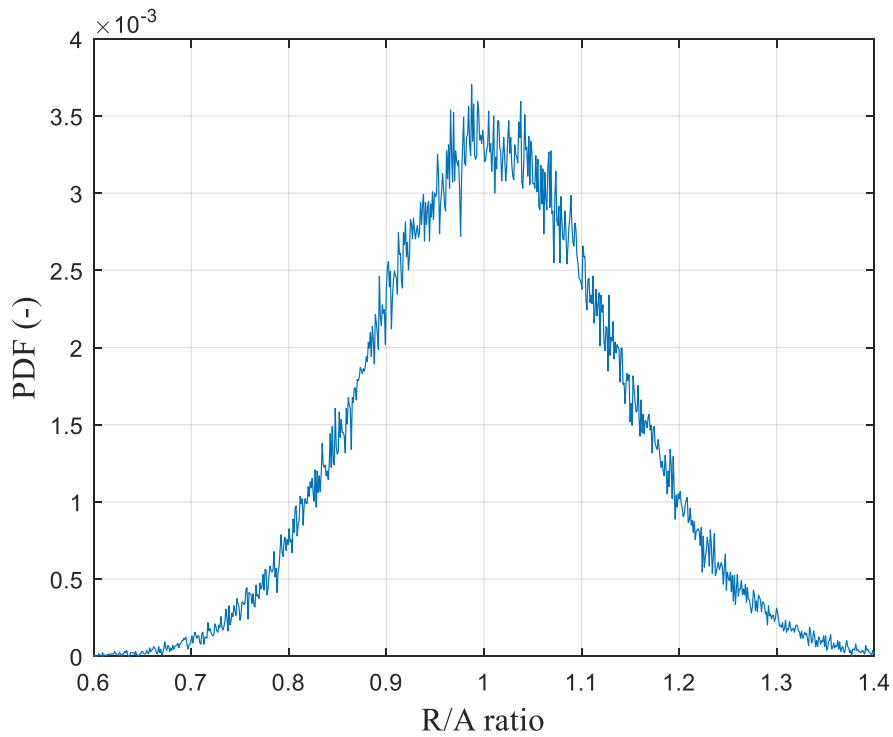
Figure III-19: Probability density of real to apparent ratio with 300 subcycles for meh-wise power.

55
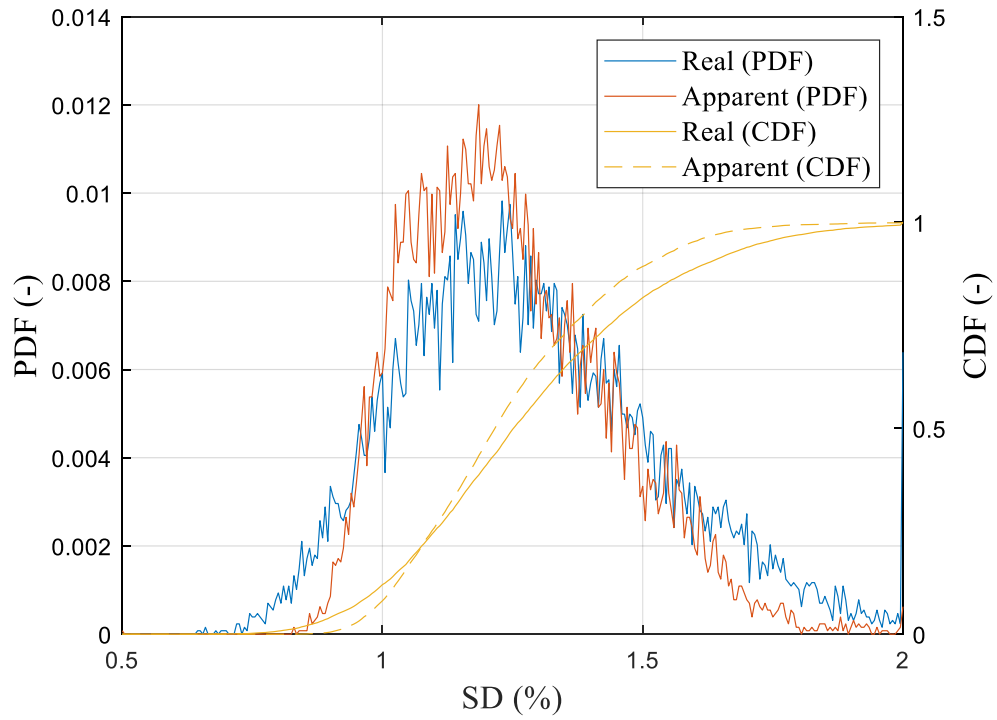
Figure III-20: Probability density of real to apparent ratio with 300 subcycles for pin-wise power.
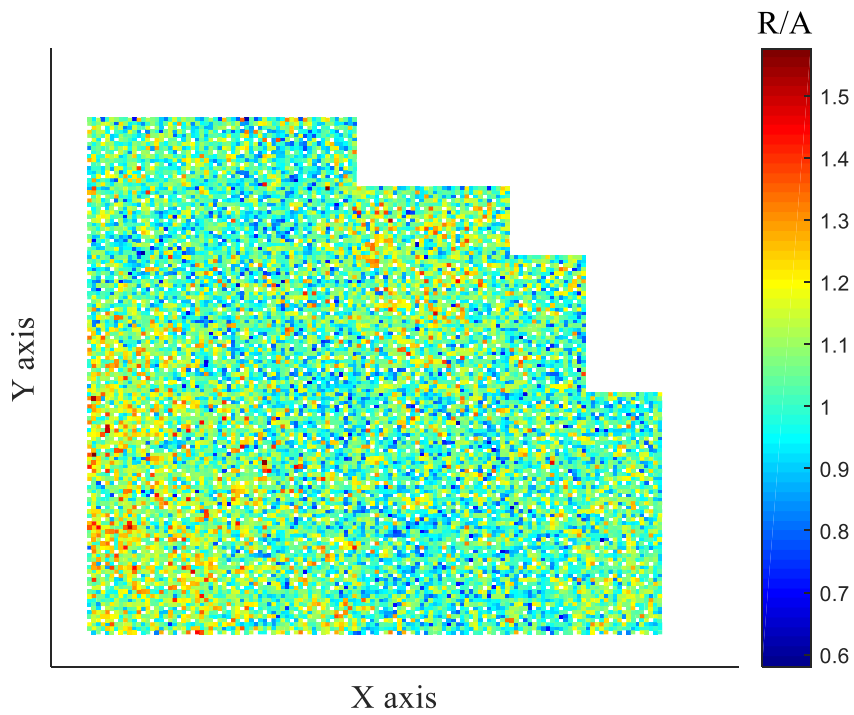
Figure III-21: Probability density of real to apparent ratio with 300 subcycles for pin-wise power.

The ACCs of assembly power for selected 6 assembly positions are presented in Figure III-22. As shown in the figure, the ACCs for all lag has no trend randomly fluctuating with small magnitude except lag 1. This ACCs represent that there is no significant correlation between tally realizations. This can explain the real and apparent ratio of assembly-wise power presented in Figure III-23. As shown in the figure, the real and apparent standard deviation shows similar magnitude and the ratio is close to 1.0.
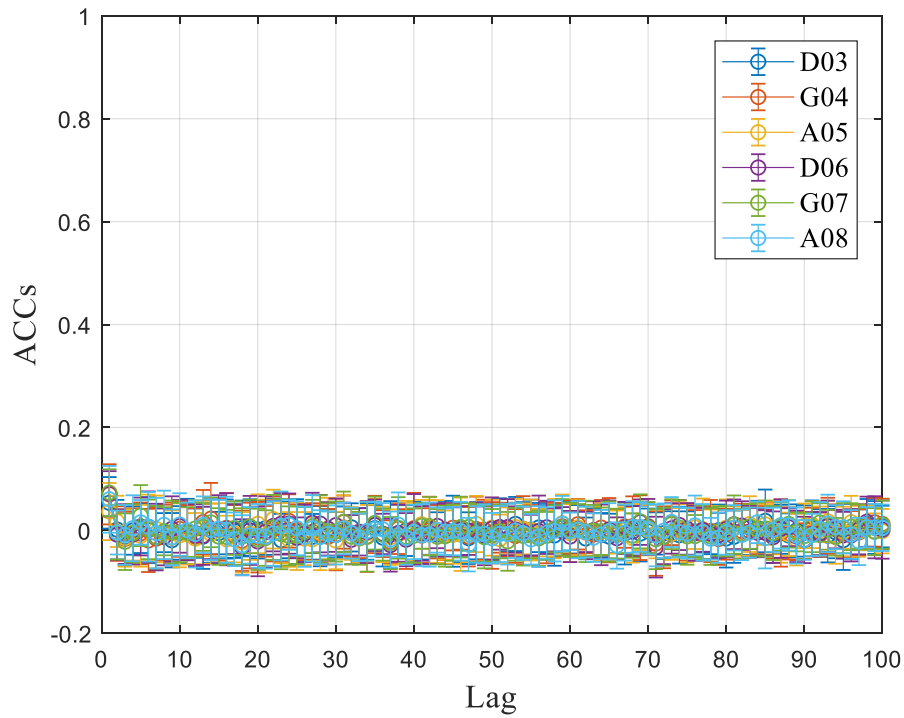
Figure III-22: ACCs for selected 6 assembly powers with 300 subcycle.

1.17	1.09	0.94	0.83					Apparent (%)
1.29	1.18	1.01	0.82					Real (%)
1.10	1.08	1.07	1.00					R/A

								R/A	
1.08	0.98	0.80	0.68	0.64	0.64			Max	1.32
1.09	0.99	0.85	0.72	0.66	0.68			Min	0.91
1.01	1.01	1.06	1.06	1.02	1.06			RMS	0.98

0.92	0.80	0.62	0.49	0.50	0.56	0.63
0.93	0.80	0.64	0.52	0.57	0.69	0.78
1.02	1.01	1.04	1.06	1.14	1.24	1.24

0.77	0.68	0.49	0.37	0.40	0.50	0.62
0.78	0.63	0.48	0.42	0.50	0.63	0.75
1.01	0.93	0.97	1.14	1.24	1.28	1.22

0.79	0.66	0.47	0.36	0.37	0.50	0.66	0.81
0.96	0.76	0.52	0.33	0.34	0.54	0.69	0.78
1.22	1.15	1.10	0.93	0.91	1.08	1.04	0.97

0.90	0.77	0.58	0.47	0.48	0.62	0.81	0.93
1.04	0.91	0.73	0.58	0.52	0.66	0.79	0.96
1.16	1.17	1.25	1.22	1.08	1.07	0.97	1.03

1.00	0.89	0.75	0.65	0.66	0.80	0.96	1.10
1.19	1.13	0.95	0.82	0.81	0.82	0.96	1.18
1.18	1.27	1.26	1.26	1.22	1.02	1.00	1.07

1.17	1.03	0.85	0.76	0.74	0.89	1.05	1.20
1.35	1.30	1.05	1.00	0.93	0.94	1.09	1.30
1.15	1.27	1.24	1.32	1.25	1.05	1.04	1.08

Figure III-23: Real to apparent standard deviation for assembly-wise power with 300 subcycle.

The convergence behavior for assembly-wise tally are checked to see whether it follows the $1/\sqrt{N}$. Since the inter-cycle correlation is small, the convergence slope must follow $1/\sqrt{N}$. The root mean square (RMS) of assembly power standard deviation are compared with ideal convergence slope in Figure III-24. It is verified that the real standard deviation follows ideal slope well, and the ratio of real and standard deviation matches well. To see the convergence slope of each assembly, the slopes are presented in Figure III-25 for selected 6 assemblies. The convergence slopes of 6 assemblies are also follows ideal slope as well.
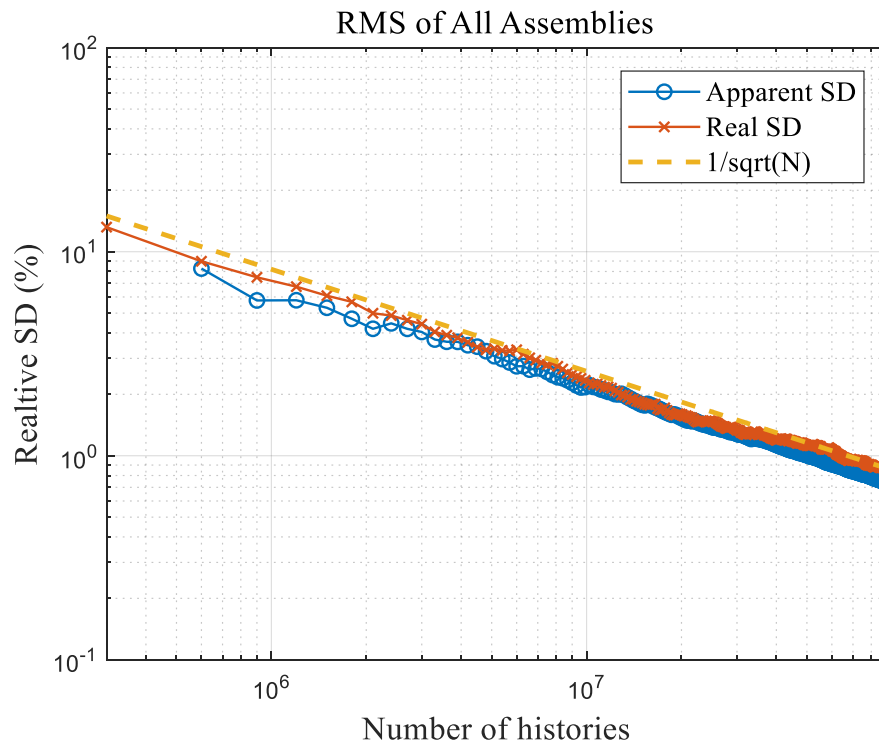
Figure III-24: RMS standard deviation of assembly-wise power with 300 subcycles.
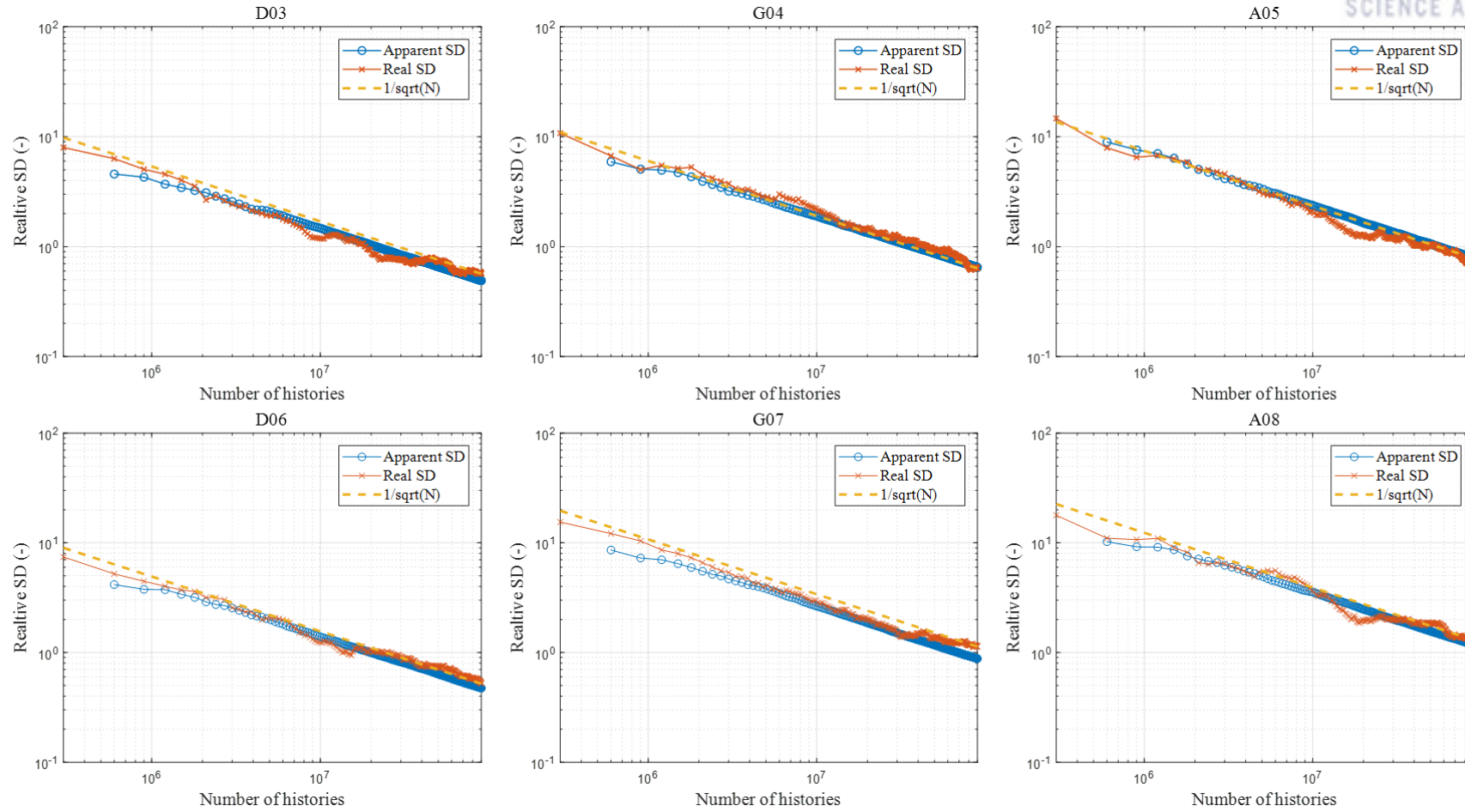
Figure III-25: Convergence slope of assembly-wise power standard deviation for selected 6 assemblies with 300 subcycles.

IV. Feedbacks for Power Reactor Simulation

4.1. Introduction

Five feedbacks are required at least for the power reactor simulation: depletion, equilibrium xenon, thermal hydraulics, on-the-fly calculation of Doppler broadened cross sections, and critical boron search. Figure IV-1 shows the feedback algorithm for power reactor simulation. The thermal hydraulics, xenon number density, and critical boron concentration will be updated at the end of every neutron transport cycle, and the number density of nuclides will be updated at the end of every burnup step. Following chapters will describe the feedbacks implemented in MCS.
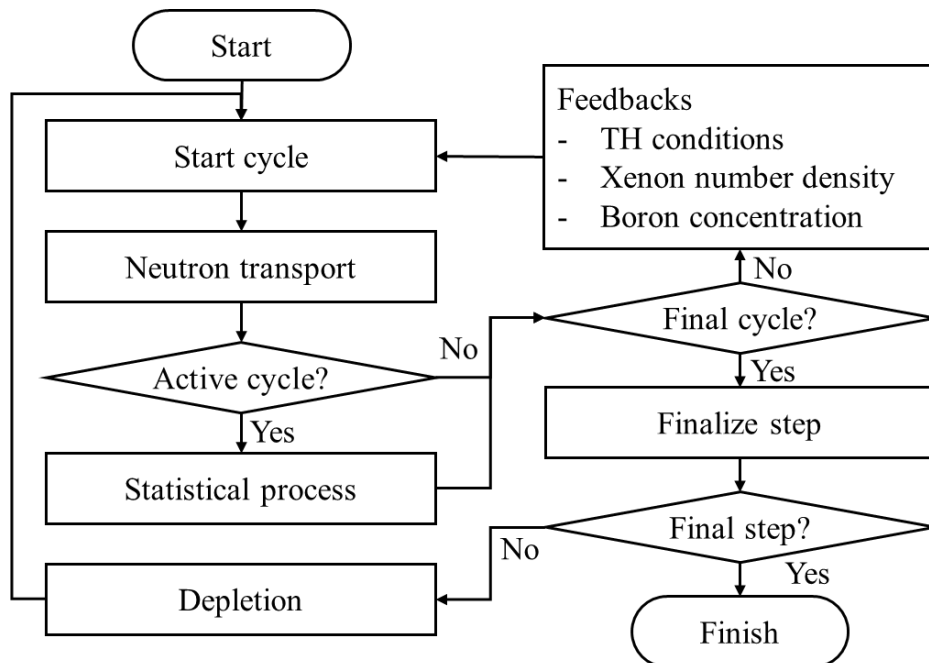
Figure IV-1: Feedback algorithm for power reactor simulation.

4.2. Depletion

The transmutation of nuclides by decay, fission, and absorption can be expressed as following:

$$\frac{dN_i}{dt} = \sum_j \gamma_{j \to i} \sigma_{f,j} N_j \phi + \sigma_{c,i-1} N_{i-1} \phi + \sum_k \lambda_{k \to i} N_k - \sigma_{a,i} N_i \phi - \lambda_i N_i \quad , \qquad (IV.1)$$

where N_i is the number density of nuclide i, $\gamma_{j \to i}$ is fission yield of nuclide i from nuclide j, $\sigma_{f,j}$ is the fission micro cross section of nuclide j, $\sigma_{c,i-1}$ is the capture micro cross section of nuclide $i-1$, $\sigma_{a,j}$ is the absorption micro cross section of nuclide j, and $\lambda_{k \to i}$ is the decay constant of nuclide k to i.

Table IV-1 shows the brief description of MCS burnup capability. MCS employs the Chebyshev Rational Approximation Method (CRAM) to solve the burnup equation. The decay constants and fission yield data are from various library including ENDF-VIII.0, ENDF-VII.1, ENDF-VII.0, and JEFF-3.1.1. Since MCS can read the raw data without modification, other library can be used directly without modification. There are data for 3,820 nuclides exist. However, MCS uses only 1,373 nuclides for burnup calculation as default. The number of nuclides and burnup chain can be modified by user. MCS tallies 6 types of reaction rates during transport simulation: *(n,γ)*, *(n,2n)*, *(n,3n)*, *(n,α)*, *(n,p)*, and 3 group fission reaction rates.

Table IV-1: Overview of Burnup Function in MCS.

Solver	CRAM
Decay constant	ENDF-VIII.0, ENDF-VII.1, NDF-VII.0
Fission yield	ENDF-VIII.0, ENDF-VII.1, NDF-VII.0
Ternary fission yield	JEFF-3.1.1
Spontaneous fission yield	ENDF-VIII.0, ENDF-VII.1, NDF-VII.0
Ternary spontaneous fission yield	JEFF-3.1.1
# of isotopes in the decay chain	1,373
Neutron induced transmutations	*(n,γ)*, *(n,2n)*, *(n,3n)*, *(n,α)*, *(n,p)*, fission
Burnup strategy	Predictor Predictor-corrector Semi predictor corrector
Option	Quadratic depletion Equilibrium xenon

Three types of burnup algorithms are implemented in MCS: predictor, predictor-corrector, and semi predictor-corrector. Among them, the semi-predictor corrector algorithm is uses as a default. Table IV-2 shows the data flor of semi predictor-corrector.

Table IV-2: Data Flow of Semi Predictor-Corrector Algorithm.

Time	Calculation	I/O	Number Density	Reaction Rate
0 (initial)	Transport (P)	In	N_0	-
		Out	-	-
	Depletion (P)	In	N_0	$R_{0,p}$
		Out	$N_{1,p}$	-
	Transport (C)	In	N_1	-
		Out	-	$R_{0,c}$
	Depletion (C)	In	N_0	$R_{0,c}$
		Out	$N_{1,c}$	-
	Result	-	$N_1 = (N_{1,p} + N_{1,c})/2$	-
t-1	Transport (P)	In	-	-
		Out	-	-
	Depletion (P)	In	N_{t-1}	$R_{t-1,c}$
		Out	$N_{t,p}$	-
	Transport (C)	In	N_{t-1}	-
		Out	-	$R_{t,c}$
	Depletion (C)	In	N_{t-1}	$R_{t,c}$
		Out	$N_{t,c}$	-
	Result	-	$N_t = (N_{t,p} + N_{t,c})/2$	-
t	Transport (P)	In	-	-
		Out	-	-
	Depletion (P)	In	N_t	$R_{t,c}$
		Out	$N_{t+1,p}$	-
	Transport (C)	In	N_t	-
		Out	-	$R_{t+1,c}$
	Depletion (C)	In	N_t	$R_{t+1,c}$
		Out	$N_{t+1,c}$	-
	Result	-	$N_{t+1} = (N_{t+1,p} + N_{t+1,c})/2$	-

4.2.1. Numerical Tests

For the verification of burnup capability, VERA benchmark [48] 1C problem and 2C problem are selected. They are typical pin and assembly problem in Hot Full Power (HFP) state. VERA-1C problem is consist of single Westinghouse type 17×17 assembly fuel rod cell at BOC as shown in Figure IV-2. The materials composed of this problem are UO_2 in red, Zircaloy-4 in green, and borated water in blue. VERA-2C is assembly problem consisted of 1C fuel pins and guide tube as shown in Figure IV-3. There are 264 fuel pins and 25 guide tubes in assembly.
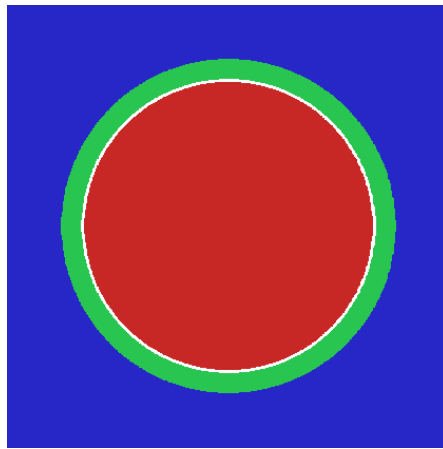
Figure IV-2: Configuration of VERA-1C pin.
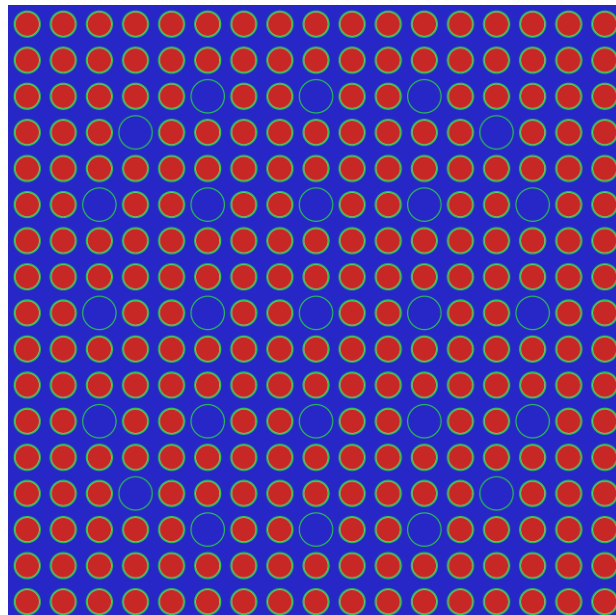
Figure IV-3: Configuration of VERA-2C assembly.

For the verification of MCS, Serpent 2.1.29 is used. Both MCS and Serpent simulations were performed by employing ENDF-VII.0 library of neutron cross sections, decay chain, and fission yield. The fuel pins in VERA-1C and 2C were divided into 3 radial rings makes 3 fuel meshes for 1C and 792 (=3×264) burnup meshes for 2C. Figure IV-4 shows the multiplication factor and 2sigma for VERA-1C problem by MCS and Serpent. Simulation was performed by employing 1 inactive cycle, 40 active cycles, and 100,000 histories per cycle. It was depleted using semi-predictor corrector up to 60 MWD/kgU with 40 burn steps. It is shown that the MCS follows the multiplication curves of Serpent very well within standard deviation.
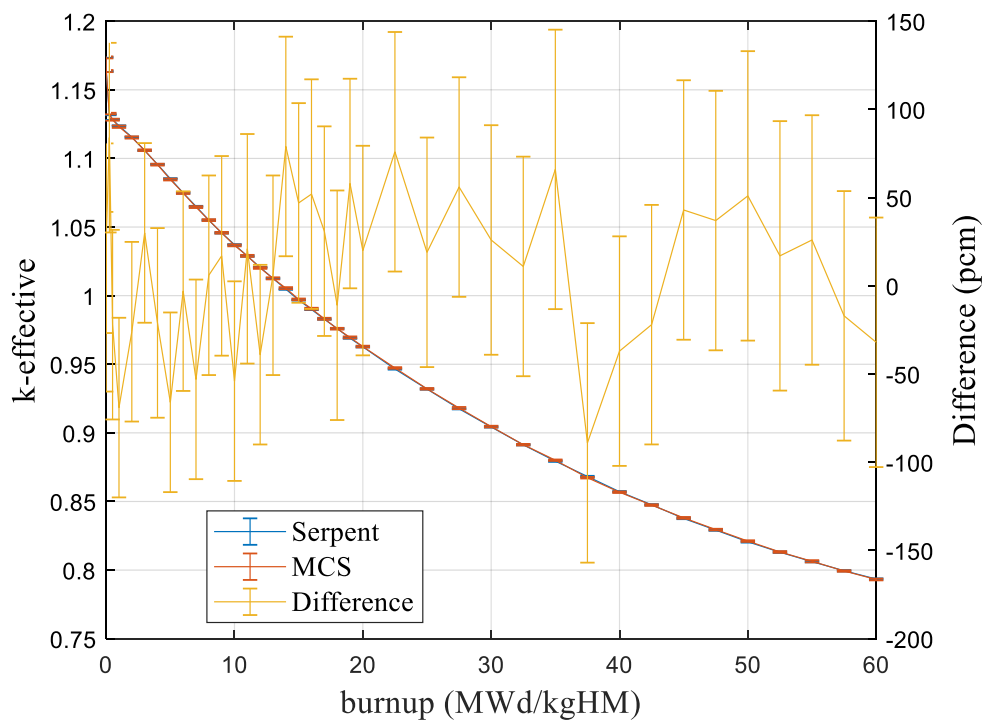
Figure IV-4: Multiplication factor for VERA-1C problem.

Figure IV-5 shows the multiplication factor and 2sigma for VERA-2C problem by MCS and Serpent. Simulation was performed by employing 40 inactive cycle, 160 active cycles, and 100,000 histories per cycle. It was depleted using semi-predictor corrector up to 50 MWD/kgU with 148 burn steps. It was shown that the MCS follows the multiplication curves of Serpent very well within standard deviation.
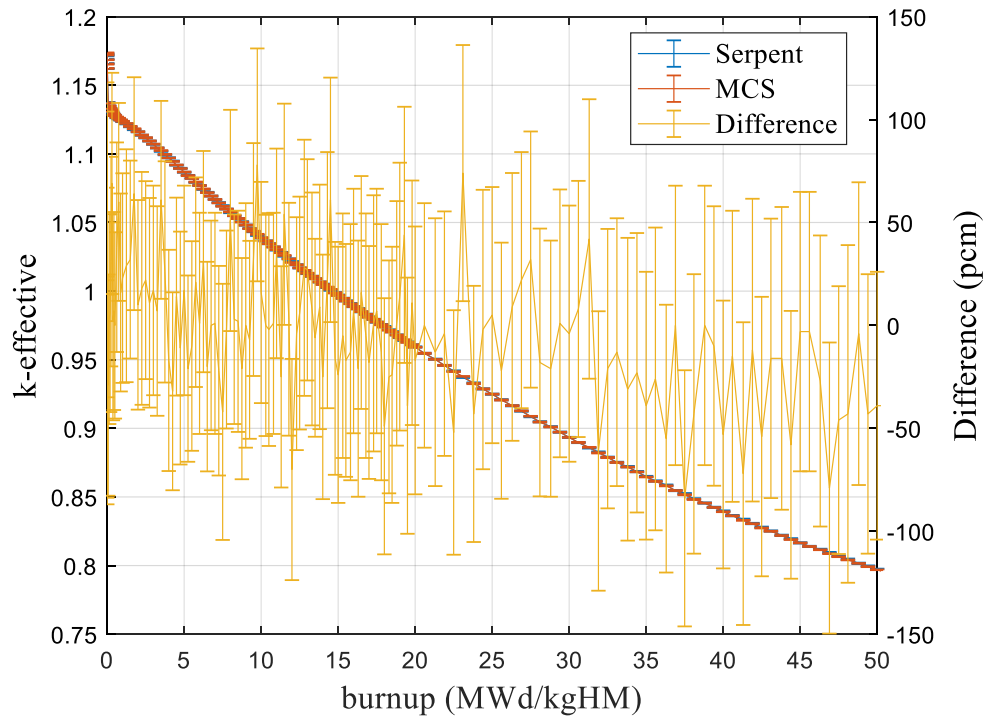
Figure IV-5: Multiplication factor for VERA-2C problem.

4.2.2.   Equilibrium Xenon Feedback

The spatial oscillation of flux was reported showing the MC burnup solutions are not spatially stable independent of burnup step size even for the simple symmetry pin geometry [49]. The spatial oscillation of flux is induced by the statistical uncertainty of xenon density which has very large thermal absorption cross section. Griesheimer proposed the in-line xenon update algorithm to prevent the xenon induced oscillation [50]. He updates the xenon number density at the end of every transport cycle by using the tallied quantities during cycle as to the following equilibrium density:

$$n_I = \frac{\sum\limits_{i=nuclides} \gamma_{i,I} R_{i,f}}{\lambda_I} \quad , \tag{IV.2}$$

$$n_{Xe} = \frac{\sum\limits_{i=nuclides} (\gamma_I + \gamma_{Xe}) R_f}{\lambda_{Xe} + \sigma_{Xe,a}\phi} \quad , \tag{IV.3}$$

where n_I is the number density of ^{135}I in equilibrium state, n_{Xe} is the number density of ^{135}Xe in equilibrium state, γ_I is the cumulative fission yield of ^{135}I, and γ_{Xe} is the cumulative fission yield of ^{135}Xe, λ_I is the decay constant of ^{135}I, λ_{Xe} is the decay constant of ^{135}Xe, R_f is fission reaction rate, and $\sigma_{Xe,a}$ is the absorption cross section of ^{135}Xe. The equilibrium xenon feedback function is very effective to prevent the xenon oscillation. However, the solution may not be reliable during the xenon buildup period. Yang proposed the improved xenon feedback algorithm [51] considering the xenon density changes during buildup period. Equilibrium xenon feedback function is implemented into MCS since the target purpose of this function is to prevent xenon oscillation at the steady state. Later, the improved algorithm will be implemented for the transient simulation.

When equilibrium xenon feedback is used, MCS first prepare the cumulative fission yield of ^{135}I and ^{135}Xe. The assumption is that all precursors of ^{135}I will decay to ^{135}I without absorption. Figure IV-6 shows the decay chain of ^{135}I which is considered in MCS to prepare fission yield.
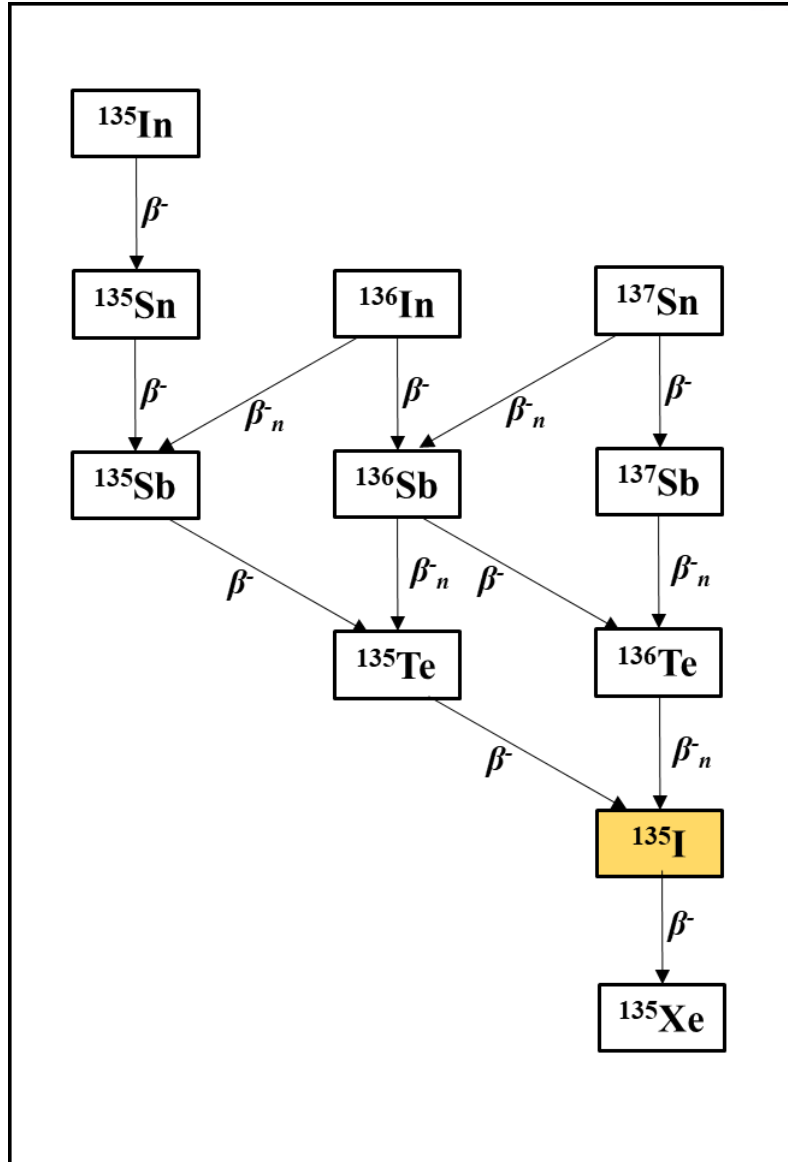
Figure IV-6: Decay chain of ^{135}I.

The density calculated by the equilibrium xenon function and the one from burnup solver must be same. This can be confirmed by comparing two solutions with and without xenon feedback against the problem which does not have oscillation. VERA-1C problem is selected for the verification. VERA-1C is 2-dimentional pin problem at hot full power state which does not have oscillation issue at all. Figure IV-7 and Table IV-3 shows the *k-effective* with and without equilibrium xenon feedback up to 3MWD/kgHM. The *k-effective* without equilibrium xenon decrease rapidly at beginning because of xenon buildup. Third depletion step is at 6.25 days that xenon density is saturated. Thus, the solutions are same after third depletion burnup step. This proves the MCS equilibrium xenon function updates the xenon number density same as depletion solver implemented in MCS.
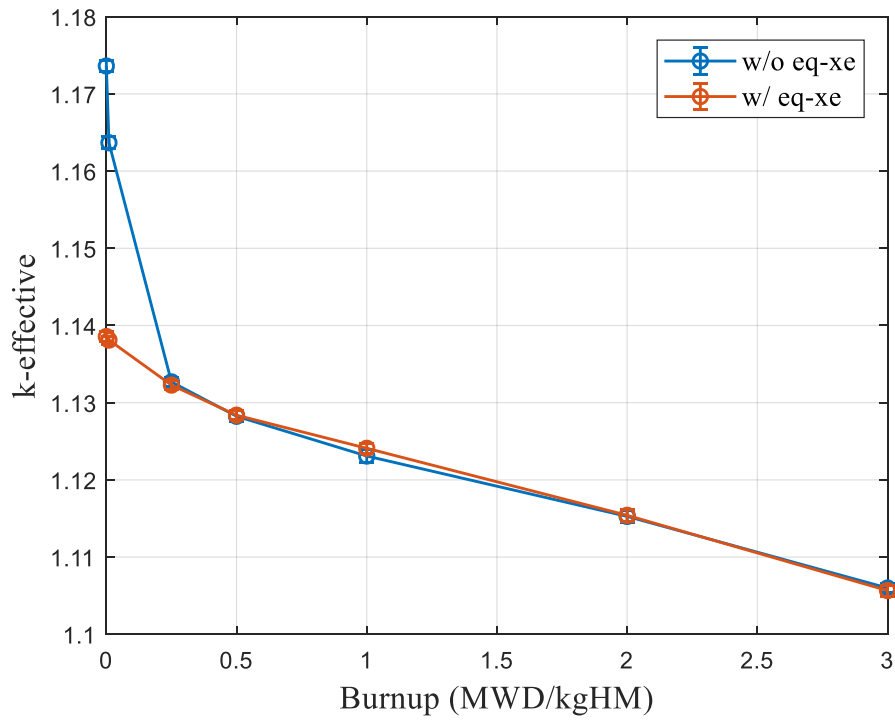
Figure IV-7: VERA-1C result with and without equilibrium xenon feedback.

Table IV-3: VERA-1C Result with and without Equilibrium Xenon Feedback.

EFPD (days)	Burnup (MWD/kgHM)	w/o eq-xe		w/ eq-xe		Diff. (pcm)
		k_{eff}	SD	k_{eff}	SD	
0.00	0.00	1.17361	0.00036	1.13857	0.00033	-3504
0.25	0.01	1.16367	0.00039	1.13811	0.00026	-2556
6.25	0.25	1.13269	0.00029	1.13228	0.00029	-41
12.50	0.50	1.12824	0.00036	1.12838	0.00031	14
25.00	1.00	1.12309	0.00043	1.12409	0.00032	100
50.00	2.00	1.11527	0.00041	1.11541	0.00038	14
75.00	3.00	1.10599	0.00031	1.10566	0.00036	-33

4.2.3. Memory Requirement

In MCS, memory requirement for each burnup cell containing 251 nuclides is approximately 82KB estimated as follows:

- material variables: $251×2×8$bytes$+251×2×4$bytes $=6,024$bytes
- reaction rates for scoring: $251×9×8$bytes $= 18,072$bytes
  (3 group fission, absorption, (n,γ), (n,2n), (n,3n), (n,α), (n,p))
- reaction rates for statistical process: $251×9×2×8$bytes $= 36,144$bytes
- number densities used in CRAM solver: $1,373×2×8$bytes $=21,968$bytes

Among burnup related variables, material variables and reaction rates for scoring must be allocated in all processors in parallel simulation. However, the reaction rates for statistical process and number densities used in CRAM solver can be allocated in only one processor. Thus, the memory requirement for burnup simulation is expressed as follows:

$$M_{burnup} = \left(M_{All} + \frac{M_{One}}{NP} \right) \times N_c \quad , \tag{IV.4}$$

where M_{all} is 24kB, M_{one} is 58kB, N_c is the number of burnup cells and NP is the number of processors. The dependence of M_{burnup} in Eq. (IV.4) on the number of burnup cells and the number of processors is illustrated in Figure IV-8. Noticeably, the required memory per processor decreases as the number of processors increases.
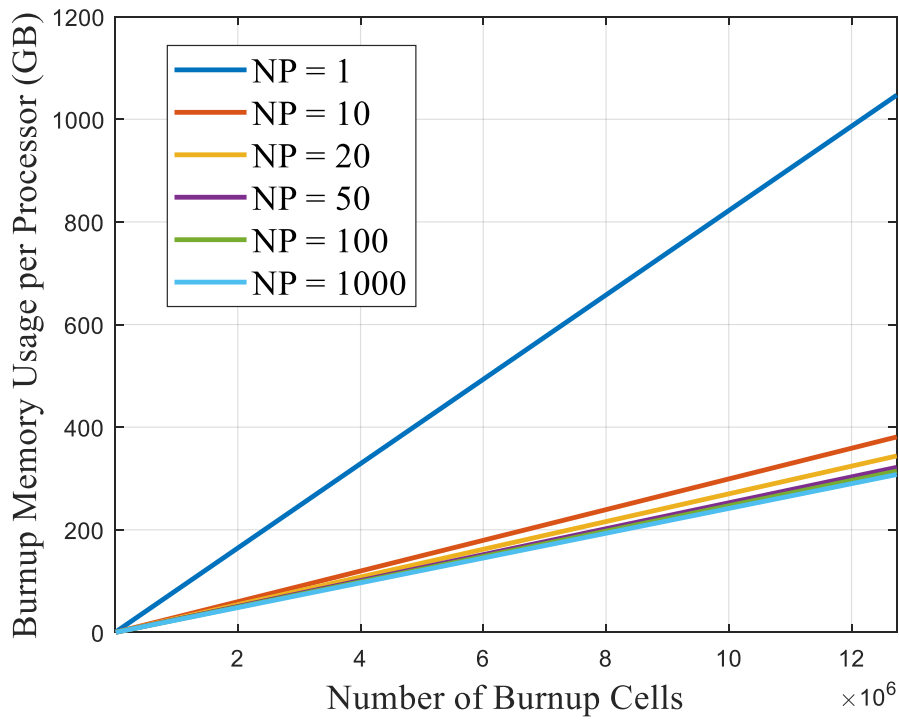
Figure IV-8: Memory requirement per processor for depletion calculation for different number of processors and burnup cells.

4.3.   On-The-Fly Doppler Broadening

In the coupled framework of Monte Carlo and thermal hydraulics solver, the temperature will be updated continuously. Thus, the cross sections must be prepared for all temperature points, or the code must be able to generate the cross section for desired temperature point on-the-fly. To store the cross section for one temperature point would cost ~1GB, and there will be more than a thousand materials having different temperature. To prepare and save cross section library into storage system is doable, but it is impossible to use it for the simulation since the ram memory of Linux cluster is limited. The remaining option is to have the capability to generate the cross section on-the-fly. Due to this reason, on-the-fly Doppler broadening techniques for resolved resonance range have been studied actively, and there are mature techniques that can be used practically. MCS employs Windowed MultiPole (WMP) method [52] since this method shows good efficiency comparing other techniques. Unlikely resolved resonance range, there is no on-the-fly broadening method for unresolved resonance range and thermal energy range yet that can be used for simulation practically. Thus, MCS employs interpolation technique for the unresolved resonance probability-table data and thermal scattering data.

4.3.1.   Multipole Representation

The multipole representation technique for the Doppler broadening at resolved resonance energy range was proposed by Hwang [53]. The multipole method generates the exact Doppler broadened cross sections by using resonance poles and residues which must be converted from the resonance parameters provided in ENDF. This method was not practically used because of the difficulty on resonance data conversion and low efficiency of method. Forget et al. proposed the WMP [52]. They have increased the efficiency by reducing the number of resonances to generate the cross section at target energy point based on the fact that resonance cross section is smooth if energy is far from the peak. Forget have shared windowed multipole code OpenW and the multipole library for 71 nuclides. The WMP module is implemented into MCS, and we have started the research to expand the multipole library. Currently, the multipole library is ready for 308 nuclides.

To confirm accuracy of Doppler broadened cross section by WMP module implemented in MCS, the cross sections generated by WMP is compared against cross sections in ACE file generated by NJOY. Figure IV-9 shows the total, absorption, and fission cross sections generated by WMP module and NJOY with the error criteria of 0.1%. Figure IV-10 shows the relative error of cross sections. The errors are smaller than 0.1% which is the error criteria used in NJOY.
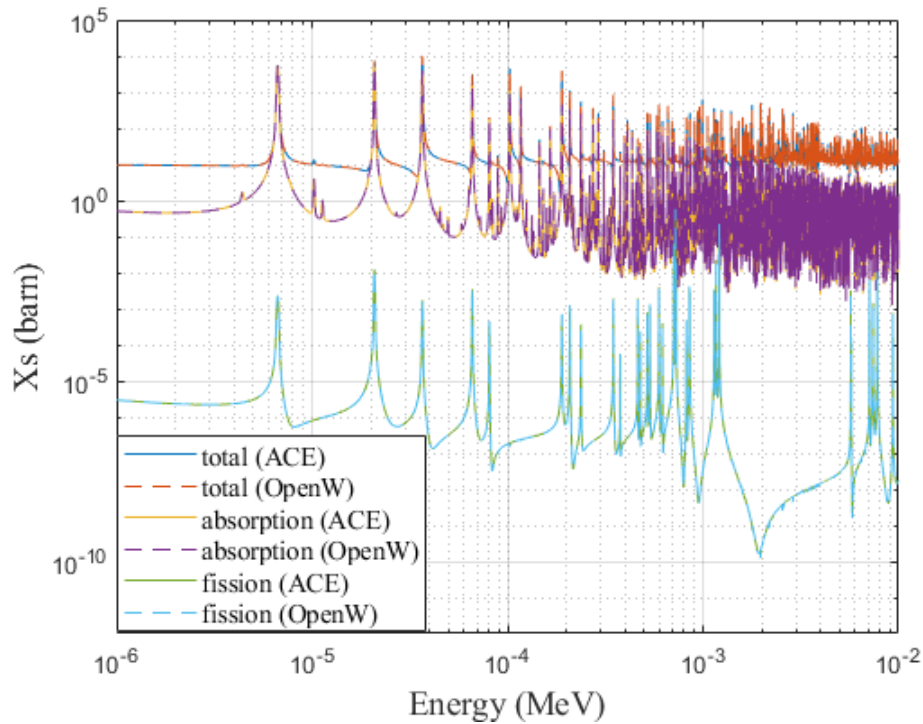
Figure IV-9: U-238 cross sections at 600K by OpenW.

The performance of WMP is tested against BEAVRS benchmark core problem. Four simulations are performed with different temperature and cross sections data: 293.K with ACE, 293.K with WMP, 600K with ACE, and 600K with WMP. Table IV-4 shows the multiplication factor. It should be noted that there are total 70 nuclides in BEAVRS core at beginning of cycle, and multipole library exist for 60 nuclides. MCS uses same ACE library for the nuclides not in the list of WMP library. The result with WMP module matches well with it of ACE.
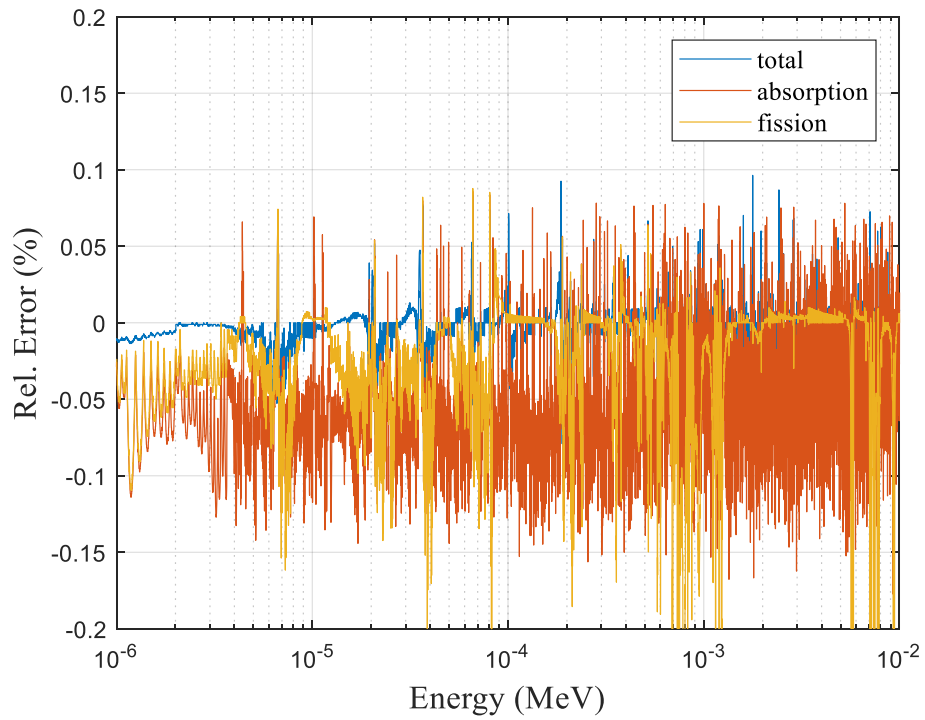
Figure IV-10: Comparison of U-238 cross sections by OpenW and NJOY.

Table IV-4: Verification of OpenW with BEAVRS Core.

Case		k_{eff}	SD
293.6K	OpenW	1.01862	0.00007
	ACE	1.01839	0.00007
600K	OpenW	0.99743	0.00007
	ACE	0.99724	0.00007

4.3.2.   Interpolation

The interpolation function is implemented for all energy range. When interpolation is used, MCS reads two pre-generated data set at lower and higher temperature than target temperature. In the resolved energy range, MCS uses sqrt-linear scheme as following:

$$f = \frac{\sqrt{T_{high}} - \sqrt{T}}{\sqrt{T_{high}} - \sqrt{T_{low}}} \quad , \qquad\qquad\qquad (IV.5)$$

$$\sigma(T) = f \cdot \sigma(T_{low}) + (1 - f) \cdot \sigma(T_{high}) \quad , \qquad\qquad (IV.6)$$

where σ is the cross section.
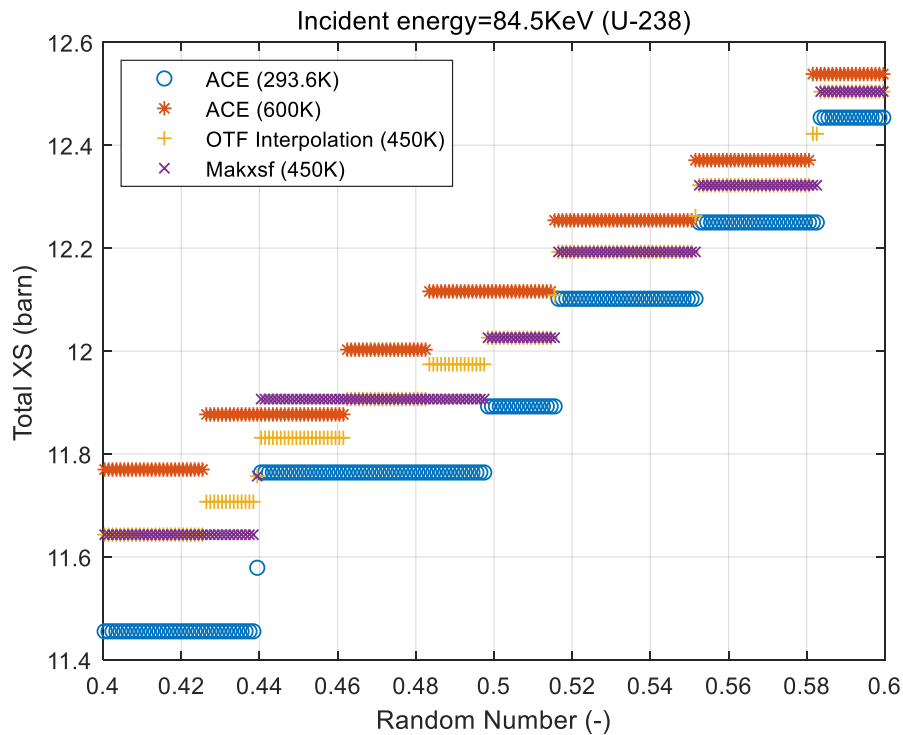
Figure IV-11: Ptable comparison of ^{238}U at 84.5KeV.

In the unresolved energy range, probability table of cross sections are given. The probability table so called ptable is a function of energy and random number [0,1). Typically, there are 20 cross sections at one energy point and cross section will be selected with the random number. Figure IV-11 show the example ptable of ^{238}U for incident neutron energy of 84.5KeV. In the figure, interpolated cross sections of 450K by *makxsf* and interpolation routine of MCS are given with the 293.K and 600K data. The cross section ladder in ptable can be different depending on the temperature, and *makxsf* choose the ladder at

75

lower temperature data. On the other hands, MCS does not need to follow one ladder. Since MCS samples cross section from both of ladder and interpolate it as shown in the Figure IV-12. It should be noted that the same random number must be used to sample cross section.

Algorithm On-the-fly interpolation of ptable
$f = (\ln(T_{high}) - \ln(T))/(\ln(T_{high}) - \ln(T_{low}))$ seed0 = get_random_seed XS_{low} = get_xs (D_{low}) change_seed(seed0) XS_{high} = get_xs (D_{high}) $XS = f\ XS_{low} + (1-f)XS_{high}$

Figure IV-12: Algorithm for on-the-fly interpolation of ptable.

For the thermal scattering, the outgoing neutron energy and angle is temperature dependent, and they are provided with distribution. It means that outgoing information must be sampled with random number. MCS uses linear-linear interpolation scheme for cross sections and outgoing neutron angle, and it uses special reciprocal equation for outgoing energy since the outgoing energy is reversely proportional to the temperature as Eqs. (IV.7) and (IV.8). Figure IV-13 shows the algorithm for on-the-fly interpolation of thermal data.

$$f = \frac{T_{high} - T}{T_{high} - T_{low}} \quad , \tag{IV.7}$$

$$E_{out} = \left(\frac{f}{E_{low}} - \frac{1-f}{E_{high}} \right)^{-1} \quad . \tag{IV.8}$$

Algorithm On-the-fly interpolation collision kernel

$f = (T_{high} - T)/(T_{high} - T_{low})$
 seed0 = get_random_seed
 $[E_{low},\ uvw_{low}]$ = collision_kernel (D_{low})
 change_seed(seed0)
 $[E_{high},\ uvw_{high}]$ = collision kernel (D_{high})
 E_{out} = 1/(f/E_{low} + (1-f)/E_{high})
 if   (GetRN() < f)
      $uvw_{out} = uvw_{low}$
 else
     $uvw_{out} = uvw_{high}$
 end if

Figure IV-13: Algorithm of on-the-fly interpolation of thermal scattering kernel.

The accuracy of on-the-fly interpolation for thermal scattering data is tested with VERA benchmark 1C problem. The VERA-1C benchmark is a typical pressurized water reactor pin cell with 3.1% enriched uranium fuel. The fuel temperature is 900K and the coolant temperature is 600K. Three

simulations were performed with same cross section data but thermal scattering data of ^{1}H. It should be noted that the true reference is the NJOY. However, the on-the-fly interpolation should be agreed with it of *makxsf* since they use same interpolation scheme.

- NJOY: 600K thermal scattering data processed by NJOY
- Mkaxsf: 600K data interpolated using 550K and 650K by *makxsf*
- OTF: on-the-fly interpolation using 550K and 650K data

Table IV-5 and Figure IV-14 show the multiplication factor and flux spectrum error in coolant region. The on-the-fly result matches well with *makxsf* as it should be.
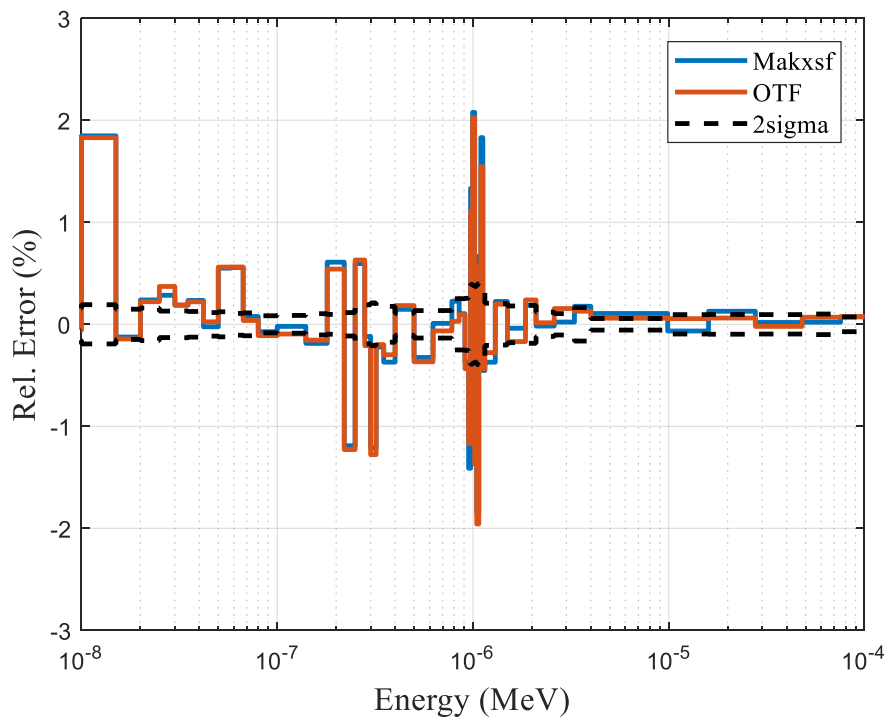
Figure IV-14: Flux spectrum comparison of VERA-1C problem in coolant region.

Table IV-5: Multiplication Factor of VERA-1C by On-The-Fly Interpolation.

Case	k_{eff}	SD	Diff. (pcm)	Time
NJOY	1.17402	0.00012	-	1.00
Makxsf	1.17414	0.00011	12	0.99
OTF	1.17402	0.00013	0	1.01

4.4. Thermal hydraulics Coupling

The closed channel thermal hydraulics solver called TH1D [54] is implemented. TH1D solver is original developed and used in nTRACER code developed at Seoul National University. TH1D solver solves thermal hydraulics equation based on the pin geometry. Figure IV-15 shows the algorithm of thermal hydraulics feedback. The feedback strategy is bit different from the conventional way and will be discussed in the section 4.4.2. MCS sends the power distribution in single pin tallied during the cycle, and TH1D calculates and sends the fuel temperature, cladding temperature, water temperature and water density. Since TH1D solves the pin geometry this procedure is repeated N times which is number of pins in problem.
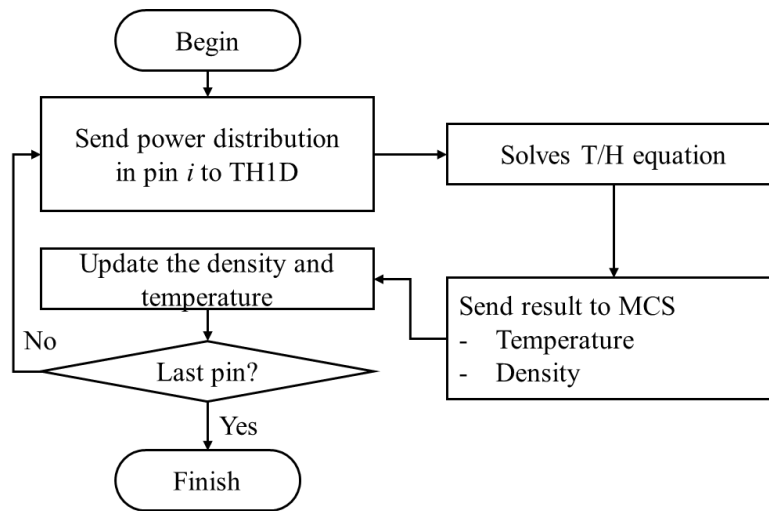
Figure IV-15: Program flow of MCS/TH1D.

TH1D solve two one-dimensional equational radially and axially as shown in the Figure IV-16. At first, it solves steady state mass and energy conservation equations axially to calculate the coolant temperature and density for each node as expressed in following equations:

$$\frac{\partial \rho v}{\partial z} = 0 \quad , \tag{IV.9}$$

$$\frac{\partial \rho h v}{\partial z} = q_c + \frac{\zeta}{A_c} q_w \equiv q \quad , \tag{IV.10}$$

where ρ is density (kg/m³) of coolant, h is the enthalpy (J/kg) of coolant, v is speed (m/s) of coolant, ζ is heated perimeter (m), A_c is cross section of the channel (m²), q_c is heat source (w/m³) in coolant, and q_w is heat flux of the fuel (w/m²). The steam table is implemented as a polynomial, and the parameters for steam table are fitted in the temperature range of 280°C to 340°C at 15.5 MPa. The radial temperature

distribution is calculated as shown in Eq. (II.11) with the temperature of coolant as a boundary condition.

$$\frac{1}{r}\frac{\partial}{\partial r}\left(k(T)r\frac{\partial T}{\partial r}\right)+q=0 \quad , \tag{IV.11}$$

where $k(T)$ is conductivity of fuel as a function of temperature.
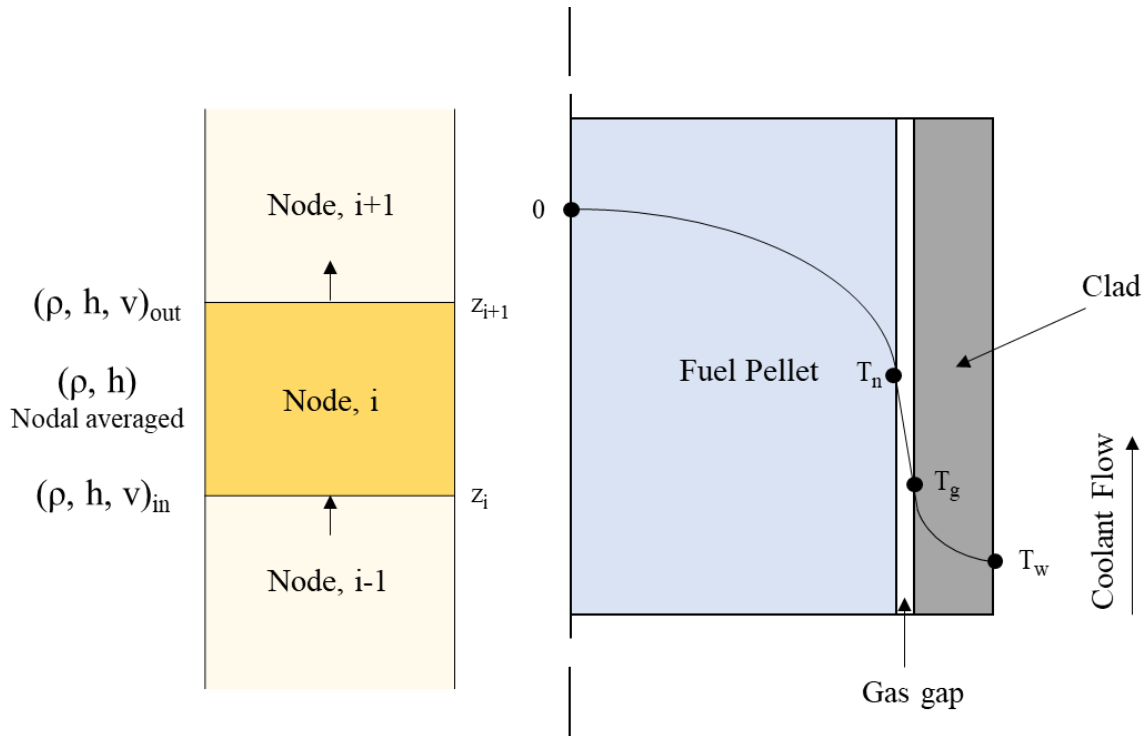
Figure IV-16: Single channel TH1D solver axial (left) and radial (right) diagram.

4.4.1. Mapping

The array to saves the power distribution in MCS is long one-dimensional array size of total number of fuel meshes which is calculated by (# of radial meshes in fuel) × (# of axial meshes in fuel) × (# of fuel pins in problem). Since TH1D is closed channel thermal hydraulics code, there is no need to give core geometry information or pin location to TH1D. What MCS need to do only is to send the power distribution of one pin repeatedly. Figure IV-17 shows the index of pin in MCS. The example geometry has 2 radial meshes and 3 axial nodes. MCS increases the index from the inner region of fuel to outer region at bottom mesh. After counting meshes at bottom mesh, it moves to the second axial mesh from bottom. If we look at global index as shown in Figure IV-18, the index from 1 to 6 is for first pin, and next 6 indices are for second pin. Receiving data from TH1D can be done in same way.
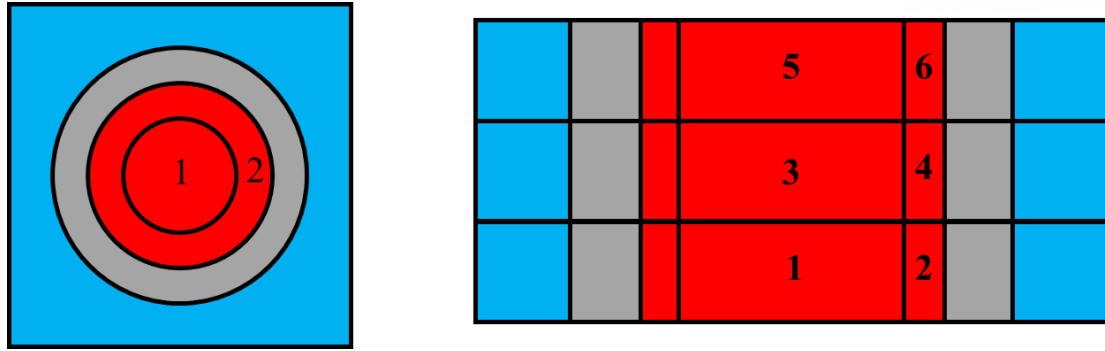
Figure IV-17: Pin index of MCS for TH feedback.

Figure IV-18: Global index of MCS for TH feedback.

4.4.2. Feedback Strategy

There have been many researches on coupling work of neutronics code and thermal hydraulics code system. Most of the coupling work adopts the Picard iteration which is serial coupling method using two individual single-physics solver. In the framework of Picard iteration, neutronics code and thermal hydraulics solver are independent but they exchange the variables which is input parameter for each code. Figure IV-19 presents the conventional coupling flow of neutronics code and thermal hydraulics code using Picard iteration. The temperature will be converged within 5 iterations generally. The program flow of Picard iteration is described below.

1. Performs the transport calculation (shown in Eq. (IV.12)).
2. Sends power distribution to thermal hydraulics solver.
3. Solves thermal hydraulics equation with given power distribution from transport solver shown in Eq. (IV.13)).
4. Check the convergence of fuel temperature by comparing the temperature of current iteration i and the temperature of previous iteration $i-1$.

80

5. If temperature is not converged, updates the thermal hydraulics condition including fuel temperature, coolant temperature and coolant density.

6. Repeat step 1-4 until the temperature is converged.
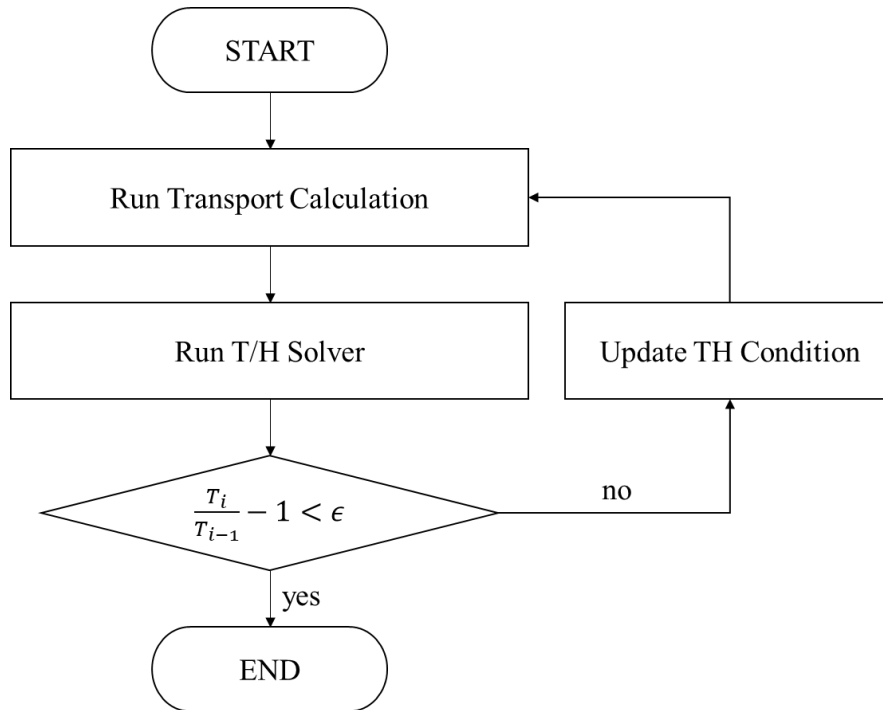
Figure IV-19: Conventional coupling flow.

$$P_i = P(T_i) + \varepsilon_i^P \quad , \tag{IV.12}$$

$$T_{i+1} = T(P_i) = T_0 + \varepsilon_i^T \quad , \tag{IV.13}$$

where ε_i^P is the uncertainty of power, ε_i^T is the uncertainty of thermal hydraulics condition, and T_0 is true solution of thermal hydraulics.

When performing the coupling of Monte Carlo code and thermal hydraulics code, the statistical uncertainty must be taken account when deciding the convergence criteria. If the convergence criterion is set to way below than statistical uncertainty, it will never be converged. Therefore, if we want to have the neutronics solution with the fuel temperature criterion of 1K, it may require tremendous neutron histories. In application of large-scale problem, the it may not possible to have converged solution with small convergence criterion practically. This mean that the we may have to use large convergence criterion. In addition to this convergence issue, the computing time to get the converged temperature distribution for 4-5 iterations is the problem since this our final solution is just a result of 1 iteration. It

means that the efficiency with thermal hydraulics coupling will be 20% at maximum comparing the stand alone neutronics simulation.

For the reasons discussed above, MCS performs thermal hydraulics feedback at the end of every transport cycle instead of doing iterations to have converged thermal hydraulics solution. By doing that, the computing time of coupled simulation would be comparable with the simulation without thermal hydraulics feedback unlikely conventional approach since MCS approach does not requires additional iterations but inactive cycles which is required in any cases for the fission source converge. Table IV-6. shows the comparison of conventional approach and MCS approach.

Table IV-6: Comparison of Conventional T/H Feedback Approach and MCS Approach.

	Conventional Approach	MCS Approach
Thermal/hydraulic feedback	Every Transport Simulation (after all neutronics cycles)	Every cycle
Statistical Uncertainty of T/H condition	σ	$\sigma \times \sqrt{\text{number of cycles}}$
Coupled Solution	$P\left(T_0 + \varepsilon_i^T\right) + \varepsilon_i^P$	$E\left(P\left(T_0 + \varepsilon_i^T\right) + \varepsilon_i^P\right)$
Computing Time	4-5 (Depending on # of iterations)	1

4.4.3.   VERA HFP Assembly

In this section, the coupling simulation of MCS and TH1D is tested against VERA benchmark problem #6 which is assembly benchmark at HFP state. The problem #6 assembly is composed of 264 fuel pins of 3.1% enriched uranium fuel and 25 guide tubes as shown in Figure IV-20. Table IV-7 shows the specification of problem #6.

Table IV-7: VERA Benchmark Problem #6 Specification.

Input	Value
Fuel Density	10.257g/cm^3
Fuel Enrichment	3.1%
Inlet Coolant Temperature	565K
Reactor Pressure	2250psia
Boron Concentration	1300ppm
Rated Power (100%)	17.67MW
Rated Coolant Mass Flow	85.9683kg/s
Gap conductance	5678.3
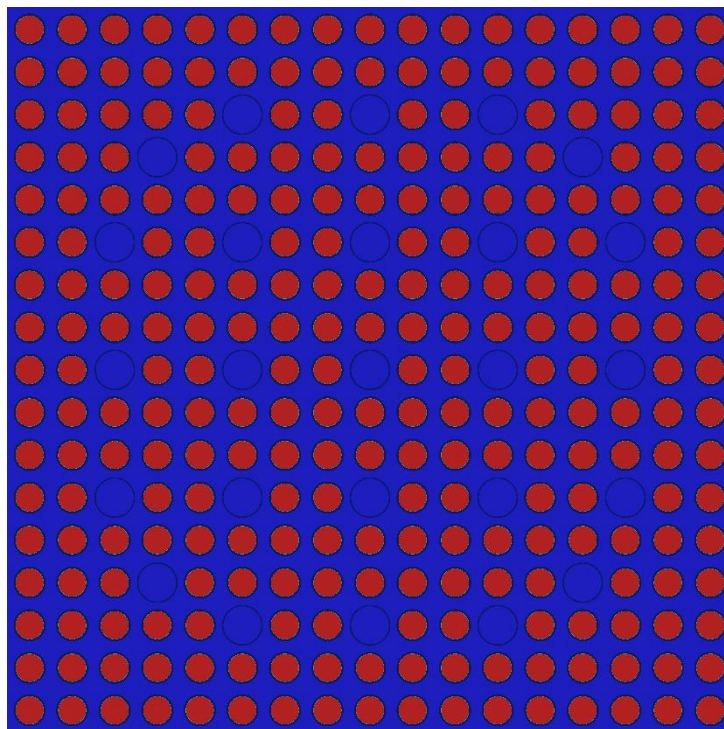
Figure IV-20: Configuration of VERA HFP assembly.

83

The reference results are taken from the journal paper of Aviles [57] and technical report of CASL project [58]. In those documents, the solution of MC21 Monte Carlo code [59] and COBRA-IE subchannel thermal hydraulics code and the solution of CASL's VERA-CS code system, MPACT/COBRA-TF [58][60] can be found. MCS simulation was performed with same mesh definitions as used for MC21/COBRA-IE and VERA-CS which is 1 radial mesh and 49 axial meshes in 365.76 cm active core region. It should be mentioned that there are two thing that might lead the disagreement of MCS solution and others. First, MCS uses single channel T/H solver while reference results were produced with subchannel code. Second, all of three neutronics codes employs different version of neutron data and different way to treat temperature dependent cross sections as follows

- MCS: ENDF-VII1 data is used. Cross sections are treated by On-The-Fly Broadening module for 47 nuclides, and 8 nuclides are treated by interpolation module with 50 – 100 K interval.
- MC21: ENDF-VII.1 data is used. Cross sections are interpolated with 50K interval in fuel region and 10K interval in coolant region.
- MPACT: 47 group cross section library based on ENDF/B-VII.0 data is used

MCS simulation was performed with 300 multicycles, 5 inactive cycles, 20 active cycles, and 20,000 histories per cycle. The flow rate per one pin is calculated by dividing number of fuel pins to the total flow rate per assembly. Figure IV-21 shows the three-dimensional distribution of power, fuel temperature, coolant temperature, and coolant density. As it should be, power distribution and fuel temperature show similar trends. The coolant temperature increases from bottom to top since coolant flows from bottom to top. Figure IV-22 shows the axial distribution of fuel and coolant temperatures. Four results were compared with MC21/COBRA-IE and VERA-CS: effective multiplication factor, radial fission reaction rate distribution, radial fuel temperature distribution, exit coolant temperature distribution. The multiplication factors are presented in Table IV-8. All of three codes matches well within hundred pcm. The axially averaged radial distribution of fission reaction rate and fuel temperature are compared in Figure IV-23 and Figure IV-24. Both results are matches well against two references in RMS of 0.1% fission error and 6-8K of fuel temperature. Exist coolant temperature also matches well with RMS error of 1K.

Table IV-8: Effective Multiplication Factor for VERA Problem 6.

Code System	*k-effective*	SD	Difference (pcm)
MC21/COBRA-IE	1.16424	0.00003	Reference
VERA-CS	1.16361	-	-63
MCS	1.16444	0.00009	20

84
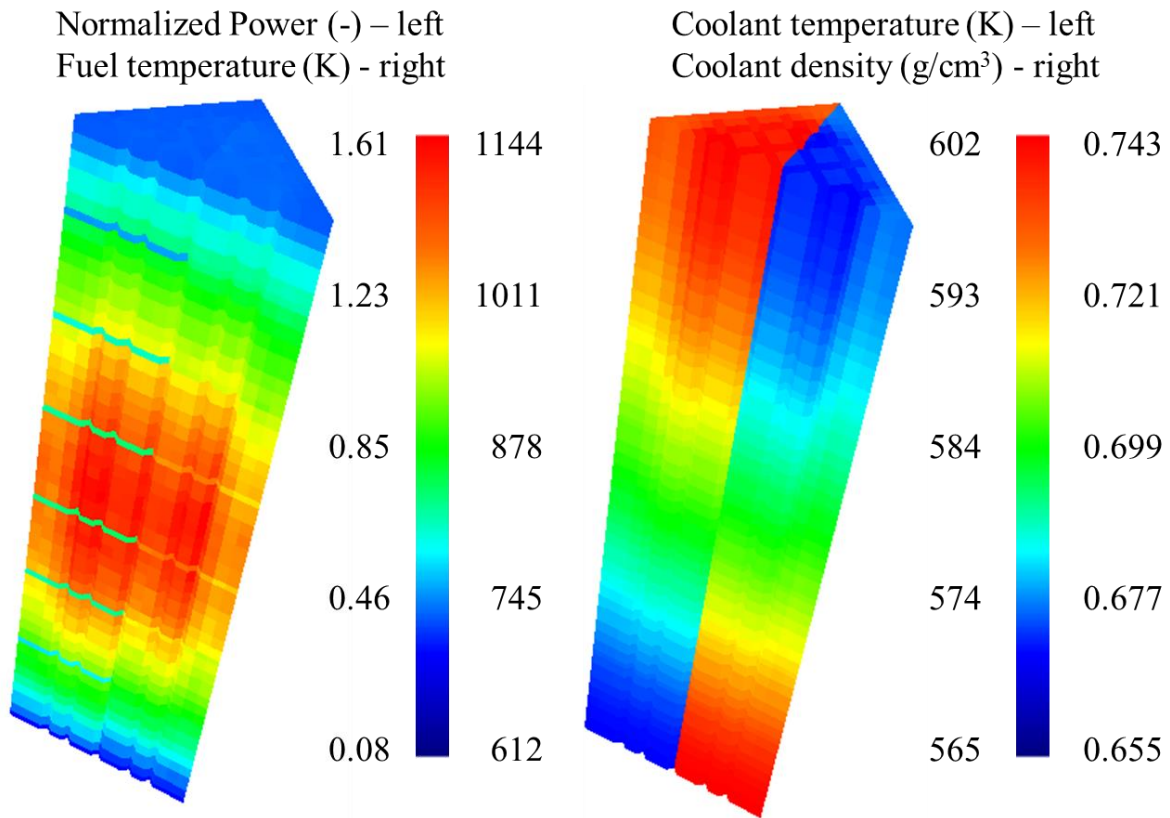
Figure IV-21: Distributions of power, fuel temperature, coolant temperature, and coolant density for VERA problem 6.
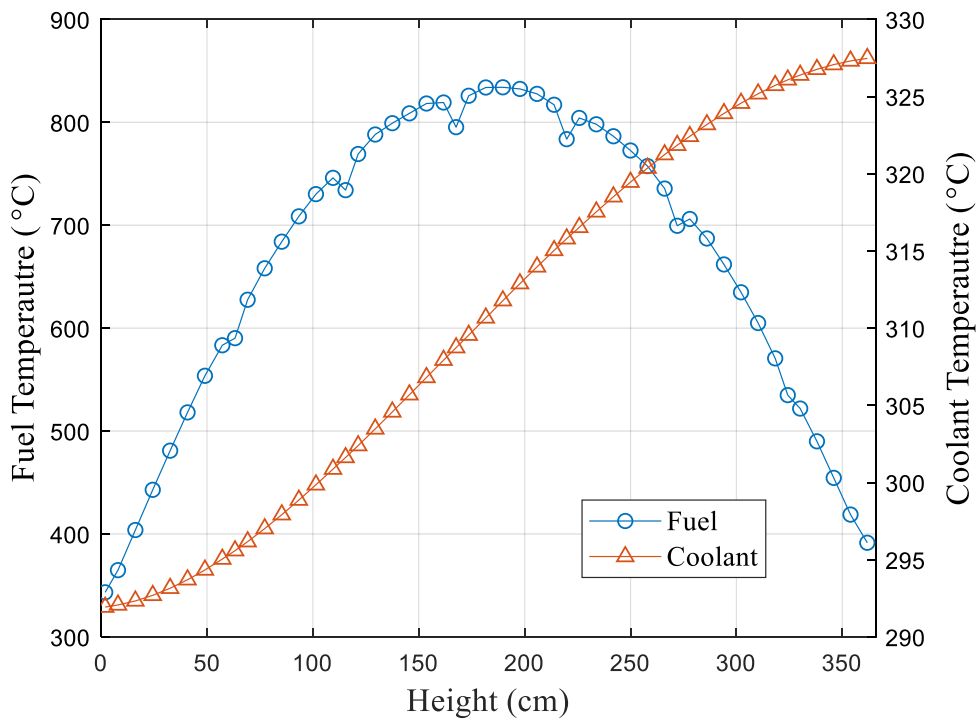
Figure IV-22: Axial distribution of fuel and coolant temperatures for VERA problem 6.

VERA / MCS / Rel. Diff (%)

Rel. Diff (%)	
Max	-0.282
RMS	0.115

Col1	Col2	Col3	Col4	Col5	Col6	Col7	Col8	Col9
1.035 / 1.036 / *0.018*	1.010 / 1.010 / *0.059*							
1.036 / 1.035 / *-0.101*	1.011 / 1.010 / *-0.063*	1.011 / 1.011 / *0.019*						
	1.037 / 1.036 / *-0.046*	1.037 / 1.037 / *-0.036*						
1.034 / 1.034 / *-0.079*	1.009 / 1.009 / *0.072*	1.011 / 1.012 / *0.058*	1.044 / 1.044 / *0.003*	1.034 / 1.031 / *-0.248*				
1.031 / 1.031 / *-0.010*	1.006 / 1.005 / *-0.116*	1.010 / 1.009 / *-0.048*	1.044 / 1.044 / *0.031*	1.052 / 1.049 / *-0.219*				
	1.025 / 1.025 / *0.051*	1.027 / 1.027 / *0.013*		1.037 / 1.035 / *-0.162*	1.017 / 1.016 / *-0.077*	0.974 / 0.973 / *-0.086*		
1.011 / 1.012 / *0.052*	0.989 / 0.988 / *-0.075*	0.989 / 0.988 / *-0.144*	1.012 / 1.011 / *-0.081*	0.983 / 0.984 / *0.016*	0.964 / 0.965 / *0.121*	0.949 / 0.949 / *-0.008*	0.940 / 0.938 / *-0.224*	
0.976 / 0.977 / *0.070*	0.973 / 0.973 / *0.033*	0.972 / 0.972 / *-0.007*	0.974 / 0.974 / *0.036*	0.965 / 0.965 / *-0.045*	0.956 / 0.955 / *-0.070*	0.947 / 0.945 / *-0.201*	0.943 / 0.940 / *-0.282*	0.949 / 0.946 / *-0.275*

MC21/COBRA-IE / MCS / Rel. Diff (%)

Rel. Diff (%)	
Min	-0.201
Max	0.079
RMS	0.105

Col1	Col2	Col3	Col4	Col5	Col6	Col7	Col8	Col9
1.037 / 1.036 / *-0.175*	1.010 / 1.010 / *0.079*							
1.037 / 1.035 / *-0.197*	1.010 / 1.010 / *0.045*	1.010 / 1.011 / *0.048*						
	1.037 / 1.036 / *-0.104*	1.039 / 1.037 / *-0.190*						
1.036 / 1.034 / *-0.185*	1.009 / 1.009 / *0.062*	1.011 / 1.012 / *0.078*	1.045 / 1.044 / *-0.102*	1.032 / 1.031 / *-0.084*				
1.032 / 1.031 / *-0.098*	1.006 / 1.005 / *-0.086*	1.009 / 1.009 / *0.051*	1.045 / 1.044 / *-0.122*	1.051 / 1.049 / *-0.181*				
	1.026 / 1.025 / *-0.105*	1.028 / 1.027 / *-0.074*		1.036 / 1.035 / *-0.124*	1.017 / 1.016 / *-0.096*	0.973 / 0.973 / *-0.055*		
1.012 / 1.012 / *-0.037*	0.988 / 0.988 / *-0.004*	0.988 / 0.988 / *-0.022*	1.012 / 1.011 / *-0.081*	0.983 / 0.984 / *0.056*	0.965 / 0.965 / *0.017*	0.948 / 0.949 / *0.055*	0.939 / 0.938 / *-0.096*	
0.977 / 0.977 / *-0.001*	0.973 / 0.973 / *0.023*	0.972 / 0.972 / *0.034*	0.974 / 0.974 / *0.026*	0.965 / 0.965 / *0.028*	0.955 / 0.955 / *-0.049*	0.946 / 0.945 / *-0.149*	0.942 / 0.940 / *-0.198*	0.948 / 0.946 / *-0.201*

Figure IV-23: Radial fission reaction rate comparison for VERA problem 6.

Left table — Fuel Temperature (C)

MC21/COBRA-IE (C) / MCS (C) / Diff. MCS-MC21 (C)								
Max Diff.	11.8	Min Diff.	2.4	RMS Diff.	8.5			

-	848.3	848.4	-	847.4	845.4	-	832.4	810.0
-	852.3	855.6	-	858.4	853.6	-	841.3	820.7
-	4.0	7.2	-	11.0	8.2	-	8.9	10.7
848.3	832.3	832.6	848.6	831.8	829.8	841.5	818.8	807.9
857.9	838.8	841.6	859.4	841.4	838.6	853.3	828.5	816.7
9.6	6.5	9.0	10.8	9.6	8.8	11.8	9.7	8.8
848.4	832.6	832.9	849.3	833.2	831.9	842.4	818.8	807.6
854.1	841.1	841.5	859.4	841.0	840.8	853.3	825.1	817.8
5.7	8.5	8.6	10.1	7.8	8.9	10.9	6.3	10.2
-	848.6	849.3	-	853.6	853.6	-	832.5	808.5
-	856.0	860.8	-	861.8	862.3	-	841.3	816.1
-	7.4	11.5	-	8.2	8.7	-	8.8	7.6
847.4	831.8	833.2	853.6	846.8	857.8	848.2	815.7	803.1
857.2	839.9	840.6	863.5	854.6	866.2	855.7	820.6	807.8
9.8	8.1	7.4	9.9	7.8	8.4	7.5	4.9	4.7
845.4	829.8	831.9	853.6	857.8	-	836.1	803.9	797.2
854.9	836.5	839.1	860.2	866.3	-	846.1	809.5	804.8
9.5	6.7	7.2	6.6	8.5	-	10.0	5.6	7.6
-	841.5	842.4	-	848.2	836.1	809.5	793.8	791.6
-	849.0	852.4	-	857.5	845.4	816.6	801.4	799.9
-	7.5	10.0	-	9.3	9.3	7.1	7.6	8.3
832.4	818.8	818.8	832.5	815.7	803.9	793.8	788.2	789.0
842.8	828.2	826.6	840.7	818.1	808.9	801.6	795.6	798.1
10.4	9.4	7.8	8.2	2.4	5.0	7.8	7.4	9.1
810.0	807.9	807.5	808.5	803.1	797.2	791.6	789.0	791.6
820.0	815.2	815.8	816.2	811.2	804.9	799.7	798.2	798.8
-	-	-	-	-	-	-	-	-

Right table — Fuel Temperature (C)

MC21/COBRA-IE (C) / MCS (C) / Diff. MCS-MC21 (C)								
Max Diff.	9.6	Min Diff.	1.2	RMS Diff.	6.6			

-	851.1	851.2	-	850.0	847.9	-	834.2	811.7
-	852.3	855.6	-	858.4	853.6	-	841.3	820.7
-	1.2	4.4	-	8.4	5.7	-	7.1	9.0
851.4	834.4	834.2	851.3	833.4	831.4	843.7	819.4	809.2
857.9	838.8	841.6	859.4	841.4	838.6	853.3	828.5	816.7
6.5	4.4	7.4	8.1	8.0	7.2	9.6	9.1	7.5
851.2	834.6	834.9	852.3	835.2	833.3	844.6	820.2	808.7
854.1	841.1	841.5	859.4	841.0	840.8	853.3	825.1	817.8
2.9	6.5	6.6	7.1	5.8	7.5	8.7	4.9	9.1
-	851.6	852.5	-	855.9	856.3	-	834.5	810.7
-	856.0	860.8	-	861.8	862.3	-	841.3	816.1
-	4.4	8.3	-	5.9	6.0	-	6.8	5.4
850.1	834.0	835.1	856.5	848.1	860.1	850.2	816.9	804.5
857.2	839.9	840.6	863.5	854.6	866.2	855.7	820.6	807.8
7.1	5.9	5.5	7.0	6.5	6.1	5.5	3.7	3.3
848.4	831.6	833.5	856.7	859.9	-	838.1	805.6	798.5
854.9	836.5	839.1	860.2	866.3	-	846.1	809.5	804.8
6.5	4.9	5.6	3.5	6.4	-	8.0	3.9	6.3
-	844.3	845.6	-	850.3	837.8	810.3	794.8	792.5
-	849.0	852.4	-	857.5	845.4	816.6	801.4	799.9
-	4.7	6.8	-	7.2	7.6	6.3	6.6	7.4
835.0	819.6	820.1	834.5	816.9	805.5	795.1	788.9	789.8
842.8	828.2	826.6	840.7	818.1	808.9	801.6	795.6	798.1
7.8	8.6	6.5	6.2	1.2	3.4	6.5	6.7	8.3
811.5	809.3	809.2	810.6	804.7	798.5	792.6	790.1	791.9
820.0	815.2	815.8	816.2	811.2	804.9	799.7	798.2	798.8
8.5	5.9	6.6	5.6	6.5	6.4	7.1	8.1	6.9

Figure IV-24: Radial fuel temperature comparison for VERA problem 6.

Left table

Exit Coolant Temperature (K)	MC21/COBRA-IE (C) MCS (C) Diff. MCS-MC21 (C)		Max Diff.	3.9
			Min Diff.	-0.7
			RMS Diff.	1.3

327.2	328.2	327.2	327.2	328.1	326.9	326.5	326.7	325.0
-	328.6	328.6	-	328.5	328.5	-	327.8	326.8
-	0.4	1.4	-	0.4	1.6	-	1.1	1.8
328.2	328.5	328.2	328.2	328.4	328.0	327.5	326.9	325.0
328.6	327.8	327.8	328.6	327.8	327.7	328.3	327.1	326.7
0.4	-0.7	-0.4	0.4	-0.6	-0.3	0.8	0.2	1.7
327.2	328.2	327.2	327.3	328.3	327.1	326.5	326.7	325.0
328.6	327.8	327.8	328.7	327.9	327.8	328.3	327.1	326.6
1.4	-0.4	0.6	1.4	-0.4	0.7	1.8	0.4	1.6
327.2	328.2	327.3	327.4	328.3	327.0	326.4	326.6	324.8
-	328.6	328.7	-	328.9	328.9	-	327.8	326.7
-	0.4	1.4	-	0.6	1.9	-	1.2	1.9
328.1	328.4	328.3	328.3	327.4	326.7	327.2	326.5	324.6
328.6	327.8	327.8	328.9	328.4	329.0	328.6	327.0	326.4
0.5	-0.6	-0.5	0.6	1.0	2.3	1.4	0.5	1.8
326.9	328.0	327.1	327.0	326.7	326.4	326.9	326.2	324.3
328.5	327.7	327.8	328.9	329.0	-	328.0	326.4	326.1
1.6	-0.3	0.7	1.9	2.3	-	1.1	0.2	1.8
326.5	327.5	326.5	326.4	327.2	326.9	326.6	325.8	324.0
-	328.3	328.3	-	328.5	328.0	326.7	325.9	325.8
-	0.8	1.8	-	1.3	1.1	0.1	0.1	1.8
326.7	326.9	326.7	326.6	326.5	326.2	325.8	325.1	323.4
327.8	327.1	327.1	327.8	327.0	326.4	325.9	325.5	325.6
1.1	0.2	0.4	1.2	0.5	0.2	0.1	0.4	2.2
325.0	325.0	325.0	324.8	324.6	324.3	324.0	323.4	321.9
326.8	326.6	326.6	326.7	326.4	326.1	325.8	325.6	325.8
1.8	1.6	1.6	1.9	1.8	1.8	1.8	2.2	3.9

Right table

Exit Coolant Temperature (K)	MC21/COBRA-IE (C) MCS (C) Diff. MCS-MC21 (C)		Max Diff.	4.7
			Min Diff.	-1.6
			RMS Diff.	1.5

326.7	329.4	326.8	326.8	329.2	326.6	326.3	327.8	324.7
-	328.6	328.6	-	328.5	328.5	-	327.8	326.8
-	-0.8	1.8	-	-0.7	1.8	-	0.0	2.1
329.4	329.2	329.3	329.4	329.2	329.1	328.7	327.8	324.7
328.6	327.8	327.8	328.6	327.8	327.7	328.3	327.1	326.7
-0.8	-1.4	-1.5	-0.8	-1.4	-1.4	-0.4	-0.7	2.0
326.8	329.3	326.9	327.0	329.4	326.9	326.4	327.7	324.8
328.6	327.8	327.8	328.7	327.9	327.8	328.3	327.1	326.6
1.8	-1.5	0.9	1.7	-1.5	0.9	1.9	-0.6	1.8
326.8	329.4	327.0	327.2	329.8	327.1	326.5	327.6	324.7
-	328.6	328.7	-	328.9	328.9	-	327.8	326.7
-	-0.8	1.7	-	-0.9	1.8	-	0.2	2.0
329.2	329.2	329.4	329.8	327.3	326.9	328.3	327.4	324.4
328.6	327.8	327.8	328.9	328.4	329.0	328.6	327.0	326.4
-0.6	-1.4	-1.6	-0.9	1.1	2.1	0.3	-0.4	2.0
326.6	329.1	326.9	327.1	326.9	326.3	327.8	327.0	324.1
328.5	327.7	327.8	328.9	329.0	-	328.0	326.4	326.1
1.9	-1.4	0.9	1.8	2.1	-	0.2	-0.6	2.0
326.3	328.7	326.4	326.5	328.3	327.8	327.3	326.6	323.8
-	328.3	328.3	-	328.5	328.0	326.7	325.9	325.8
-	-0.4	1.9	-	0.2	0.2	-0.6	-0.7	2.0
327.8	327.8	327.7	327.6	327.4	327.0	326.6	326.1	323.4
327.8	327.1	327.1	327.8	327.0	326.4	325.9	325.5	325.6
0.0	-0.7	-0.6	0.2	-0.4	-0.6	-0.7	-0.6	2.2
324.7	324.7	324.8	324.7	324.4	324.1	323.8	323.4	321.1
326.8	326.6	326.6	326.7	326.4	326.1	325.8	325.6	325.8
2.1	1.9	1.8	2.0	2.0	2.0	2.0	2.2	4.7

Figure IV-25: Exit coolant temperature comparison for VERA problem 6.

4.5. Critical Boron Concentration

The critical boron search is implemented in simple way. MCS updates the boron concentration for cycle $i+1$ at the end of every transport cycle based on the *k-effective* tallied at cycle i as followings:

$$C_{B,i+1} = (k_i - 1) \times C + C_{B,i} \quad,$$

(IV.14)

where C is the is the conversion constant from multiplication factor to boron concentration. Constant C is set to 10^4 based on the assumption that reactivity of boron 1 ppm is equal to the 10 pcm reactivity. This boron concentration update algorithm is tested against BEAVRS benchmark. Benchmark provides the critical boron concentration with 5 rod positions. The simulations were performed with following conditions:

- Geometry: BEAVRS whole core
- Library: ENDF-VII.1
- Inactive cycle: 4
- Active cycle: 30
- Subcycle: 200
- Histories per cycle: 50,000

Table IV-9 shows the estimated critical boron concentration and measured data for five rod positions. It shows that the estimated critical boron concentration matches well against measured data in the range of -5 – 15 ppm. Figure IV-26 shows the critical boron concentration at every cycle including inactive and active in all rod out position. It should be noted that the concentration is converged after 2-3 cycles and the fluctuation is small.

Table IV-9: Estimated Critical Boron Concentration for BEAVRS Benchmark HZP.

Bank position	Measured	MCS	SD	Difference
All out	975	970.34	0.61	-4.66
D in	902	909.82	0.54	7.82
C,D, in	810	818.59	0.57	8.59
A,B,C,D in	686	689.28	0.48	3.28
All in	508	523.69	0.67	15.69
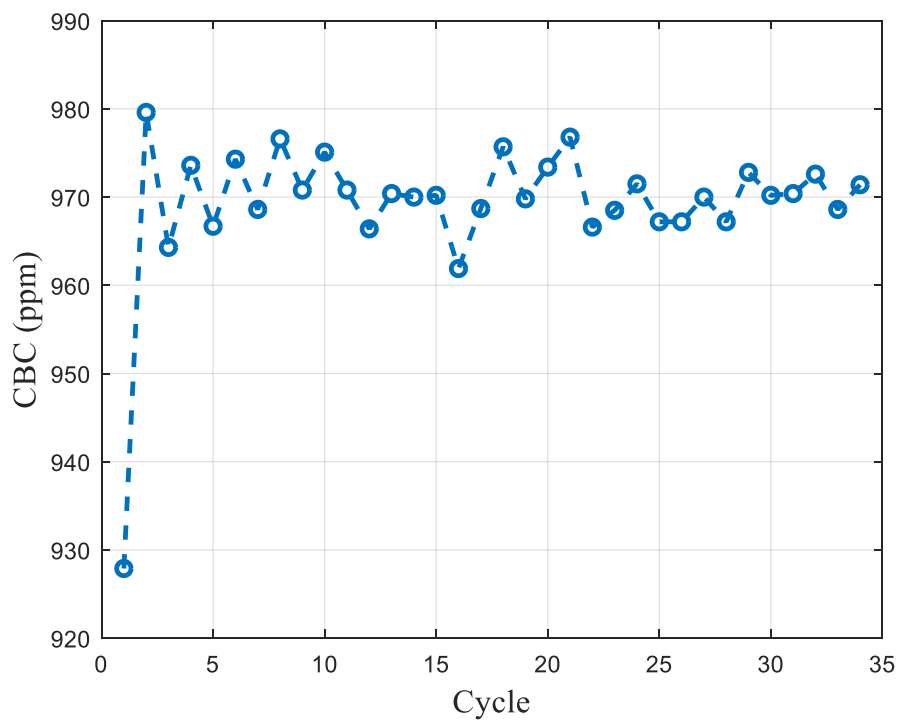
Figure IV-26: Critical boron concentration at every cycle (ARO position).

V. Power Reactor Simulation

5.1. Introduction

In this section, the capability of MCS to carry out power reactor simulation is demonstrated on the BEAVRS benchmark [29]. BEAVRS benchmark is Westinghouse type PWR producing 3,411 MWt. The core is composed of 193 fuel assemblies having 264 fuel pins each. The benchmark provides very detail information about Cycle 1 and Cycle 2 simulation including power history, inlet temperature, rod position, detector signals, loading pattern.

The plan for this section is as follows. The sensitivity test is performed in section 5.2 to decide calculation condition including burnup step, mesh structure, and history. Next, the variance overestimation phenomena induced by feedbacks will be discussed in section 5.3. Finally, the BEAVRS Cycle 1 and 2 simulations are performed and compared against measured data and two step code STREAM/RAST-K (ST/RK) developed at UNIST [61].

5.2.   Sensitivity Study on BEAVRS Cycle 1

To meet the criteria of Kord Smith challenges [4] in the development of high-fidelity Light Water Reactor (LWR) core neutronics tools, the core behavior should be analyzed down to the level of individual fuel pellet. This requires a lot of fuel meshes approximately 220 million zones (193 assemblies×289 pins/assembly×400 pellets/pin×10 depletion rings/pellet). This will require tones of memory about 4 TB which is much larger than maximum memory on computer memory at this moment. In addition to this memory issue, the Monte Carlo simulation will take forever to reach the 95/95 statistical criteria on Linux cluster. Therefore, we have no choice but to used coarse mesh structure to finish the simulation with limited computing power and memory. In addition to the mesh structure, depletion step also should be decided.

5.2.1.   Burnup Step Sensitivity

For the reactor design with two step code system, 15 burnup steps are used in general. Two simulations are performed to confirm whether 15 burnup steps are enough or not for Monte Carlo simulation by comparing the reference solution produced with 23 burnup steps. The simulation conditions are as below:
- BEAVRS quarter core geometry
- ENDF-VII.1 library
- Feedbacks (thermal hydraulics, equilibrium xenon, critical boron concentration, on-the-fly Doppler broadening)
- Semi predictor corrector algorithm
- 4 inactive cycles, 20 active cycles, 300 subcycles, and 10,000 histories per subcycle
- 1 radial ring and 20 axial meshes per pin

Figure V-1 and Figure V-2 show the critical boron concentration and difference with 2 sigma standard deviation of 15 steps and 23 steps. Since the boron concentrations exist at different burnup points, the difference was calculated by interpolating data. As shown in the figure, the 15 steps and 23 steps match well within 2 sigma statistical uncertainty showing 15 steps are enough also for Monte Carlo simulation for BEAVRS core.
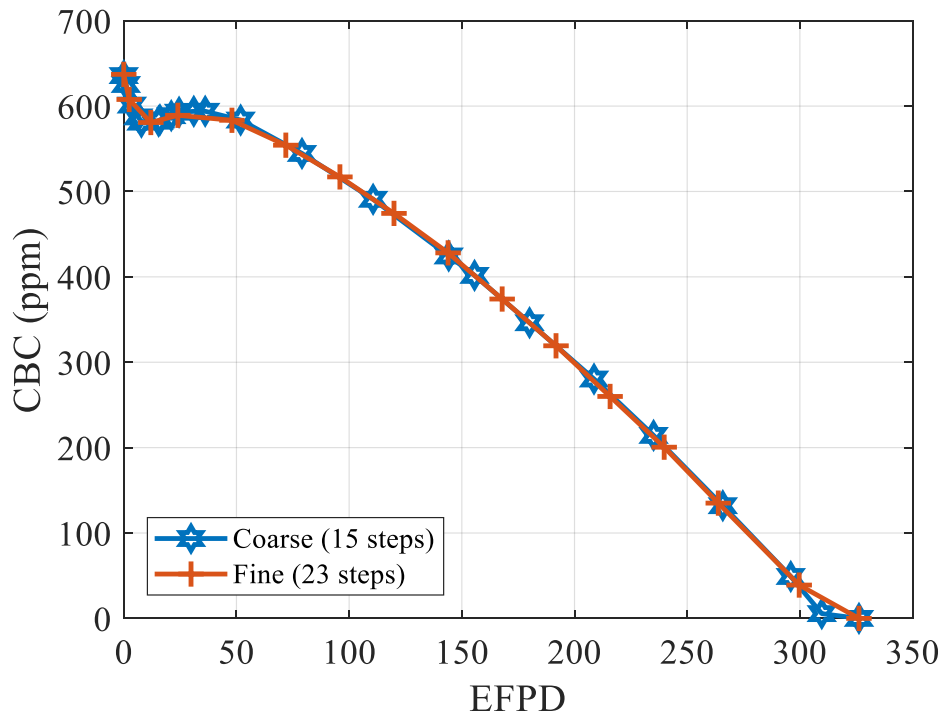
Figure V-1: Critical boron concentration for BEAVRS Cycle 1 with fine and coarse burnup step.
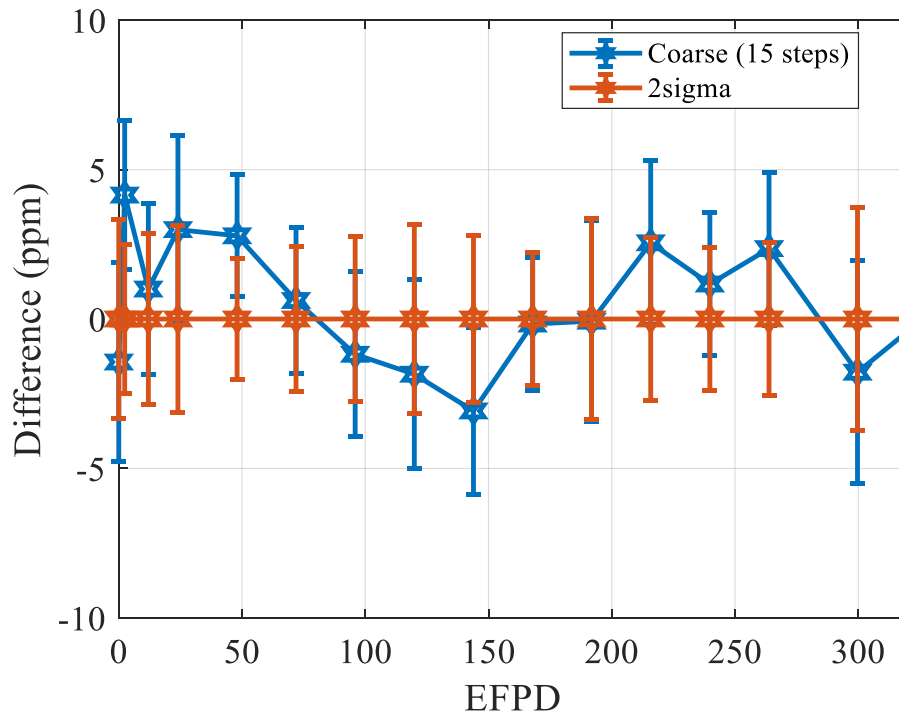
Figure V-2: Critical boron concentration difference for BEAVRS Cycle 1 with fine and coarse burnup step.

5.2.2. History Sensitivity

The solution of MCS multiphysics simulation can be expressed as follows:

$$E\left(P\left(T_0 + \varepsilon_i^T\right) + \varepsilon_i^{\prime\prime}\right) \quad .$$

(V.1)

The concern is the uncertainty propagation of thermal hydraulics condition, ε_i^T, to neutronics solution. If infinite number of histories are used, the statistical uncertainty of power will be zero and the thermal hydraulics condition also have no uncertainty propagated from neutronics solution. However, it is inevitable to have neutronics uncertainty. Thus, it is important to estimate the effect of uncertainty of thermal hydraulics condition to the Monte Carlo multiphysics solution. Two simulations are performed by employing different number of histories per cycle. It should be mentioned that the thermal hydraulics uncertainty would be proportional to the uncertainty of power which is inversely proportional to the $\sqrt{N}$.

Two simulations were performed by employing two set of history:
- Case 1: 4 inactive cycles, 20 active cycles, 300 subcycles, and 10,000 histories per subcycle
- Case 2: 4 inactive cycles, 20 active cycles, 300 subcycles, and 100,000 histories per subcycle
-
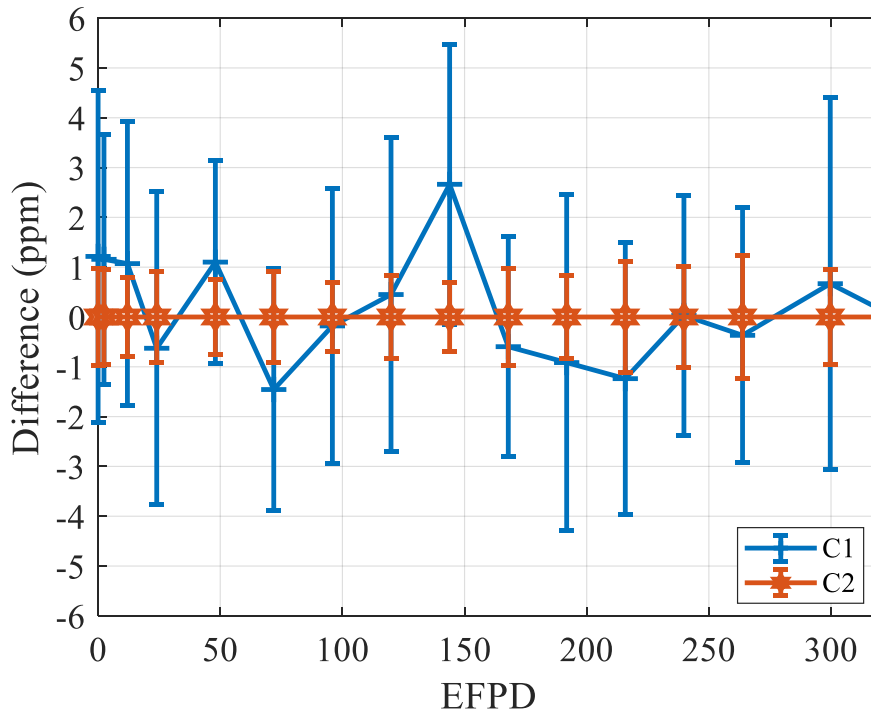
Figure V-3: Critical boron concentration difference for BEAVRS Cycle 1 with two set of history.

94
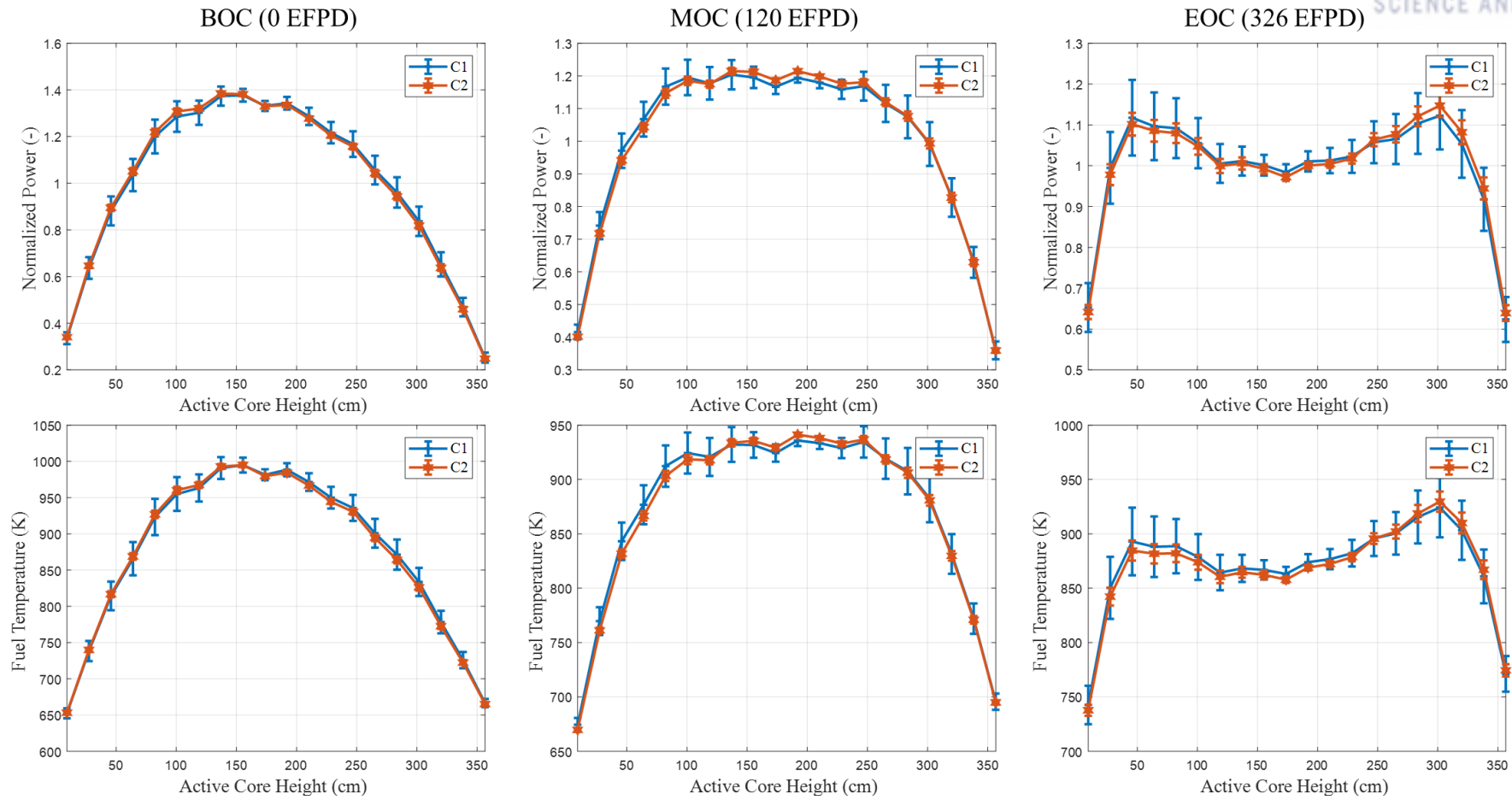
Figure V-4: Radially integrated axial distribution of power and fuel temperature at BOC, MOC, and EOC with two set of history.

Figure V-3 shows the critical boron concentration difference with 2sigma for case 1 and 2. As shown in the figure, case 1 and 2 matches well within standard deviation. Figure V-4 shows the radially integrated axial distribution of power and fuel temperature at BOC, MOC, and EOC. As presented in the figure, axial distribution also matches well within standard deviation. Those figures show that uncertainty of thermal hydraulics condition does not affect much to the neutronics solution. Thus, the solution of case 1 is reliable. Figure V-5 and Figure V-6 show the probability density of fuel and coolant temperature standard deviation. It should be noted that the standard deviation used to plot those figures are not the estimated standard deviation of all cycles but one cycle. In each figure, there are six lines of case 1 and case 2 at BOC, MOC, and EOC state. Since case 2 employs 10 times more histories, the standard deviation of case 2 is smaller than case 1. The median standard deviations are compared to see the uncertainty convergence behavior whether it follows $1/\sqrt{N}$ or not. Table V-1 shows the median standard deviation of fuel and coolant temperature of case 1, 2, and ratio of two. The ratios of three states are about 3.3 which is similar to the ideal ratio $\sqrt{10}$.

Table V-1: Median Standard Deviation of Fuel and Coolant Temperature.

State	Median of Fuel Temperature			Median of Coolant Temperature		
	C1	C2	C1/C2	C1	C2	C1/C2
BOC	71.48	20.95	3.41	1.68	0.47	3.61
MOC	69.89	21.13	3.31	1.60	0.46	3.49
EOC	75.40	23.98	3.14	1.98	0.63	3.16
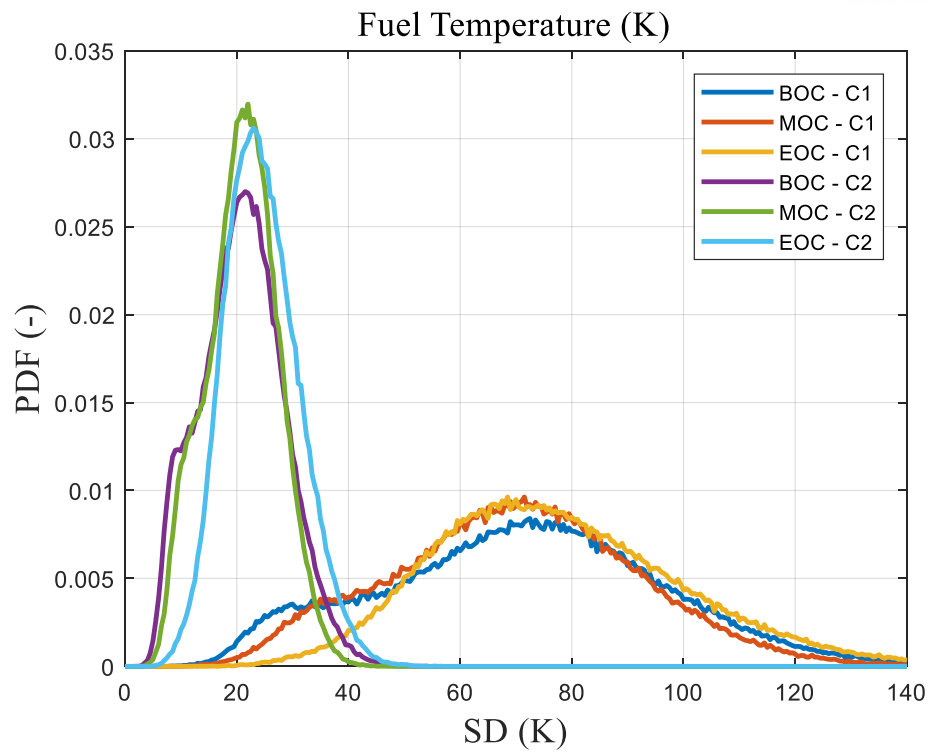
Figure V-5: Probability density of fuel temperature uncertainty for BEAVRS Cycle 1 BOC and EOC.
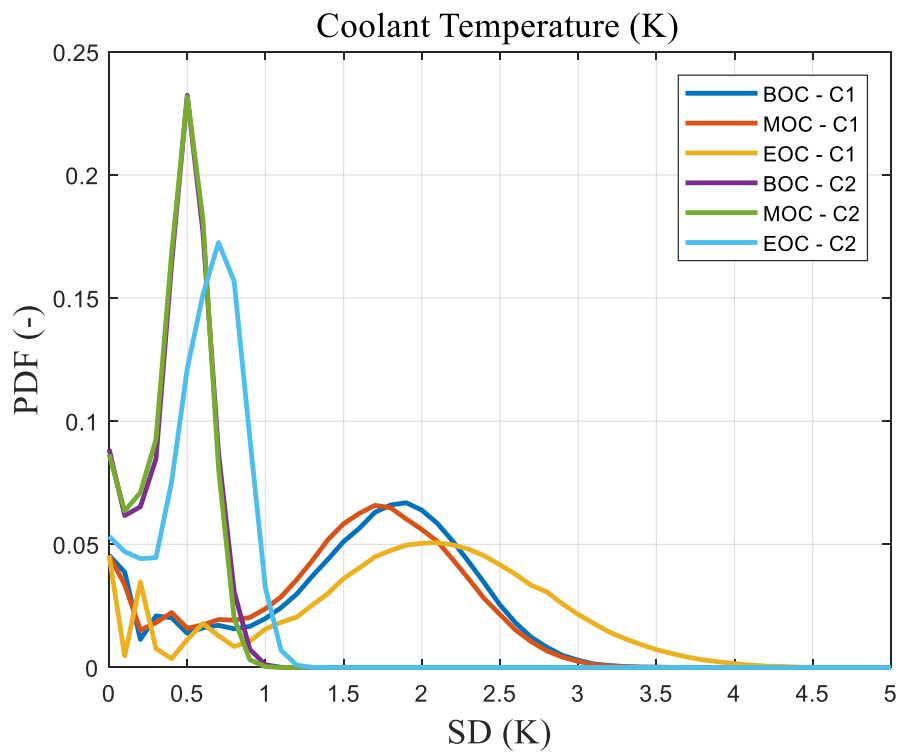
Figure V-6: Probability density of coolant temperature uncertainty for BEAVRS Cycle 1 BOC and EOC.

5.2.3.   Mesh Structure Sensitivity

The fuel pin must be divided into radially and axially to give distribution of temperature and number density. The mesh sensitivity was performed with various number of axial meshes from 1 to 30. It should be noted that the pin geometry is modeled explicitly including spacer grid as shown in Figure V-7. The fuel, clad, and coolant regions are divided axially from bottom of active fuel region to top of active fuel region. There are 12,828 number of fuel pins in the geometry. Thus, the total number of fuel meshes are 12,828 × (number of axial meshes). The number of cladding and coolant meshes are same as fuel meshes.
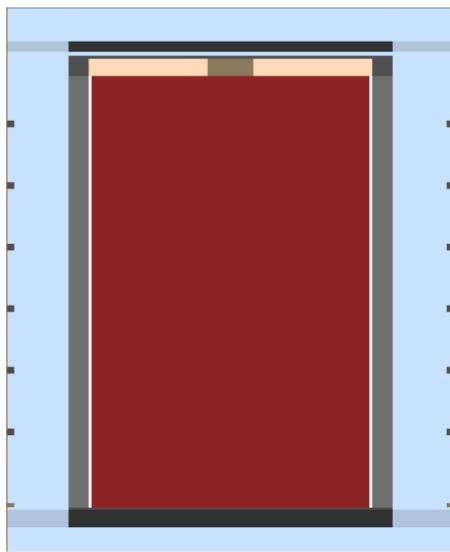
Figure V-7: Configuration of fuel pin in yz plane.

The simulations were performed at BOC with following conditions

- 4 inactive cycles, 30 active cycles, 300 subcycles, and 20,000 histories per subcycle
- Thermal hydraulics feedback
- Equilibrium xenon feedback
- *N* axial mesh (*N*=1, 5, 10, 15, 20, 30). (equally divided)

The assembly-wise radial fission distribution with 1 mesh and 30 meshes are compared. In the Figure V-8, assembly-wise fission distribution, 2sigma, and relative difference are presented. The result of 1 mesh matches very well with the result of 30 meshes within 2sigma.

Figure V-8 table content:

									30 Mesh
									Rel. SD (%)
									Rel Diff. (%)

0.81	0.84	0.75	0.66				
2.83	2.55	2.28	2.00				
1.14	1.01	0.82	0.10				
0.77	0.89	0.75	0.89	0.95	0.73		
2.32	2.20	1.88	1.65	1.62	1.64		
0.69	1.13	0.53	0.53	0.76	0.84		
0.84	0.78	0.84	0.81	0.87	0.87	0.73	
1.76	1.66	1.35	1.09	1.17	1.34	1.51	
-0.29	-0.42	0.21	0.10	0.81	0.93	0.37	
0.82	0.91	0.81	0.89	1.08	0.87	0.95	
1.51	1.29	0.95	0.69	0.85	1.13	1.45	
-0.90	-0.52	-0.45	0.37	0.77	0.51	0.32	
0.94	0.84	0.93	0.84	0.89	0.81	0.89	0.66
1.44	1.35	1.06	0.76	0.87	1.10	1.46	1.72
-1.01	-0.88	-0.28	-0.09	0.44	0.22	0.30	-0.18
0.82	0.92	0.84	0.94	0.82	0.84	0.75	0.75
1.80	1.66	1.42	1.18	1.23	1.32	1.59	2.03
-1.95	-1.01	-0.74	-0.19	-0.21	0.08	0.16	0.07
0.83	0.80	0.93	0.84	0.92	0.79	0.90	0.85
2.04	1.89	1.85	1.67	1.62	1.63	1.99	2.32
-1.53	-1.73	-0.89	-0.73	-0.37	0.08	0.37	0.58
0.76	0.83	0.82	0.94	0.82	0.84	0.77	0.81
2.17	2.14	2.02	1.90	1.84	1.97	2.18	2.49
-1.72	-1.51	-1.47	-0.56	-0.39	0.21	0.26	0.50

R/A	
Max	1.14
Min	-1.95
RMS	1.84

Figure V-8: Radial fission distribution comparison with 30 mesh and 1 mesh.

The axial fission distribution in the core with various axial mesh are compared in Figure V-9. The axial distribution of all cases matches very well within 2sigma except the one with 1 axial mesh. According to the result what we have here, it would be okay to use 5 mesh for BOC simulation.

Figure V-9: Axial fission distribution with various number of mesh (1, 5, 10, 15, 20, 30).

The cycle simulations were performed with 10 axial meshes, 20 axial meshes, and 30 axial meshes:

- 4 inactive cycles, 30 active cycles, 300 subcycles, and 20,000 histories per subcycle
- Semi predictor corrector with 15 burnup steps

Figure V-10 shows the critical boron concentration difference from solution with 30 meshes. The result of 20 meshes and 30 shows good agreement while the difference of 10 meshes and 30 meshes increases as burnup progress. The result shows that the 20 axial meshes are required for the burnup simulation.
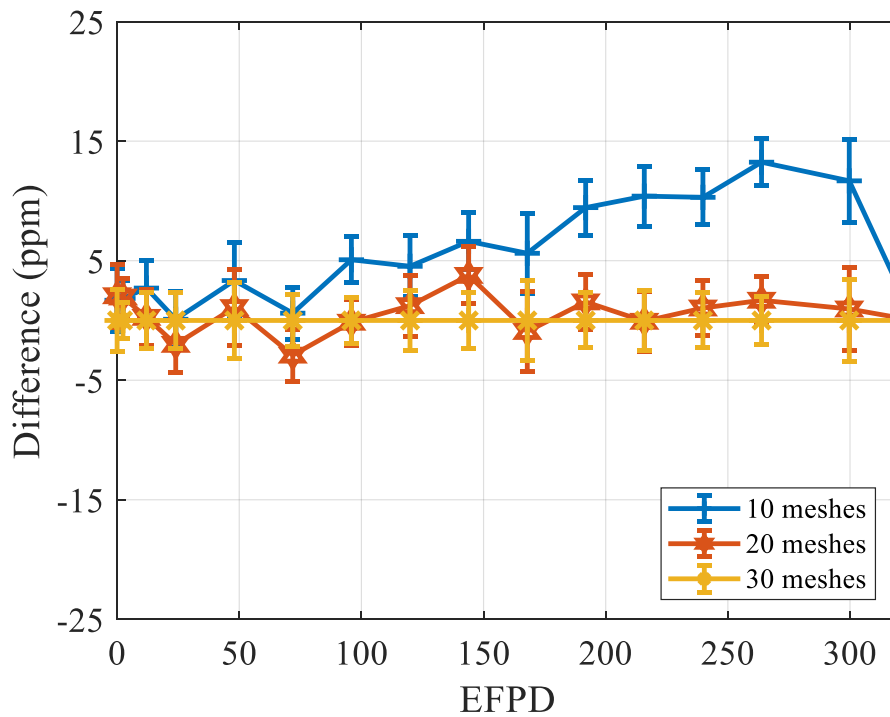
Figure V-10: Critical boron concentration difference of BEAVRS Cycle 1 with 10, 20, and 30 axial meshes.

5.2.4. Error Propagation

In Monte Carlo multiphysics simulation, the statistical error of reaction rates propagates as burnup progress. Eight simulations were performed with difference random seed:

- 4 inactive cycles, 30 active cycles, 300 subcycles, and 20,000 histories per subcycle
- Semi predictor corrector with 15 burnup steps
- 20 axial meshes

Figure V-11 shows the critical boron concentration difference and linear power distribution at BOC, MOC, and EOC for 8 simulations. All results match within 2sigma showing the effect of error propagation is not severe. The important observation in this figure is that the linear power results of 8 simulations are match well despite of large standard deviation. This would mean that the MCS overestimates the standard deviation, and this will be discussed in the next section.
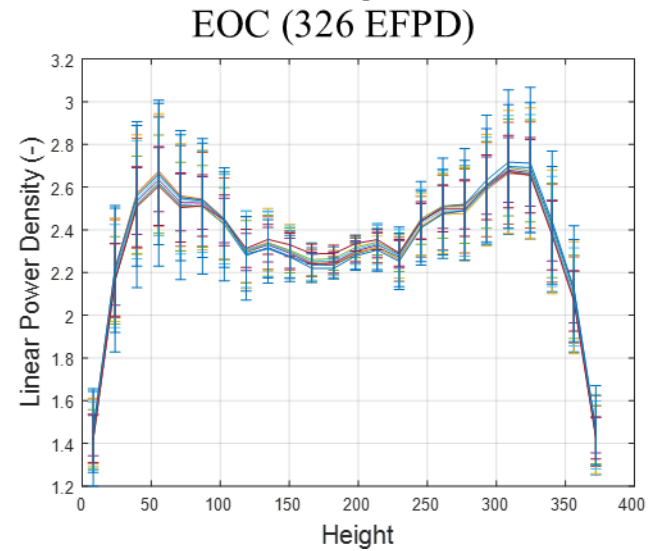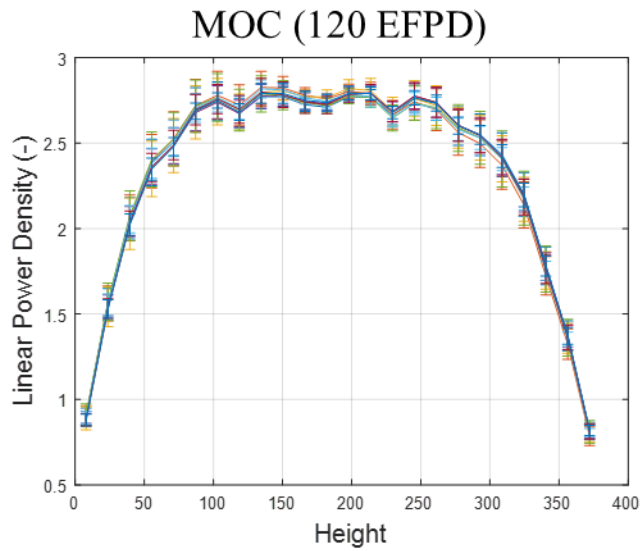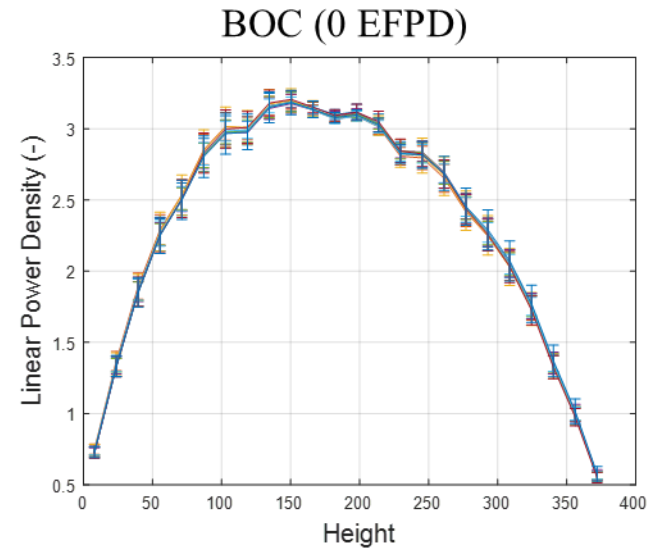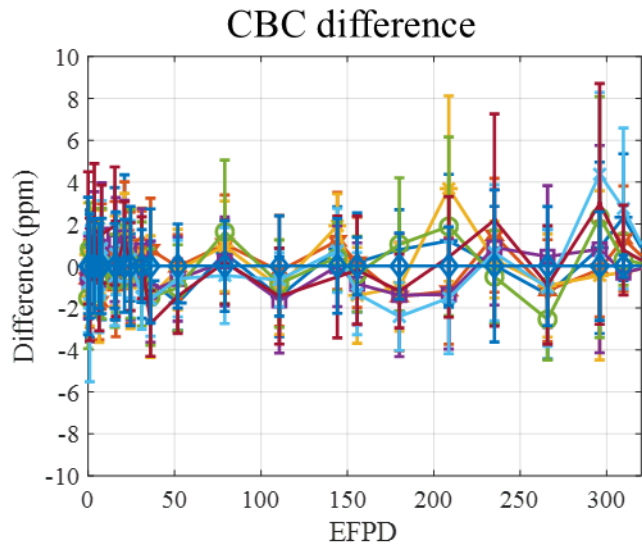
Figure V-11: Critical boron concentration difference and liner power density of BEAVRS Cycle 1 for 8 independent simulations.

5.3. Variance Overestimation in Tally

In order to see the variance bias, 28 independent simulations were performed at BOC and 18 independent simulation were performed at EOC. Five quantities are tallied in this section: critical boron concentration, axial shape index, axially integrated radial power (assembly-wise power), radially integrated axial power, and mesh-wise power distribution. The simulations were performed by employing following condition:

- 4 inactive cycles, 30 active cycles, 300 subcycles, and 20,000 histories per subcycle
- 20 axial meshes for feedbacks
- 24 axial meshes for radial power tally (equally divided)

The real and apparent standard deviation of five quantities are summarized in Table V-2. As summarized in the table, all parameters are overestimated at BOC and EOC. The relative standard deviation of mesh power is at 95% cumulative density point. It should be noted that the ASI and axial power show the biggest overestimation while critical boron concentration and radial power distribution show smaller overestimation ratio.

Table V-2: Real and Apparent Standard Deviation of Five Quantities.

	CBC (SD)	ASI (SD)	RP (RSD)	AP (RSD)	Mesh (RSD)
BOC (App.)	1.39	0.0144	0.5-1.5%	0.8-2.6%	8.23%
BOC (Real)	0.87	0.0061	0.4-1.1%	0.5-1.5%	8.15%
EOC (App.)	1.87	0.0616	0.4-1.6%	1.3-4.3%	7.3%
EOC(Real)	1.50	0.0086	0.4-1.0%	0.5-1.5%	6.5%

The overestimation of variance can be explained with the inter-cycle correlation induced by multiphysics feedback. In order to measure the autocorrelation coefficients, another simulation was performed with 6,000 active cycles. ACCs of mesh 1,7, 12, 19, 24 are presented in the Figure V-12. In case of equilibrium xenon feedback, high power at cycle i leads high xenon density at cycle $i+1$ which will lead lower power. Big negative autocorrelation coefficients at lag 1 can be explained with this negative effect of feedbacks. One more thing should be mentioned that the correlation of even lag is negative and odd lag is positive, and the correlation will not vanish. The overestimation of variance can be solved by adopting batch method. The variance with large T batch will converges to the real variance. Thus, the ratio of sample standard deviation, $R(T)$, with 1 batch and T batch as shown in Eq. (V.2) is estimated to check how many batches are required to have unbiased variance.

$$R(T) = \frac{\sigma_S^2\left[\overline{Q}_{L,T}\right]}{\sigma_S^2\left[\overline{Q}_{L,1}\right]} \quad . \tag{V.2}$$
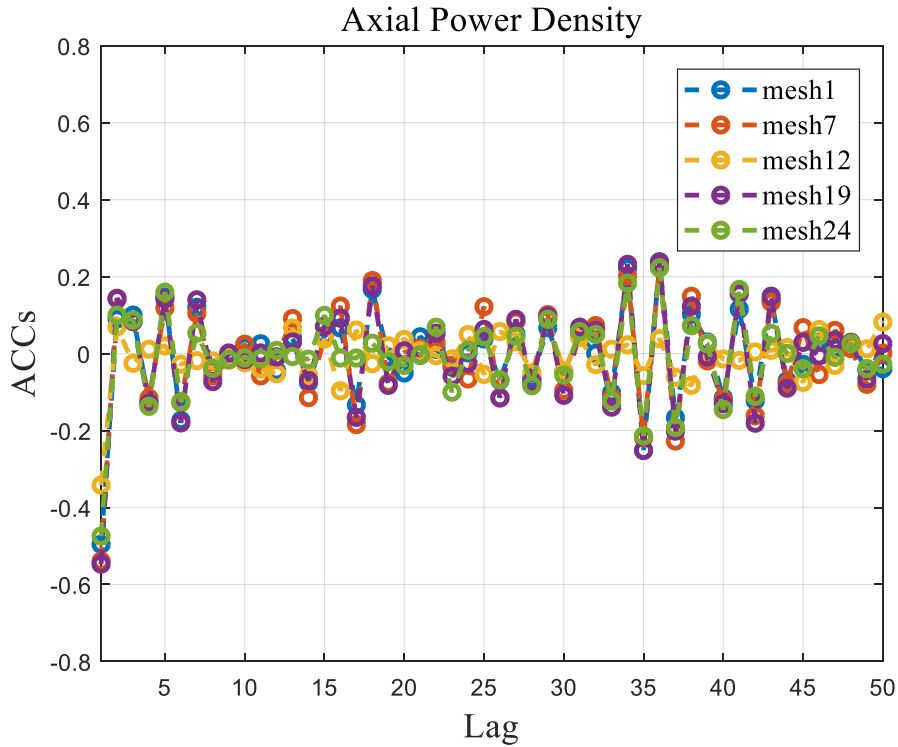
Figure V-12: Autocorrelation coefficients of axial power at BOC.

Figure V-13 shows the ratio $R(T)$ of first mesh at BOC, and it shows the ratio converges with 20 batch size. Same test is performed for EOC too. The autocorrelation coefficients are presented in Figure V-14. The correlation of cycles is bigger than BOC which can explains bigger overestimation. Due to larger correlation, number of batches required to estimates unbiased standard deviation increase to 60 as shown in Figure V-15.
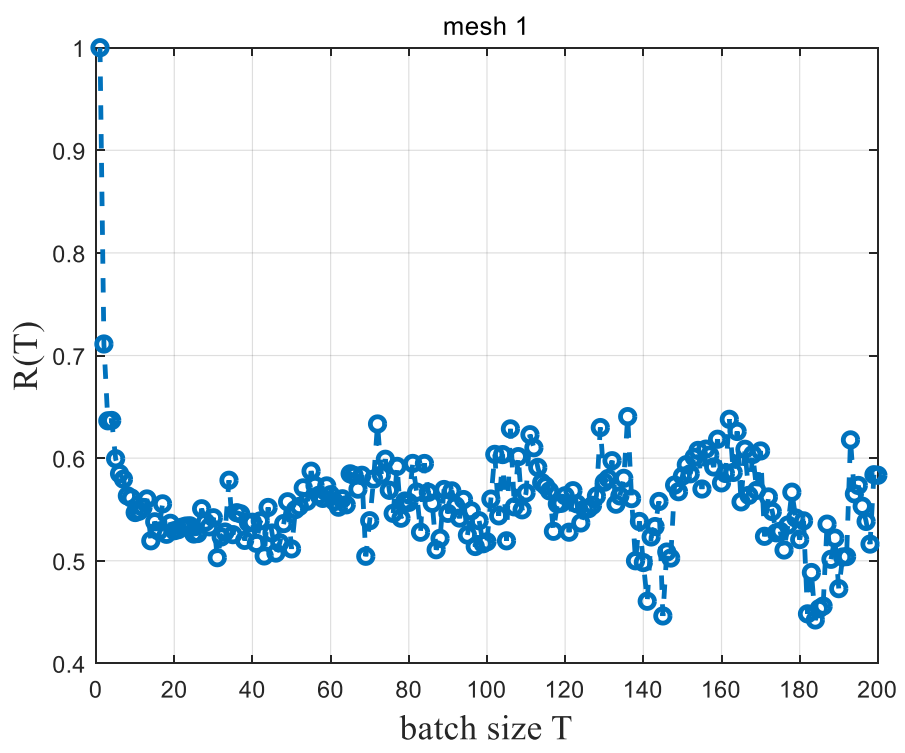
Figure V-13: Standard deviation of 1st mesh with different batch size at BOC.
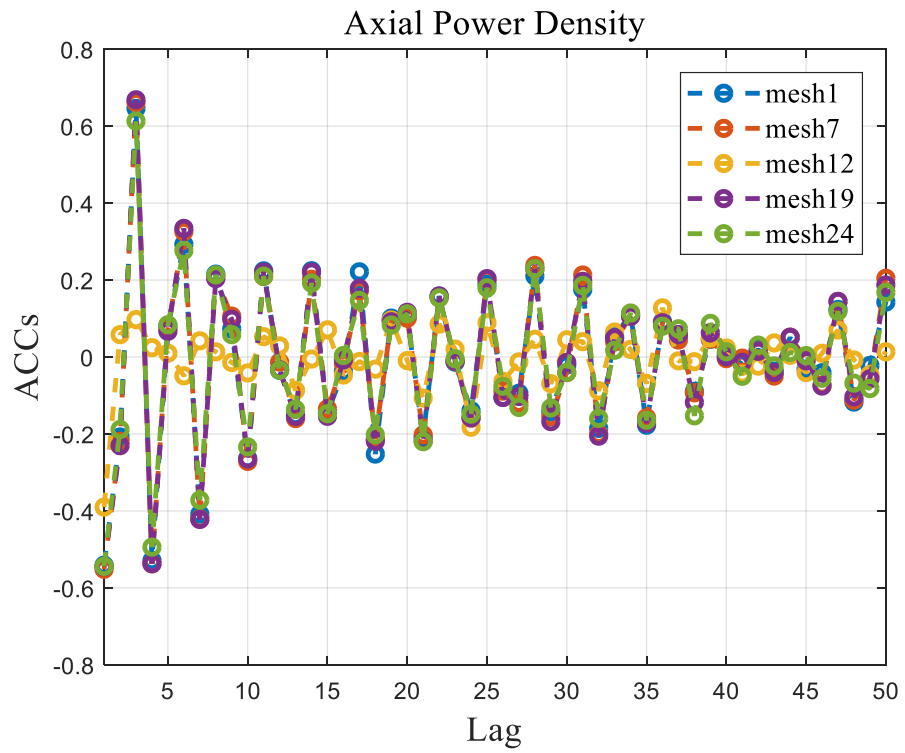
Figure V-14: Autocorrelation coefficients of axial power at EOC.
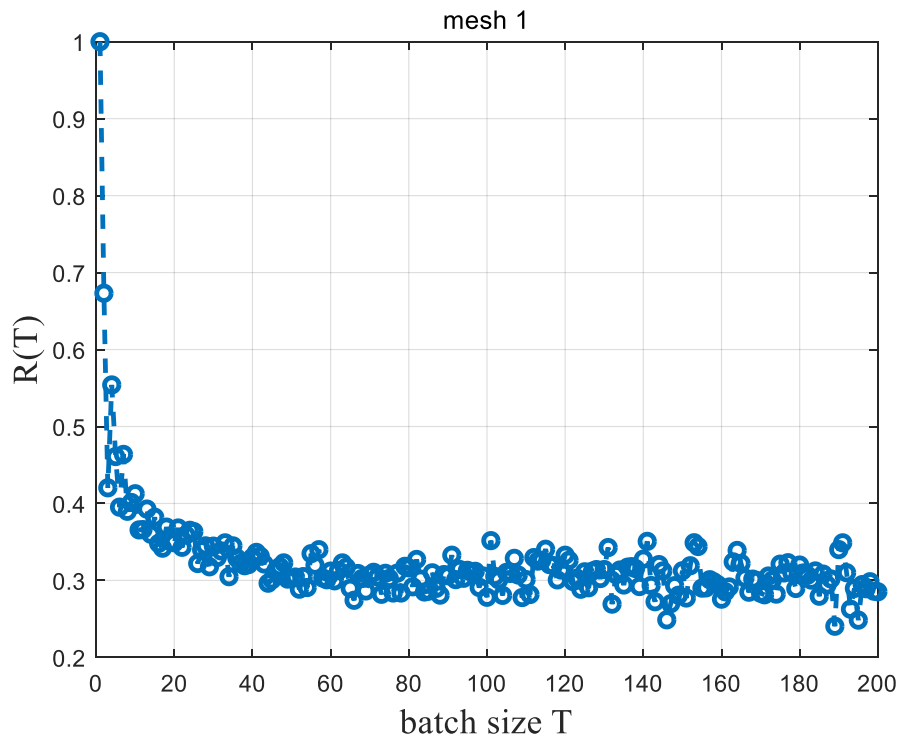
Figure V-15: Standard deviation of 1st mesh with different batch size at EOC.

5.4. BEAVRS Cycle 1

5.4.1. Simulation Result

The Cycle 1 simulation was performed with following condition:
- BEAVRS quarter core geometry
- ENDF-VII.1 library
- Feedbacks (thermal hydraulics, equilibrium xenon, critical boron concentration, on-the-fly Doppler broadening)
- Semi predictor corrector algorithm
- 4 inactive cycles, 20 active cycles, 300 subcycles, and 100,000 histories per subcycle
- 1 radial ring and 20 axial meshes per pin
- 15 burnup steps
- 100% power
- All rod out condition

The simulation was performed with 45 processors on Linux cluster (Intel Xeon E5-2620 @ 3.00GHz). It cost 13 GB memory per processor and 28 hours per one step calculation when the number of isotopes in burnup cell is saturated. Figure V-16 shows the critical boron concentration curves of MCS together with measurement, MPACT [62], and ST/RK. The critical boron concentration change trend matches very well with measurement, but it shows 35 ppm discrepancy between MCS and measurement as shown in Figure V-17 while the critical boron concentration of three codes matches within 20 ppm. It should be noted that the standard deviation of estimated critical boron concentration is less than 0.5 ppm for all burnup points. Figure V-18 presents the assembly power, core average axial power density, core average axial fuel temperature, and core average axial coolant temperature at beginning of cycle (EFPD = 2.4). The assembly power distribution agrees very well with RMS error of 0.95% while standard deviation of assembly power is about 0.3%. The core average axial distributions match well except spacer grid location. MCS results of power and fuel temperature show small deep at the location of spacer grid since MCS modeled the spacer grid explicitly while ST/RK used smeared spacer grid model. Figure V-19 and Figure V-20 present same quantity at the middle of cycle (EFPD = 144) and end of cycle (EPFD = 300). The assembly power distributions of both step match very well with RMS error of 0.34% and 0.58%. The core average axial distributions also agree very well.
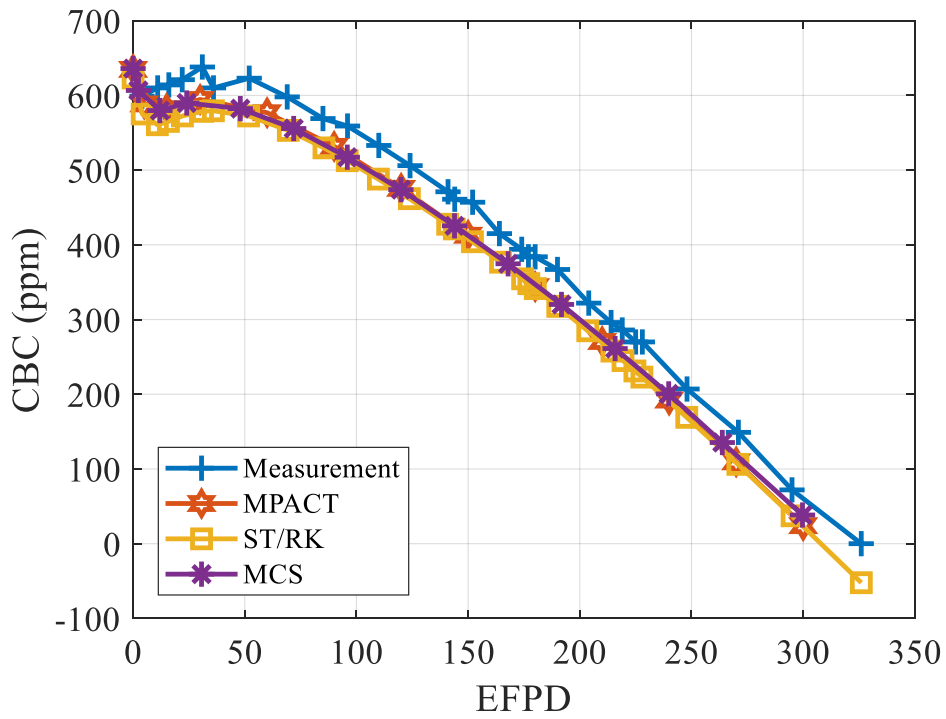
Figure V-16: Critical boron concentration curve for BEAVRS Cycle 1.
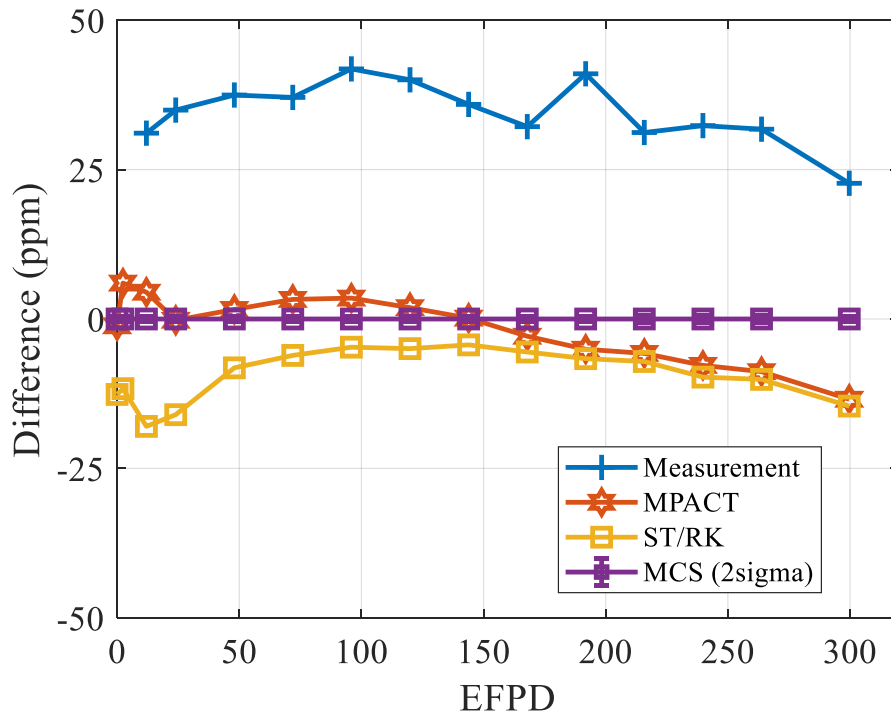
Figure V-17: Critical boron concentration difference for BEAVRS Cycle 1.

ST/RK / MCS / Rel. Diff. (%)							
1.112 / 1.117 / -0.368	1.230 / 1.223 / 0.573	1.216 / 1.201 / 1.252	1.370 / 1.359 / 0.816	1.187 / 1.173 / 1.134	1.191 / 1.190 / 0.073	1.068 / 1.071 / -0.274	1.035 / 1.054 / -1.796
1.230 / 1.221 / 0.761	1.186 / 1.169 / 1.445	1.368 / 1.353 / 1.129	1.233 / 1.217 / 1.359	1.320 / 1.310 / 0.754	1.116 / 1.109 / 0.709	1.222 / 1.239 / -1.402	1.077 / 1.098 / -1.901
1.216 / 1.196 / 1.675	1.368 / 1.352 / 1.199	1.243 / 1.224 / 1.522	1.363 / 1.352 / 0.870	1.171 / 1.160 / 0.962	1.180 / 1.179 / 0.084	1.036 / 1.037 / -0.124	0.956 / 0.970 / -1.444
1.370 / 1.356 / 0.984	1.233 / 1.217 / 1.368	1.363 / 1.352 / 0.828	1.210 / 1.200 / 0.859	1.257 / 1.257 / -0.065	1.125 / 1.124 / 0.160	1.184 / 1.197 / -1.037	0.779 / 0.792 / -1.535
1.187 / 1.173 / 1.144	1.320 / 1.311 / 0.739	1.171 / 1.160 / 0.920	1.257 / 1.258 / -0.119	1.461 / 1.489 / -1.924	1.173 / 1.178 / -0.363	1.176 / 1.191 / -1.293	
1.191 / 1.190 / 0.064	1.116 / 1.109 / 0.658	1.180 / 1.179 / 0.077	1.125 / 1.123 / 0.199	1.173 / 1.177 / -0.307	1.147 / 1.151 / -0.345	0.851 / 0.863 / -1.437	
1.068 / 1.070 / -0.134	1.222 / 1.236 / -1.122	1.036 / 1.034 / 0.216	1.184 / 1.194 / -0.866	1.176 / 1.189 / -1.075	0.851 / 0.861 / -1.187		
1.035 / 1.049 / -1.324	1.077 / 1.094 / -1.486	0.956 / 0.966 / -0.998	0.779 / 0.788 / -1.113				

Rel. Diff.	
Max	1.96
Min	-1.65
RMS	0.95

ST/RK
MCS
Rel. Diff. (%)
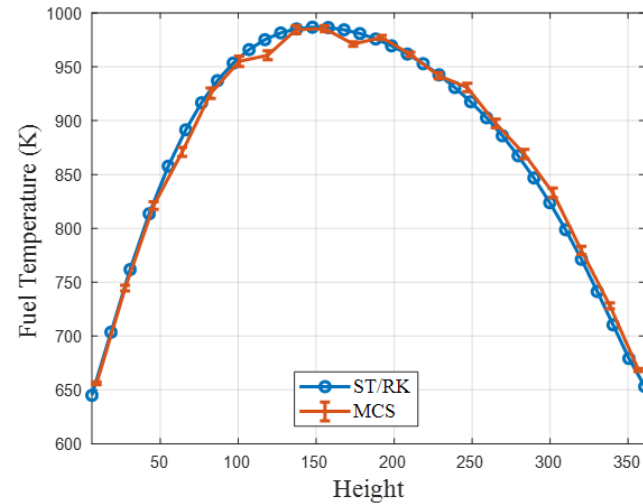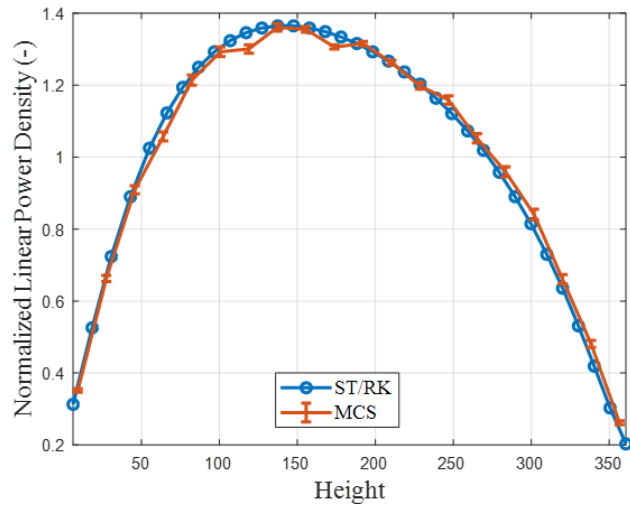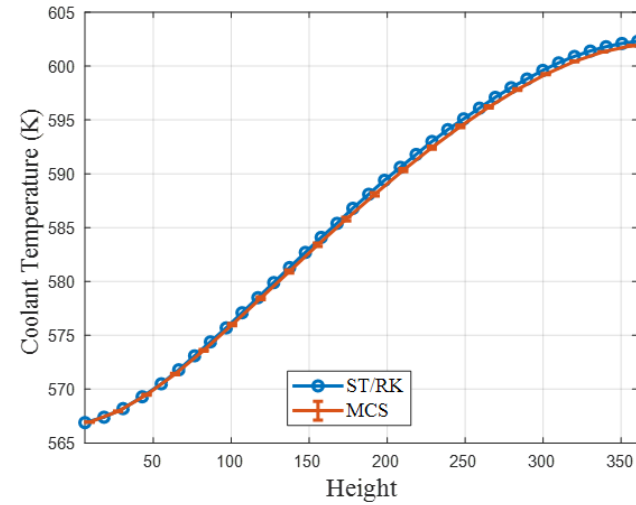
Figure V-18: Assembly power and axial distribution of MCS and ST/RK for BEAVRS Cycle 1 BOC.

109

1.171	1.315	1.222	1.369	1.204	1.272	1.085	0.969
1.194	1.319	1.217	1.368	1.198	1.268	1.079	0.974
-1.929	-0.334	0.424	0.041	0.556	0.309	0.554	-0.444
1.315	1.212	1.371	1.226	1.345	1.160	1.264	0.991
1.321	1.210	1.368	1.220	1.342	1.153	1.265	0.996
-0.448	0.156	0.166	0.469	0.261	0.624	-0.096	-0.548
1.222	1.371	1.231	1.368	1.198	1.256	1.046	0.899
1.217	1.367	1.223	1.365	1.192	1.253	1.040	0.904
0.391	0.282	0.665	0.236	0.503	0.251	0.526	-0.542
1.369	1.226	1.368	1.222	1.320	1.145	1.169	0.728
1.366	1.217	1.365	1.220	1.323	1.143	1.176	0.735
0.230	0.701	0.273	0.246	-0.255	0.189	-0.640	-0.951
1.204	1.345	1.198	1.320	1.385	1.210	1.073	
1.192	1.338	1.190	1.321	1.417	1.218	1.084	
0.999	0.546	0.651	-0.092	-2.227	-0.603	-0.939	
1.272	1.160	1.256	1.145	1.210	1.140	0.771	
1.264	1.147	1.249	1.139	1.215	1.151	0.783	
0.680	1.114	0.521	0.486	-0.399	-0.963	-1.453	
1.085	1.264	1.046	1.169	1.073	0.771		
1.073	1.259	1.038	1.172	1.082	0.782		
1.136	0.391	0.769	-0.306	-0.754	-1.335		
0.969	0.991	0.899	0.728				
0.969	0.994	0.901	0.733				
0.073	-0.302	-0.240	-0.667				

Rel. Diff.	
Max	2.28
Min	-1.12
RMS	0.34

ST/RK
MCS
Rel. Diff. (%)
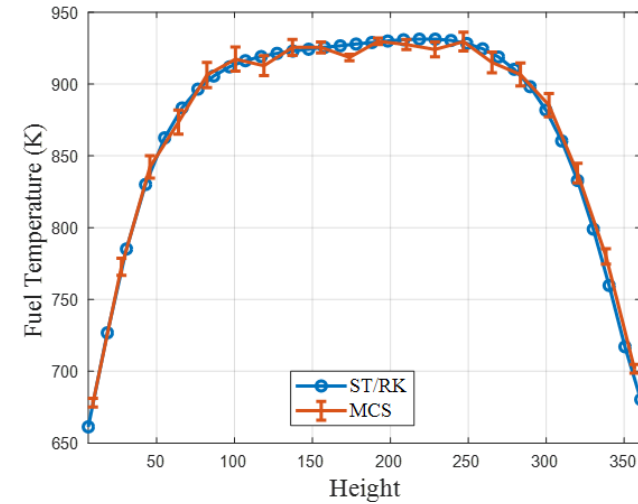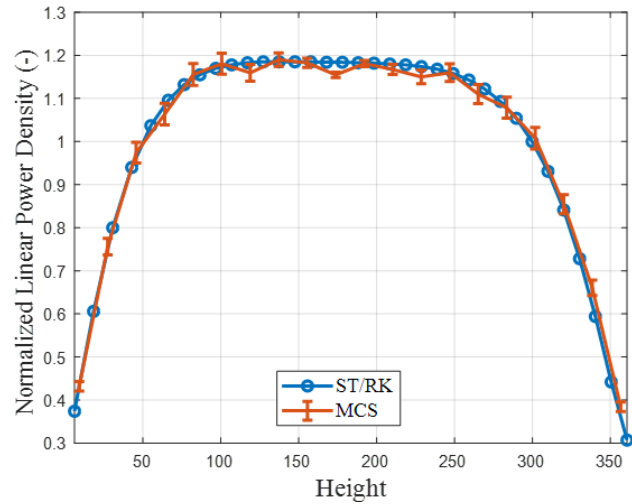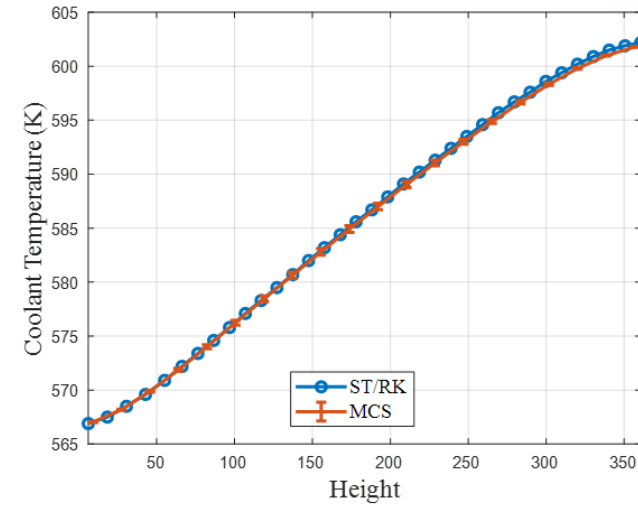
Figure V-19: Assembly power and axial distribution of MCS and ST/RK for BEAVRS Cycle 1 MOC.

1.098	1.249	1.136	1.282	1.162	1.305	1.131	1.019
1.138	1.269	1.137	1.280	1.148	1.293	1.116	1.011
-3.560	-1.567	-0.110	0.205	1.254	0.899	1.369	0.730
1.249	1.130	1.273	1.149	1.301	1.173	1.349	1.028
1.268	1.138	1.278	1.143	1.293	1.158	1.335	1.021
-1.448	-0.650	-0.397	0.476	0.633	1.292	1.016	0.628
1.136	1.273	1.144	1.292	1.167	1.295	1.096	0.958
1.138	1.278	1.141	1.290	1.160	1.286	1.082	0.950
-0.163	-0.433	0.269	0.183	0.573	0.701	1.313	0.861
1.282	1.149	1.292	1.170	1.311	1.161	1.235	0.781
1.287	1.150	1.296	1.170	1.317	1.155	1.228	0.774
-0.385	-0.102	-0.275	0.034	-0.441	0.598	0.556	0.820
1.162	1.301	1.167	1.311	1.331	1.261	1.092	
1.160	1.304	1.169	1.322	1.370	1.268	1.090	
0.221	-0.183	-0.125	-0.834	-2.888	-0.536	0.163	
1.305	1.173	1.295	1.161	1.261	1.213	0.804	
1.304	1.169	1.295	1.162	1.271	1.222	0.806	
0.005	0.395	-0.027	-0.006	-0.785	-0.783	-0.280	
1.131	1.349	1.096	1.235	1.092	0.804		
1.124	1.346	1.090	1.238	1.097	0.808		
0.639	0.205	0.589	-0.199	-0.419	-0.568		
1.019	1.028	0.958	0.781				
1.019	1.029	0.958	0.781				
-0.043	-0.146	0.068	-0.083				

Rel. Diff.	
Max	3.69
Min	-1.35
RMS	0.58

ST/RK
MCS
Rel. Diff. (%)
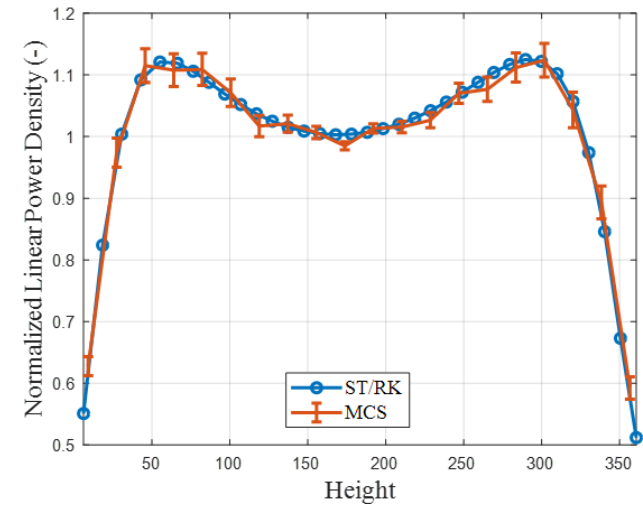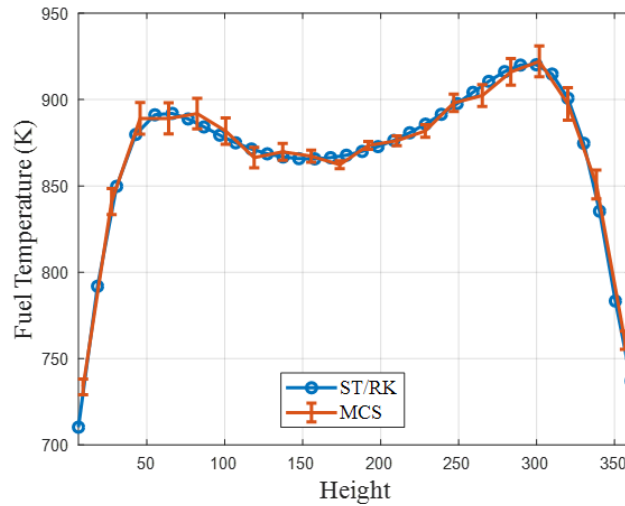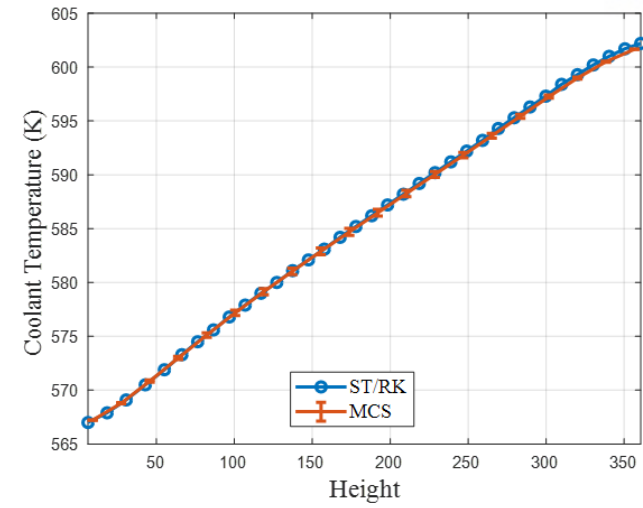
Figure V-20: Assembly power and axial distribution of MCS and ST/RK for BEAVRS Cycle 1 EOC.

111

The operation history of Cycle 1 is quite complex as shown in the Figure V-21. The power alters very frequently as well as control rod position. BEAVRS provides the measured detector signal at 24 points which is marked in blue dot together with inlet coolant temperature, rod position, power. In order to produce detector signal with given condition, MCS simulations were performed with restart capability by using the number density produced by previous simulation with 100% all rod out condition. The MCS simulations were performed by employing 4 inactive cycles, 20 active cycle, 300 subcycles, and 10,000 histories per subcycle.
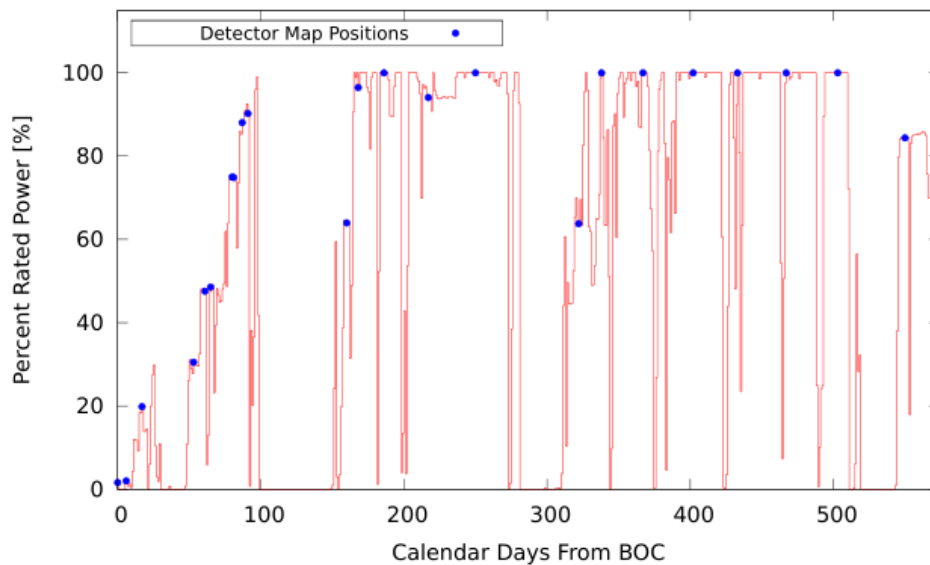
Figure V-21: Power history of BEAVRS Cycle 1.

Benchmark provides tilt corrected detector signal together with original detector signal since the original signal is tilted a lot. The detector signal was calculated by inserting very small about of 235U input instrument tube and tally the fission reaction rate. The maximum, minimum, and RMS difference of detector signal for 22 burnup points are compared and summarized in Table II. The detector signal matches very well with 1.5-3% RMS error while the standard deviation is about 1-2%. The radial detector signals are presented for selected three points represent BOC (EFPD = 0), MOC (EFPD = 111 days), and EOC (EFPD=296 days). At BOC, the RMC different is 1.84% as shown in Figure V-22. The MOC and EOC also shows good agreement with RMS error of 2.45% and 2.30% as shown in Figure V-23 and Figure V-24. Overall, MCS result of Cycle 1 shows good agreement with ST/RK and measured data.

Table V-3: Detector Signal Comparison for BEAVRS Cycle 1.

EFPD	Max (%)	Min (%)	RMS (%)
0.00	4.56	-3.36	1.84
0.93	3.78	-4.67	2.00
3.58	4.56	-6.53	2.33
6.43	6.21	-5.19	3.04
15.46	3.17	-4.68	2.01
16.05	3.52	-3.54	1.77
21.07	2.46	-3.84	1.67
24.54	5.23	-5.59	2.54
36.13	3.08	-4.86	1.96
51.86	0.94	-5.64	2.68
79.07	2.77	-5.81	2.07
110.63	0.75	-5.19	2.45
144.18	1.46	-6.18	2.62
155.65	1.81	-4.64	2.49
180.05	3.73	-6.61	2.02
208.66	2.88	-5.48	2.25
235.09	5.11	-4.85	2.55
265.81	3.43	-5.50	2.08
295.96	0.93	-4.33	2.30
309.72	4.00	-5.61	3.10
326.23	2.11	-5.44	2.79

Figure V-22: Radial detector signal for BERA Cycle 1 at BOC (EDPF = 0 days).

-	0.779	1.065	0.940	1.147	0.935	1.264	0.778
-	0.764	1.049	0.934	1.158	0.925	1.282	0.789
-	-1.920	-1.531	-0.689	0.932	-1.085	1.397	1.369
0.779	1.011	0.897	1.143	0.974	1.168	0.873	0.815
0.764	0.989	0.906	1.147	0.971	1.218	0.869	0.827
-1.920	-2.170	1.003	0.357	-0.290	4.307	-0.472	1.526
1.065	0.897	1.138	0.968	1.212	0.984	1.242	0.728
1.049	0.893	1.145	0.976	1.221	1.004	1.287	0.733
-1.531	-0.416	0.632	0.800	0.769	2.035	3.615	0.646
0.940	1.143	0.968	1.249	-	1.307	-	0.584
0.934	1.143	0.935	1.259	-	1.367	-	0.598
-0.689	-0.026	-3.364	0.802	-	4.558	-	2.342
1.147	0.974	1.212	-	1.343	1.196	0.958	
1.158	0.955	1.196	-	1.332	1.195	0.960	
0.932	-1.982	-1.320	-	-0.782	-0.105	0.192	
0.935	1.168	0.984	1.307	1.196	0.852	0.702	
0.925	1.187	0.974	1.363	1.192	0.834	0.691	
-1.085	1.629	-1.027	4.258	-0.301	-2.076	-1.582	
1.264	0.837	1.242	-	0.958	0.702		
1.282	0.868	1.259	-	0.945	0.714		
1.397	3.696	1.361	-	-1.362	1.674		
0.778	0.815	0.728	0.584				
0.789	0.793	0.723	0.590				
1.369	-2.655	-0.632	1.008				

Rel. Diff.	
Max	4.56%
Min	-3.36%
RMS	1.84%

BEAVRS
MCS
Rel. Diff. (%)

Figure V-22: Radial detector signal for BERA Cycle 1 at BOC (EDPF = 0 days).

-	1.071	1.321	1.126	1.297	1.037	1.180	0.666
-	1.037	1.288	1.102	1.285	1.031	1.189	0.661
-	-3.184	-2.465	-2.156	-0.947	-0.543	0.755	-0.822
1.071	1.312	1.126	1.322	1.103	-	0.844	0.678
1.037	1.295	1.097	1.312	1.058	-	0.818	0.662
-3.184	-1.286	-2.604	-0.760	-4.116	-	-3.113	-2.433
1.321	1.126	1.343	1.124	1.278	1.022	1.139	0.617
1.288	1.070	1.289	1.100	1.254	0.992	1.135	0.604
-2.465	-4.971	-4.041	-2.170	-1.876	-2.888	-0.390	-2.106
1.126	1.322	1.124	1.315	-	1.225	-	0.508
1.102	1.300	1.066	1.286	-	1.195	-	0.485
-2.156	-1.662	-5.194	-2.215	-	-2.482	-	-4.570
1.297	1.103	1.278	-	1.105	1.010	0.730	
1.285	1.080	1.266	-	1.065	0.982	0.713	
-0.947	-2.067	-0.938	-	-3.633	-2.723	-2.263	
1.037	-	1.022	1.225	1.010	0.710	0.533	
1.031	-	0.999	1.230	0.986	0.697	0.511	
-0.543	-	-2.240	0.434	-2.372	-1.813	-4.210	
1.180	0.844	1.139	-	0.730	0.533		
1.189	0.826	1.116	-	0.725	0.527		
0.755	-2.126	-1.991	-	-0.641	-1.106		
0.666	0.678	0.617	0.508				
0.661	0.669	0.614	0.495				
-0.822	-1.374	-0.556	-2.463				

Rel. Diff.	
Max	0.75%
Min	-5.19%
RMS	2.45%

BEAVRS
MCS
Rel. Diff. (%)

Figure V-23: Radial detector signal for BERA Cycle 1 at MOC (EDPF = 111 days).

114

- - -	- - -	1.211 1.194 -1.388	1.053 1.046 -0.621	1.219 1.222 0.246	1.073 1.041 -2.941	1.205 1.205 0.012	0.695 0.672 -3.306
- - -	1.209 1.200 -0.705	1.051 1.054 0.300	1.218 1.214 -0.295	1.075 1.033 -3.909	- - -	0.920 0.895 -2.730	0.705 0.675 -4.217
1.211 1.194 -1.388	1.051 1.016 -3.297	1.218 1.193 -2.062	1.079 1.041 -3.485	1.225 1.223 -0.123	1.067 1.033 -3.198	1.171 1.155 -1.400	0.654 0.630 -3.626
1.053 1.046 -0.621	1.218 1.199 -1.570	1.079 1.051 -2.594	1.252 1.241 -0.869	- - -	1.243 1.246 0.214	- - -	0.546 0.525 -3.812
1.219 1.222 0.246	1.075 1.048 -2.506	1.225 1.226 0.100	- - -	1.143 1.114 -2.521	1.086 1.050 -3.270	0.759 0.749 -1.349	
1.073 1.041 -2.941	- - -	1.067 1.057 -0.936	1.243 1.237 -0.471	1.086 1.056 -2.733	- - -	0.560 0.544 -2.870	
1.205 1.205 0.012	0.920 0.907 -1.377	1.171 1.171 -0.037	- - -	0.759 0.729 -3.917	0.560 0.550 -1.719		
0.695 0.672 -3.306	0.705 0.712 0.929	0.654 0.656 0.298	0.546 0.522 -4.329				

Rel. Diff.	
Max	0.93%
Min	-4.33%
RMS	2.30%

BEAVRS
MCS
Rel. Diff. (%)

Figure V-24: Radial detector signal for BERA Cycle 1 at EOC (EDPF = 296 days).

The pin-wise power, flux, fuel temperature, coolant density at BOC, EOC, and EOC are shown in the Figure V-25. The local quantity tally results look reasonable proving that the capability of MCS Cycle simulation.
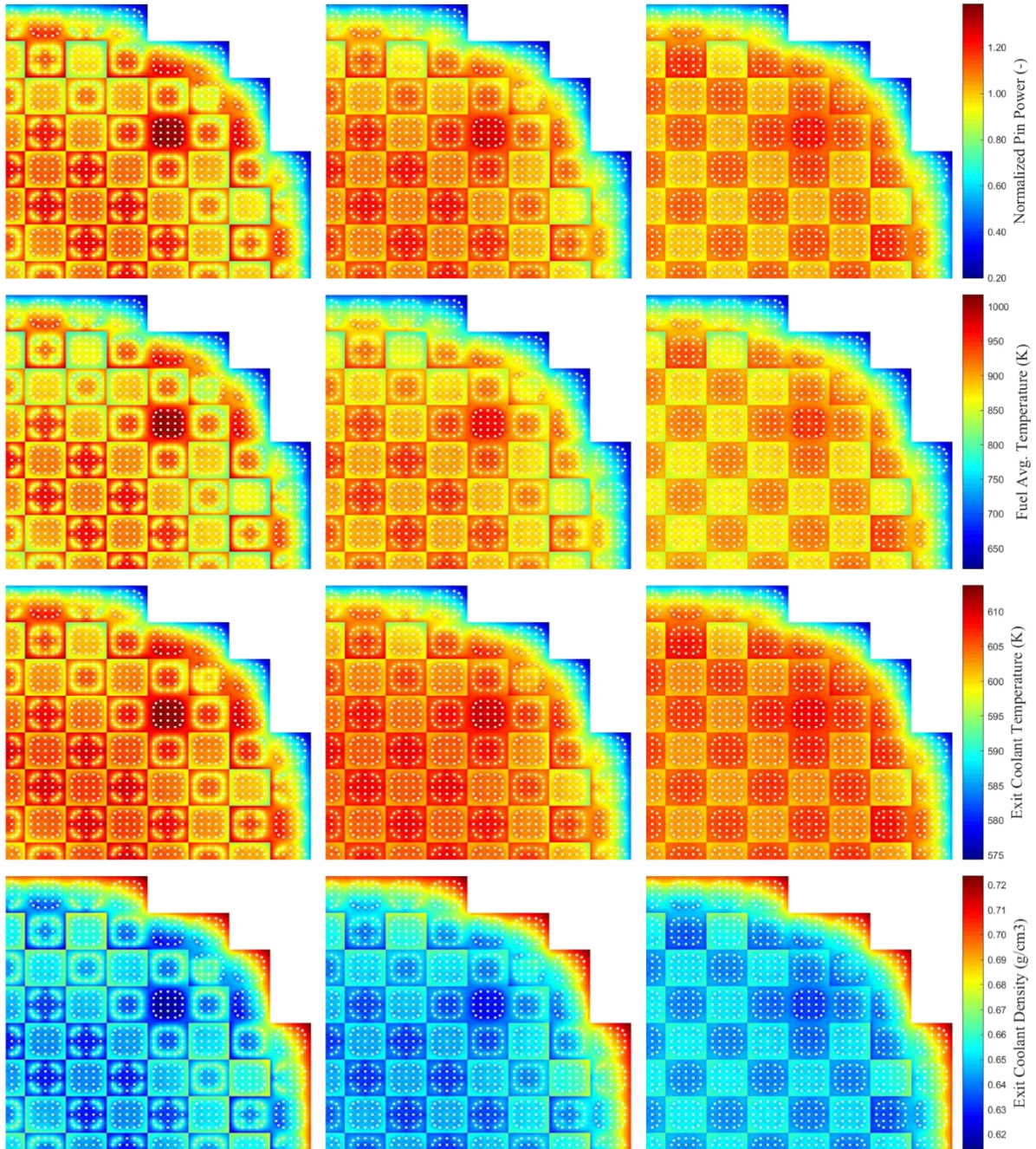

Figure V-25: Pin power, fuel average temperature, exit coolant temperature and exit coolant density for BEAVRS Cycle 1 at BOC, MOC, and EOC.

5.4.2. Statistical Uncertainty

The 95/95 1% criterion is often suggested as a convergence criterion of MC fission source distribution. The 95/95 criterion means that uncertainty of tally result should be treated with at least a 95% probability at a 95% confidence level. To achieve 95/95 criterion, the standard deviation of tally mesh at 95% probability should be lower than 0.51% (1/1.96). In Monte Carlo simulation, the standard deviation decreases as more histories are used, and increases with more tally mesh. There are 50,952 pins in BEAVRS core, and the number of mesh increases proportional to the number of radial mesh and axial mesh in one pin. It is important to know what the statistical uncertainty and how many histories are required to meet the criterion of 95/95 to decide the running strategy and to estimates to computing.

The statistical uncertainty calculated in the section 5.3 by using BEAVRS quarter core geometry was used to estimate the computing time required to meet 95/95 criteria. The simulation was performed with 4 inactive cycles, 30 active cycles, 300 subcycles, and 20,000 histories per subcycle (total history in active cycles = 180,000,000). Figure V-26 presents the cumulative density of apparent and real standard deviation of mesh-wise tally at BOC and EOC. As shown in the figure, the 95% points of real and apparent at BOC are similar around 8.2%, and the 95% of real and apparent at EOC are 7.3% and 6.5%. The computing time to meet 95/95 criteria is estimated by using the real standard deviation by assuming the standard deviation will decreases as $1/\sqrt{N}$. MCS can treat the 1500 particles per second at BOC, and the standard deviation of 95% point is 8.3%. In order to decreases 8.3% to 0.51%, 16.27 times more history should be used. The expected computing to run 2,929,411,764 (=180,000,000 16.27 =) histories is 22.6 days with single processor. MCS can treat the 200 particles per second at EOC, and the standard deviation of 95% point is 6.5%. Thus, it will cost 132.76 days to meet 95/95 criteria at EOC with single processor. The estimated simulation time is summarized in Table V-4.

Table V-4: Transport Time to Meet 95/95 Criterion for BEAVRS Quarter Core with 20 Axial Meshes.

	BOC	EOC
History per Second-Proc.	1,500	200
History for 95/95 1% Criterion	2,929,411,764	2,294,117,647
Transport Time with Single Proc. (days)	22,6	132.76
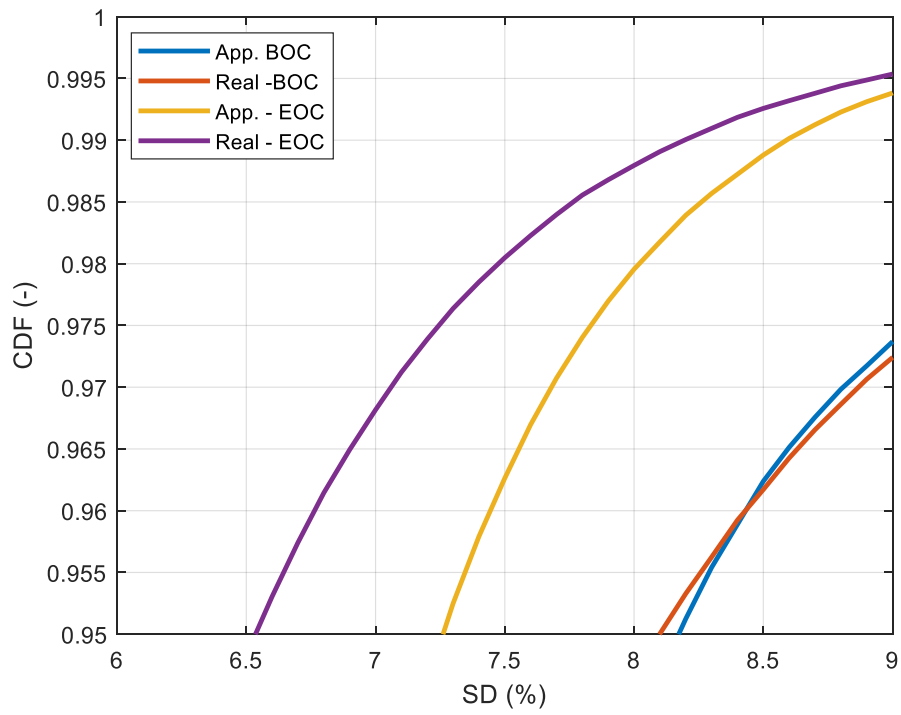
Figure V-26: Cumulative density of real and apparent standard deviation of mesh-wise power for BEAVRS Cycle 1 at BOC and EOC.

5.5. BEAVRS Cycle 2

5.5.1. Refueling

To perform the BEAVRS Cycle 2 simulation, the assemblies at the end of Cycle 1 should be shuffled and fresh fuel should be loaded according to the given loading pattern shown in Figure V-27. The challenge here is that there are 128,280 fuel mesh in the quarter core, and there are about 250 nuclides in a single mesh. This is almost impossible to make shuffled core manually.
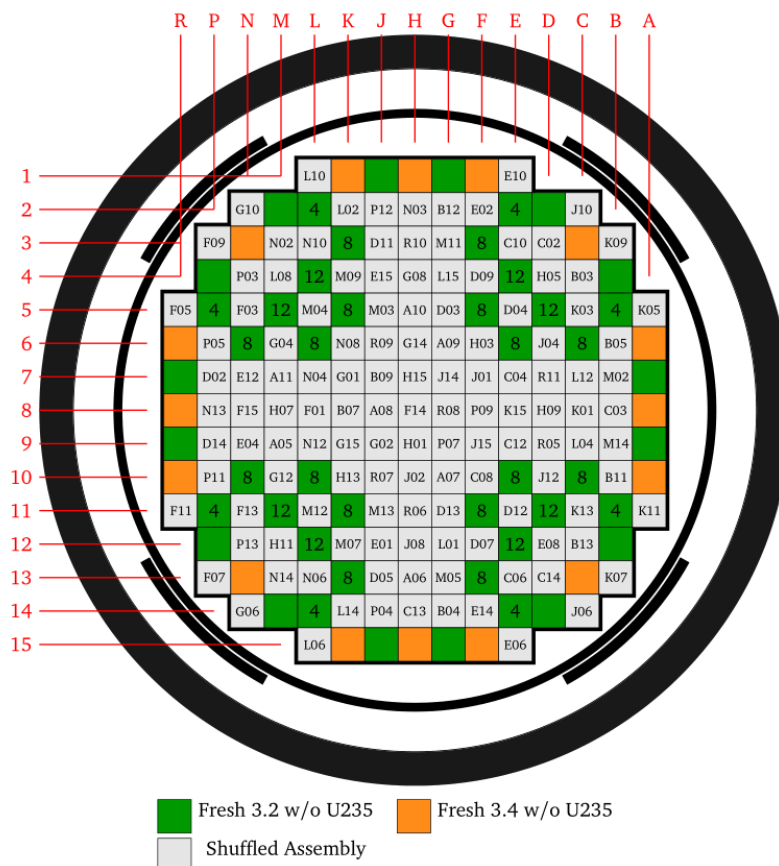
Figure V-27: BEAVRS Cycle 2 shuffling pattern.

For the refueling, MCS prints the number density of each assembly into separate files at the end of Cycle 1. For Cycle 2, MCS replace the number density in each assembly by using the files assigned by user. The MCS input should be ready for Cycle 2 refueling as shown in Figure V-28. The Cycle 2 input has fresh fuels in green and orange color with the assemblies ready to be replaced in red. The material composition in the red assembly will be replaced for the Cycle 2 simulation. Figure V-29 shows the ^{235}U number density at the end of Cycle 1 and beginning of Cycle 2. The gradation of uranium density

can be clearly observed showing that the fuel is depleted well during Cycle 1 and it is shuffled well for Cycle 2 simulation. It should be noted that the refueling assemblies had 100 days cooling time.
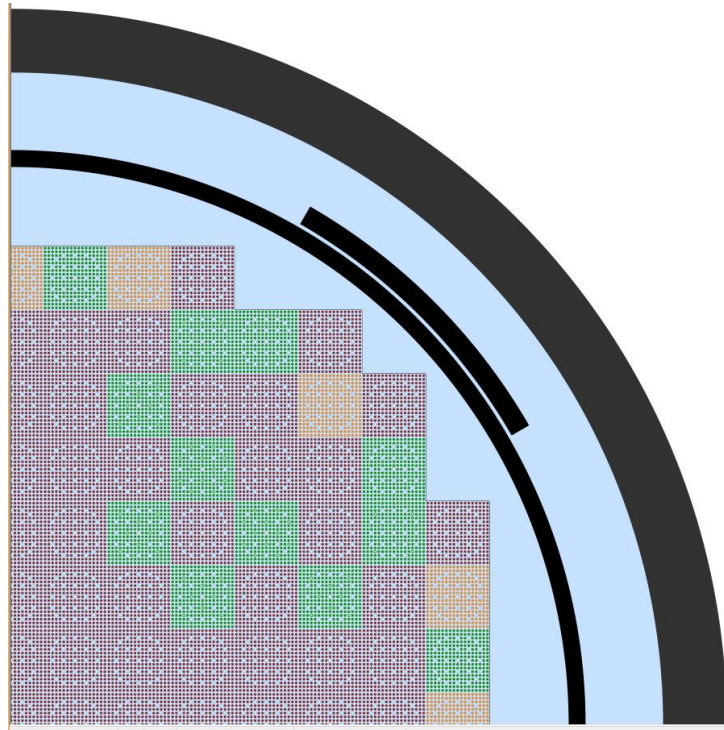
Figure V-28: Configuration of BEAVRS Cycle 2 before refueling.
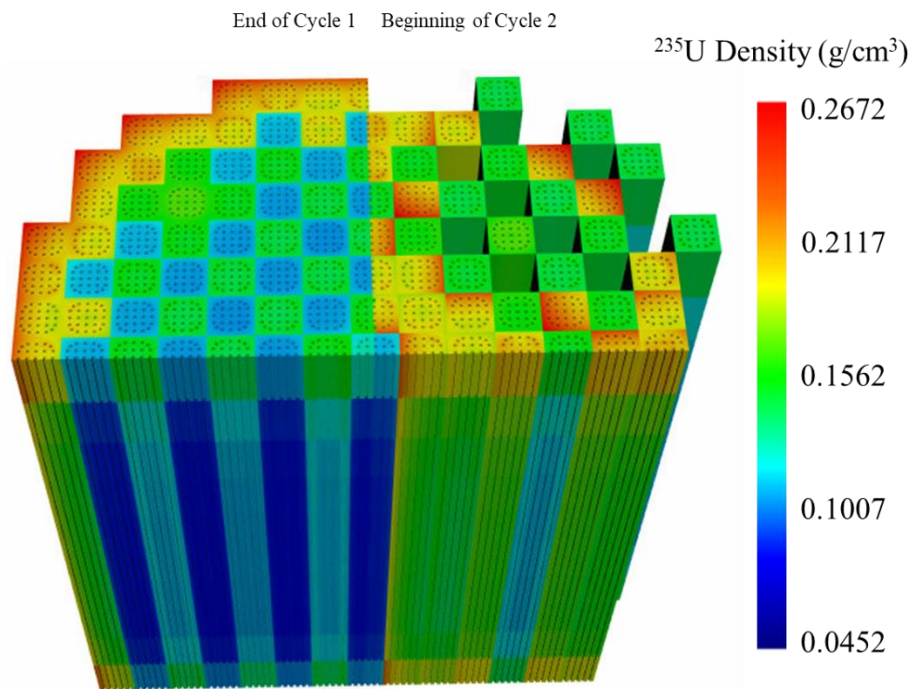
Figure V-29: ^{235}U density at the end of Cycle 1 and beginning of Cycle2.

5.5.2. Cycle 2 Simulation

The BOC HZP is performed prior to Cycle 2 simulation to check whether the modeling is done well. The simulation is performed for with 300 subcycles, 4 inactive cycles, 30 active cycle, and 10,000 histories per subcycle. MCS result of critical boron concentration is compared with measured data and MPACT solution [62] as in Table V-5. MCS shows very good agreement different within 20 ppm comparing measured data and 7 ppm comparing MPACT result.

Figure V-32 shows the power history and detector map positions, there are 15 detector signals are given. MCS simulation is performed with 100% power level with 300 multicycles, 4 inactive cycles, 20 active cycles, and 10,000 histories per multicycle. The simulation time and memory requirement are similar with it of end of Cycle 1. It takes about 4 hours with 6GB memory per processor.

Table V-5: Critical Boron Concentration for BEAVRS Cycle 2 BOC HZP.

| Rod	Measured (ppm)	MCS (ppm)	SD (ppm)	MPACT (ppm)
ARO	1405	1380	1.24	1387

The Cycle 2 simulation was performed with following condition:
- BEAVRS quarter core geometry
- ENDF-VII.1 library
- Feedbacks (thermal hydraulics, equilibrium xenon, critical boron concentration, on-the-fly Doppler broadening)
- Semi predictor corrector algorithm
- 4 inactive cycles, 20 active cycles, 300 subcycles, and 10,000 histories per subcycle
- 1 radial ring and 20 axial meshes per pin
- 15 burnup steps
- 100% power
- All rod out condition

Figure V-30 presents the critical boron concentration curves of MCS, MPACT, ST/RK, and measurement. The critical boron concentration of four data match very well within 25 ppm except the MCS and ST/RK at beginning of cycle. The discrepancy of MCS and ST/RK is originated from the cooling time. MCS considered the 100 days cooling time while ST/RK does not considered it. Since MCS considered cooling time, neutron absorber such as xenon and fission products are decayed out. Thus, the critical boron concentration of MCS at BOC is much higher than it of ST/RK.

The operation history of Cycle 2 is much simpler than it of Cycle 1 as shown in Figure V-32, and there are 14 data point which provides detector signal marked in blue. Unlikely Cycle 1, the data points of Cycle 2 is almost 100% power and all rod out state. Thus, the detector signals are calculated during Cycle simulation. Among 14 data points, 10 data points are selected to compare detector signal which produced which 100% power. The maximum, minimum, and RMS difference are calculated and summarized in the Table V-6.   As shown in the table, MCS detector signal result shows good agreement against measured data. The RMS error is about 1.5-3% for all points while the standard deviation is about 1-2%.
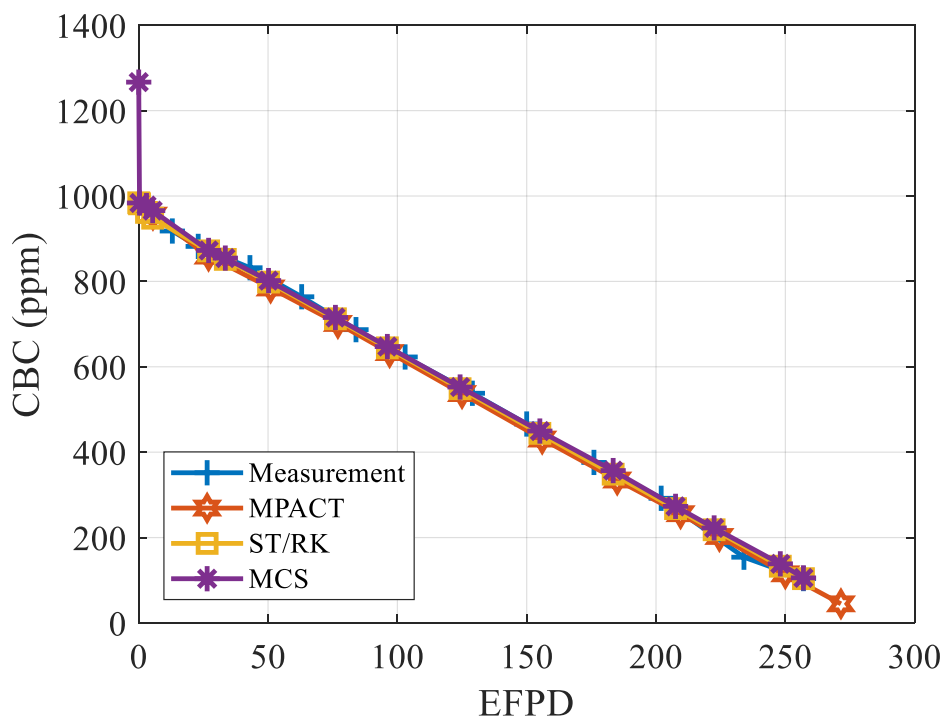
Figure V-30: CBC curve for BEAVRS Cycle 2.
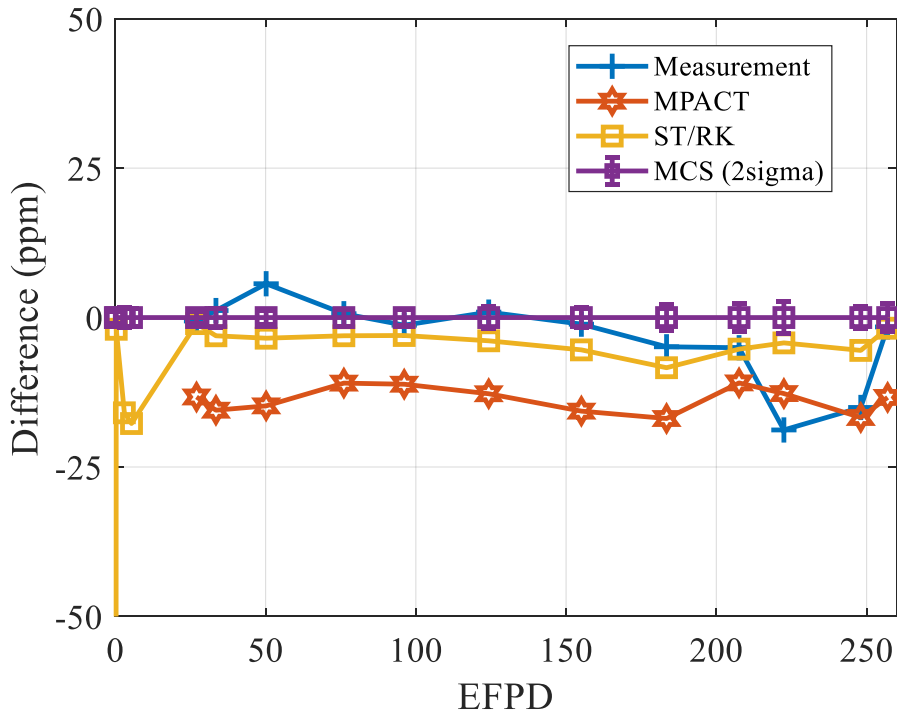
Figure V-31: CBC difference curve for BEAVRS Cycle 2.
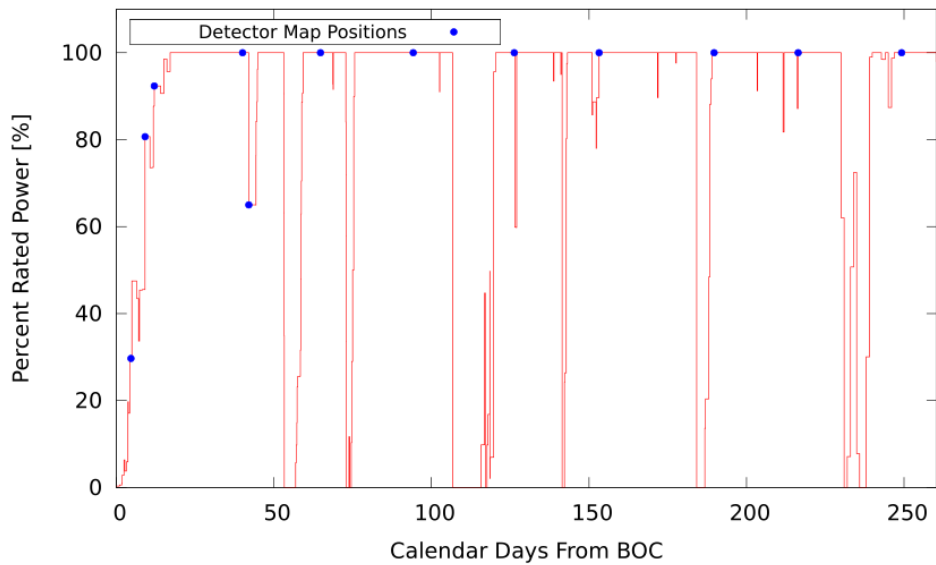
Figure V-32: Power history of BEAVRS Cycle 2.

The radial detector signals for selected three points are compared representing BOC (EDPC=5.39), MOC (EFPD =124.25), and MOC (EFPD=248.06). Figure V-33 shows the radial signal at the BOC. It shows RMS difference of 2.87% and maximum absolute difference of 6.34%. Figure V-34 shows the radial signal at the MOC. It shows RMC difference of 2.11% and maximum absolute difference of

6.21%. Figure V-35 shows the detector signal at the EOC. It shows the RMC difference of 1.65% and maximum absolute difference of 5.89%. Overall, MCS result of Cycle 2 shows good agreement and the local quantity tally results looks reasonable proving that the capability of MCS multi-cycle simulation.

Table V-6: Detector Signal Comparison for BEAVRS Cycle 2.

EFPD	Max (%)	Min (%)	RMS (%)
5.39	2.98	-6.34	2.87
27.02	1.59	-6.01	3.04
50.19	0.50	-6.86	2.76
96.13	1.98	-4.55	2.14
124.25	2.85	-6.21	2.11
155.09	3.60	-4.00	1.74
183.43	5.72	-4.09	2.35
207.55	2.85	-3.89	1.90
222.47	3.98	-4.16	1.73
248.06	2.74	-5.89	1.65

Radial detector signal map (each cell: BEAVRS / MCS / Rel. Diff. (%)):

|							
- / - / -	1.167 / 1.179 / 1.032	1.136 / 1.138 / 0.137	1.147 / 1.122 / -2.166	1.135 / 1.109 / -2.261	1.069 / 1.040 / -2.726	1.055 / 1.011 / -4.196	0.901 / 0.900 / -0.157
1.167 / 1.179 / 1.032	1.160 / 1.149 / -0.967	1.179 / 1.133 / -3.917	1.191 / 1.192 / 0.071	1.094 / 1.100 / 0.564	- / - / -	1.063 / 1.032 / -2.885	0.941 / 0.886 / -5.839
1.136 / 1.138 / 0.137	1.167 / 1.129 / -3.271	1.203 / 1.189 / -1.170	- / - / -	1.153 / 1.104 / -4.216	1.024 / 1.021 / -0.282	- / - / -	0.752 / 0.748 / -0.471
1.147 / 1.122 / -2.166	- / - / -	1.069 / 1.041 / -2.633	1.118 / 1.096 / -1.946	- / - / -	1.096 / 1.075 / -1.928	- / - / -	0.492 / 0.466 / -5.195
1.135 / 1.109 / -2.261	1.128 / 1.079 / -4.335	- / - / -	- / - / -	1.011 / 1.041 / 2.983	1.000 / 0.998 / -0.202	0.803 / 0.818 / 1.828	
1.069 / 1.040 / -2.726	1.164 / 1.090 / -6.339	- / - / -	1.117 / 1.050 / -5.959	- / - / -	0.921 / 0.920 / -0.115	0.460 / 0.448 / -2.666	
1.055 / 1.011 / -4.196	- / - / -	1.031 / 0.993 / -3.691	- / - / -	- / - / -	0.462 / 0.456 / -1.282		
0.901 / 0.900 / -0.157	0.883 / 0.904 / 2.358	- / - / -	0.473 / 0.477 / 0.865				

Rel. Diff.	
Max	2.98%
Min	-6.34%
RMS	2.87%

| BEAVRS |
| MCS |
| Rel. Diff. (%) |

Figure V-33 Radial detector signal for BERA Cycle 2 at BOC (EDPF = 5.39 days).

124

Figure V-34 table — BEAVRS / MCS / Rel. Diff. (%)

1	2	3	4	5	6	7	8
-	1.051	1.047	1.068	1.120	1.037	1.019	0.814
-	1.081	1.050	1.069	1.129	1.029	1.003	0.799
-	2.850	0.329	0.133	0.778	-0.751	-1.550	-1.822
1.051	1.048	1.090	1.179	1.088	-	-	0.843
1.081	1.071	1.068	1.176	1.078	-	-	0.802
2.850	2.232	-2.047	-0.262	-0.937	-	-	-4.848
1.047	1.090	1.213	-	1.229	1.064	-	0.741
1.050	1.093	1.209	-	1.213	1.042	-	0.723
0.329	0.246	-0.363	-	-1.285	-2.089	-	-2.385
1.068	-	1.077	1.255	-	1.188	-	0.533
1.069	-	1.057	1.225	-	1.177	-	0.500
0.133	-	-1.864	-2.420	-	-0.935	-	-6.208
1.120	1.093	-	-	1.148	1.065	0.814	
1.129	1.091	-	-	1.172	1.036	0.788	
0.778	-0.228	-	-	2.100	-2.703	-3.240	
1.037	1.156	-	1.200	-	0.914	0.506	
1.029	1.141	-	1.190	-	0.921	0.511	
-0.751	-1.323	-	-0.867	-	0.720	0.972	
1.019	-	1.056	-	-	0.516		
1.003	-	1.015	-	-	0.506		
-1.550	-	-3.844	-	-	-1.971		
0.814	0.828	-	0.523				
0.799	0.816	-	0.510				
-1.822	-1.393	-	-2.526				

Rel. Diff.	
Max	2.85%
Min	-6.21%
RMS	2.11%

BEAVRS
MCS
Rel. Diff. (%)

Figure V-34: Radial detector signal for BERA Cycle 2 at BOC (EDPF = 124.25 days).

Figure V-35 table — BEAVRS / MCS / Rel. Diff. (%)

1	2	3	4	5	6	7	8
-	1.031	1.042	1.053	1.124	1.028	1.001	0.762
-	1.033	1.033	1.053	1.155	1.024	1.004	0.758
-	0.170	-0.890	0.005	2.738	-0.352	0.312	-0.577
1.031	1.035	1.067	1.184	1.090	-	1.022	0.794
1.033	1.029	1.062	1.203	1.101	-	1.006	0.770
0.170	-0.553	-0.489	1.569	1.029	-	-1.607	-3.031
1.042	1.071	1.219	-	1.259	1.069	-	0.712
1.033	1.053	1.220	-	1.256	1.049	-	0.689
-0.890	-1.691	0.047	-	-0.236	-1.909	-	-3.163
1.053	-	1.080	1.317	-	1.221	-	0.556
1.053	-	1.058	1.284	-	1.225	-	0.523
0.005	-	-2.082	-2.481	-	0.331	-	-5.895
1.124	1.086	-	-	1.209	1.070	0.791	
1.155	1.083	-	-	1.201	1.064	0.807	
2.738	-0.279	-	-	-0.683	-0.540	2.015	
1.028	-	-	1.230	-	0.884	0.527	
1.024	-	-	1.228	-	0.884	0.523	
-0.352	-	-	-0.142	-	-0.041	-0.840	
1.001	-	1.051	-	-	0.538		
1.004	-	1.033	-	-	0.531		
0.312	-	-1.708	-	-	-1.295		
0.762	0.783	-	0.547				
0.758	0.770	-	0.545				
-0.577	-1.713	-	-0.387				

Rel. Diff.	
Max	2.74%
Min	-5.89%
RMS	1.65%

BEAVRS
MCS
Rel. Diff. (%)

Figure V-35: Radial detector signal for BERA Cycle 2 at BOC (EDPF = 248.06 days).

The pin-wise power, flux, fuel temperature, coolant density at BOC, EOC, and EOC are shown in the Figure V-36. The local quantity tally results look reasonable proving that the capability of MCS Cycle simulation.
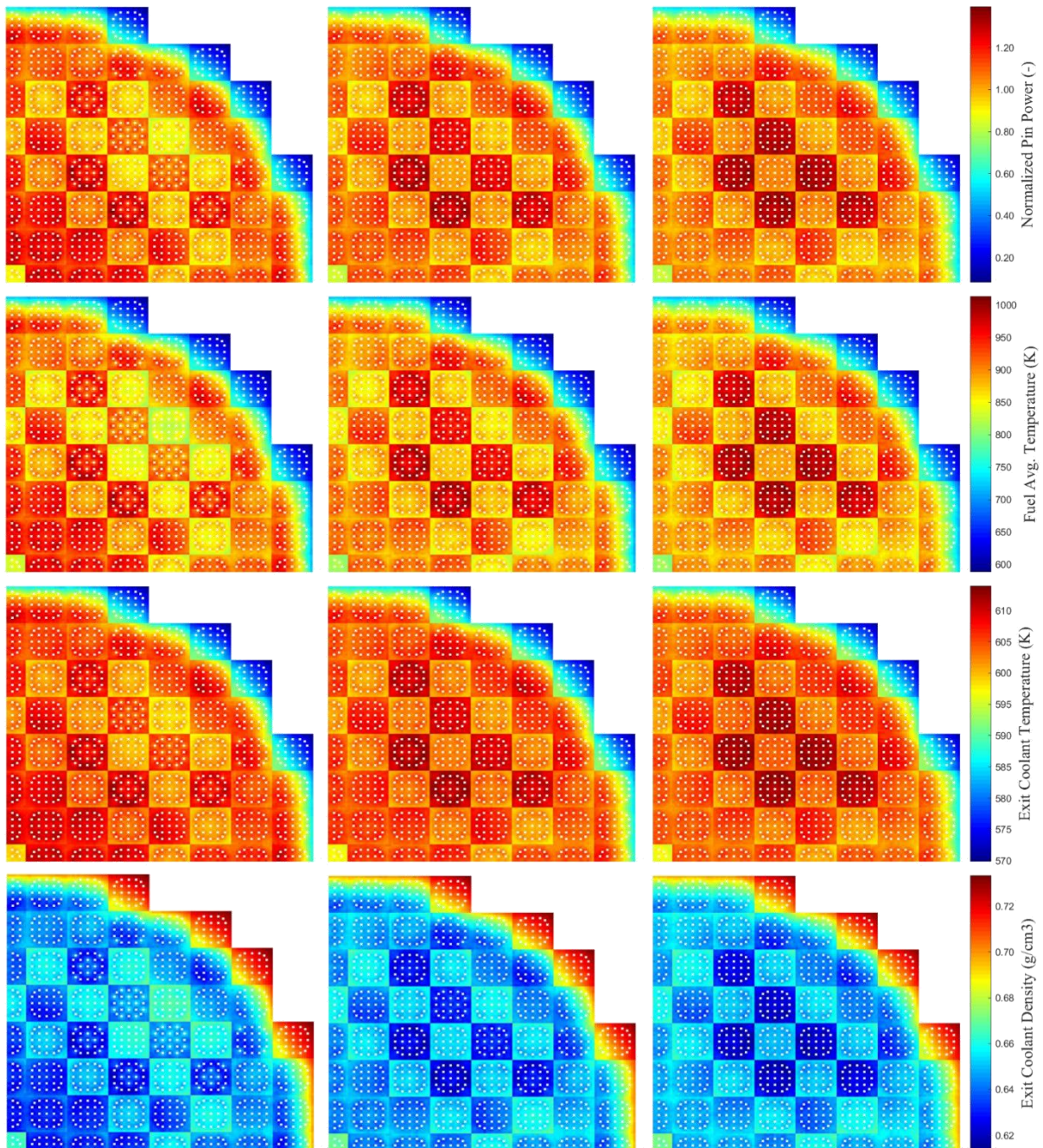

Figure V-36: Pin power, fuel average temperature, exit coolant temperature and exit coolant density for BEAVRS Cycle 2 at BOC, MOC, and EOC.

VI. Conclusion

The goal of this thesis was to develop a new Monte Carlo code MCS for power reactor simulation to extended the applications of Monte Carlo code on practical working station. In this thesis, the features and performance of MCS were discussed showing the capability and high efficiency solving large-scale multiphysics problem. The feasibility of using Monte Carlo code for power reactor application was examined in this study, and it was demonstrated that it is possible to calculated Cycle solution with 1-2% standard including critical boron concentration, assembly power, axial power, radial detector signal.

In section II, the general capabilities of MCS was overviewed. The common features required for neutron transport capability including transport kernel, collision kernel, depletion kernel was described and tested against various benchmark cases: ICSBEP benchmark, INDC benchmark, Doppler defect benchmark, BEAVRS benchmark. The parallel performance of MCS was demonstrated against BEAVRS benchmark Cycle 1 at end of cycle incorporation with feedbacks including thermal hydraulics, depletion, and equilibrium xenon. The parallel efficiency was tested up to 1,120 processors, and the efficiency was over 90 %. The tally performed of MCS was also demonstrated against Monte Carlo performance benchmark up to 13M tally bins. The overhead of tally bin searching time was 1%, and the overhead of adding one tally quantity was about 0.5%.

In section III, the inter-cycle correlation of Monte Carlo simulation for high dominance problem was studied. The variance bias due to inter-cycle correlation was overviewed, and the model to estimate the variance bias when subcycle method is adopted was developed and tested. It was estimated that 120 subcycles are required to reduce variance bias less than 5% when solving BEAVRS benchmark. Then, it was confirmed that the standard deviation of assembly-wise power converges following ideal slope proving that the inter-cycle correlation is almost removed.

In section IV, the feedbacks required for the power reactor simulation was discussed one by one. The CRAM burnup solver was adopted and tested against VERA benchmark by comparing the result of Serpent Monte Carlo code. The unphysical oscillation induced from by statistical uncertainty of xenon number density was discussed and it was studied that the equilibrium xenon feedback helps to prevent this phenomenon. For the temperature dependent cross section generation, Windowed multipole represent module was adopted for resolved resonance energy range together with on-the-fly interpolation function for the thermal scattering and probability table. The implemented functions were tested by comparing cross sections from pre-processed data by NJOY. At last, Thermal hydraulics solver TH1D was implemented and the feedback strategy was discussed. It was tested against VERA benchmark problem 6 by comparing MC21 and MPACT solution.

In section V, the sensitivity study was performed to decide the calculation condition of Monte Carlo power reactor simulation. It was shown that it requires at least 15 burnup steps, 20 axial meshes should

be used to have converged solution. The overestimation of variance was found during sensitivity study, and it was studied. Monte Carlo results tends to overestimate the variance due to feedbacks over transport cycles. Among various size of meshes, the core average axial distribution showed largest overestimation ratio, and the ratio increased as burnup progresses. Finally, the power reactor simulation was demonstrated against BEAVRS benchmark Cycle 1 and Cycle 2 simulation. The critical boron concentration, assembly power, core average axial distribution, and detector signal were compared. The critical boron concentration showed good agreement within 40 ppm against measurement data. The radial detector signal also showed good agreement comparing measurement within RMS error of 1-3%.

Reference

[1] M. Herman, and A. Trkov, ENDF-6 Formats Manual, ENDF-102/BNL-90365, 2009.

[2] D. W. Muir, R. M. Boisourt, and A. C. Kahler, The NJOY nuclear data processing system, Version 2012, Los Alamos National Laboratory, 2012.

[3] K. Smith, "High Performance Computing Challenges Encountered in High-Resolution Reactor Core Simulation," *Plenary Talk 1 in M&C 2017*, Jeju, Korea, April 16-20, 2017.

[4] K. Smith and B. Forget, "Challenges in the Development of High-Fidelity LWR Core Neutronics Tools," *Proc. M&C,* Sun Valley, Idaho, May 5-9, 2013.

[5] D. Kropaczek, "CASL: Achievements in Addressing Challenges Facing the Light Water Reactor Industry," *Plenary Talk 4 in M&C 2017*, Jeju, Korea, April 16-20, 2017.

[6] "Consortium for Advanced Simulation of Light Water Reactors (CASL)," http://www.casl.gov/.

[7] B. Kochunas, B. Collins, D. Jabaay, et al., "VERA Core Simulator Methodology for PWR Cycle Depletion," *Proc. M&C*, Nashville, TN, April 19-23, 2015.

[8] S.G. Stimpson, J.J. Poweres, K.T. Clarno, "Assessment of Pellt-Clad Interation Indicators in Watts Bar Unit 1, Cycles 1-3 using VERA," Proc. PHYSOR, Sun valley, ID, May 1-5, 2016.

[9] F. Franceschini, D.A. Salazar, M. Ouisloumen, et al, "AP1000 PWR Cycle 1 HFP Depletion Simulations with VERA-CS," Proc. PHYSOR, Sun valley, ID, May 1-5, 2016.

[10] T. Goorley, M. James, T. Booth, et al., "Initial MCNP6 Release Overview," Nuclear Technology, 180:3, 298-315, 2012.

[11] J. Leppänen, M. Pusa, T. Viitanen, et al., "The Serpent Monte Carlo Code: Status, Development and Applications in 2013," Annals of Nuclear Energy, vol. 82, 142-150, 2015.

[12] H.J. Shim, et al., "McCARD: Monte Carlo Code for Advanced Reactor Design and Analysis," Nuclear Engineering and Technology, 44:2, doi: http://dx.doi.org/10.5516/NET.01.2012.503, 2012

[13] P. K. Romano and B. Forget, "The OpenMC Monte Carlo Particle Transport Code," Annals of Nuclear Energy, vol. 51, 274-291, 2013.

[14] H. Lee, C. Kong, and D. Lee, "Status of Monte Carlo Code Development at UNIST," *proc. PHYSOR*, Kyoto, Japan, September 28 – October 3, 2014.

[15] H. Lee, W. Kim, P. Zhang, et al., "Preliminary Simulation Results of BEAVRS Three-dimensional Cycle 1 Wholecore Depletion by UNIST Monte Carlo Code MCS," *proc. M&C*, Jeju, Korea, April 16-20, 2017.

[16] Forrest B. Brown, "Fundamentals of Monte Carlo Particle Transport," LA-UR-05-4983.

[17] F.B. Brown, Y. Nagaya, "The MCNP5 Random Number Generator," *Trans. American Nuclear Society*, Nov. 17-21, 2002.

[18] F.B. Brown, "Random Number Generation with Arbitrary Strides," *Trans. Am. Nucl. Soc.* 71, 202,

1994.

[19] M. Herman, and A. Trkov, ENDF-6 Formats Manual, ENDF-102/BNL-90365, 2009.

[20] D. W. Muir, R. M. Boisourt, and A. C. Kahler, The NJOY nuclear data processing system, Version 2012, Los Alamos National Laboratory, 2012.

[21] X-5 Monte Carlo Team, "MCNP – A General Monte Carlo N-Particle Transport Code Version 5," Los Alamos National Laboratory, 2005.

[22] D. Lee, K. Smith, and J. Rhodes, "The Impact of 238U Resonance Elastic Scattering Approximations on Thermal Reactor Doppler Reactivity," Annals of Nuclear Energy, 36, 274-280, 2009.

[23] B. Becker, et al., "Improvement of the Resonance Scattering Treatment in MCNP in View of HTR Calculations," Annals of Nuclear Energy, 36, 281-285, 2009.

[24] L.B. Levitt, "The Probability Table Method for Treating Unresolved Neutron Resonance in Monte Carlo Calculations," Nuclear Science and Engineering, 49, 450-457, 1972

[25] F.B. Brown, "On the Use of Shannon Entropy of the Fission Distribution for Assessing Convergence of Monte Carlo Criticality Calculations," *Proc. ANS Topical Meeting on Reactor Physics*, Vancouver, British Columbia, Canada, September 10–14, 2006.

[26] International Handbook of Evaluated Criticality Safety Benchmark Experiments, NEA/NCS/DOC(95)03/IV, 2014.

[27] D.E. Cullen, R.N. Blomquist, C. Dean, et al., "How Accurate Can We Calculate Thermal Systems?," INDC(USA)-107, International Nuclear Data Committee, 2004.

[28] R.D. Mosteller, "The Doppler-Defect Benchmark: Overview and Summary of Results," *Proc. M&C*, Monterey, California, April 15-19, 2007.

[29] N. Horelik, B. Herman, B. Forget, and K. Smith, "Benchmark for Evaluation and Validation of Reactor Simulations (BEAVRS), v1.0.1," *proc. M&C 2013*, Sun Valley, Idaho, 2013.

[30] Z. Wang, B. Wu, L. Hao, et al., "Validation of SuperMC with BEAVRS Benchmark at Hot Zero Power Condition,*" Annals of Nuclear Energy*, 111, 709-714, 2018.

[31] D.J. Kelly, et al., "Analysis of Select BEAVRS PWR Benchmark Cycle 1 Resuts Using MC21 and OpenMC," *Proc. PHYSOR*, Kyoto, Japan, Sep. 28-Oct 3, 2014.

[32] P.K. Romano and B. Forget, "Parallel Fission Bank Algorithms in Monte Carlo Criticality Calculations," *Nuclear Science and Engineering*, 170, 125-135, 2012.

[33] D. She, K. Wang, J. Sun, et al., "Improved Methods of Handling Massive Tallies in Reactor Monte Carlo Code RMC," *Proc. M&C*, Sun Valley, Idaho, May 5-9, 2013.

[34] P.K. Romano, B. Forget, "The OpenMC Monte Carlo Particle Transport Code," *Annals of Nuclear Energy*, 51, 274-281, 2013.

[35] D.M. Lax, "Memory Efficient Indexing Algorithm for Physical Properties in OpenMC," Master

Thesis, MIT, 2015.

[36] J.E. Hoogenboom, W.R. Martin, and B. Petrovic, "The Monte Carlo Performance Benchmark Test – Aims, Specifications and First Results," *Proc. M&C*, Rio de Janeiro, Brazil, May 8-12, 2011.

[37] T. Goorley, M. James, T. Booth, et al., "Initial MCNP6 Release Overview," *Nuclear Technology*, 180:3, 298-315, doi: https://doi.org/10.13182/NT11-135, 2012.

[38] E.M. Gelbard and R.E. Prael, "Monte Carlo Work at Argonne National Laboratory," ANL-75-2 (NEACRP-L-118), p. 220, Argonne National Laboratory, 1974.

[39] R.J. Brissenden and A.R. Garlick, "Biases in the Estimation of Keff and Its Error by Monte Carlo Methods," *Annals of Nuclear Energy*, 13, 63, 1986.

[40] E.M. Gelbard and R.E. Prael, "Computation of Standard Deviation in Eigenvalue Calculations," *Progress in Nuclear Energy*, 24, 237, 1990.

[41] T. Ueki, T. Mori, and M. Nakagawa, "Error Estimations and Their Biases in Monte Carlo Eigenvalue Calculations," *Nuclear Science and Engineering*, 125, 1, 1997.

[42] H.J. Shim and C.H. Kim, "Real Variance Estimation Using an Intercycle Fission Source Correlation for Monte Carlo Eigenvalue Calculations," *Nuclear Science and Engineering*, 162, 2009.

[43] J. Miao, B. Forget, and K. Smith, "Analysis of Correlations and Their Impact on Convergence Rates in Monte Carlo Eigenvalue Simulations," *Annals of Nuclear Energy*, 92, 81-95, 2016.

[44] B.R. Herman, "Monte Carlo and Thermal Hydraulic Coupling using Low-Order Nonlinear Diffusion Acceleration," Ph.D. thesis, MIT, 2014.

[45] M.J. Lee, "Monte Carlo Method with Coarse Mesh Finite Difference Formulation for Efficient Power Reactor Analysis," Ph.D. thesis, Seoul National University, 2013.

[46] H. Lee and D. Lee, "Application of CMFD with Superhistory Method on Continuous Energy Monte Carlo Simulation for Eigenvalue Problems," *Proc. M&C*, Nashville, TN, April 19-23, 2015.

[47] Lulu Li, "Acceleration Methods for Monte Carlo Particle Transport Simulations," Ph.D. thesis, MIT, 2017.

[48] A.T. Godfrey, "VERA Core Physics Benchmark Progression Problem Specifications (Rev. 2)," Tech. Rep. CASL-U-2012-0131-002, Oak Ridge National Laboratory, (2013).

[49] J. Dufek and J.E. Hoogenboom, "Numerical Stability of Existing Monte Carlo Burnup Codes in Cycle Calculations of Critical Reactors," *Nuclear Science and Engineering*, 162, 307-311, 2009.

[50] D.P. Griesheimer, "In-Line Xenon Convergence Algorithm for Monte Carlo Reactor Calculations," *PHYSIR 2010,* Pittsburgh, Pensylvania, Usa, May, 9-14, 2010.

[51] F. Yang, G. Wang, G. Yu, and K. Wang, "Implementation of Inline Equilibrium Xenon Method in RMC Code," *PHYSOR 2016*, Sun Valley, ID, May 1-5, 2016.

[52] C. Josey, P. Ducru, B. Forget., and K. Smith, "Windowed Multipole for Cross Section Doppler

Broadening," *Journal of Computational Physics*, 2015.

[53] R. N. Hwang, "A Rigorous Pole Representation of Multilevel Cross sections and Its Practical Applications," Nuclear Science and Engineering, 96: 129-209, 1987.

[54] M. Ryu, Y.S. Jung, H.H. Cho, and H.G. J, "Solution of the BEAVRS Benchmark using the nTRACER Direct Whole Core Calculation Code," *Journal of Nuclear Science and Technology*, 52, 961-969, 2015.

[55] M. Vazquez, H.Tsige-Tamirat, L. Ammirabile, and F. Martin-Fuertes, "Coupled Neutronics Thermal hydraulics Analysis Using Monte Carlo and Sub-Channel Codes," *Nuclear Engineering and Design*, 250, 403-411, 2012.

[56] M. Ellis, B. Forget, K. Smith, and D. Gaston, "Preliminary Coupling of the Monte Carlo Code OpenMC and the Multiphysics Object-Oriented Simulation Environment (MOOSE) for Analyzing Doppler Feedback in Monte Carlo Simulations," *Proc. M&C*, Nashville, Tennessee, April 19-23, 2015.

[57] B.N. Aviles, D.J. Kelly, D.L. Aumiler, et al., "MC21/COBRA-IE and VERA-CS Multiphysics Solutions to VERA Core Physics Benchmark Problem #6," *Progress in Nuclear Energy*, 101, 338-351, 2017.

[58] S. Palmtag, "Coupled Single Assembly Solution with VERA (problem 6), Rev 1," Technical Report: CASL-U-2013-0140-001, 2013.

[59] A. Ivanov, V. Sanchez, R. Strieglitz, K. Ivanov, "Large-Scale Monte Carlo Neutron Transport Calculations with Thermal-Hydraulic Feedback," *Annals of Nuclear Energy*, 84, 204-219, 2015.

[60] M.N. Avramova, "CTF:A Thermal Hydraulic Sub-Channel Code for LWR Transient Analysis," User's Manual, Pennsylvania State University, February 2009.

[61] J. Choe, S. Choi, P. Zhang, et al., "Verification and Validation of STREAM/RAST-K for PWR analysis," Nuclear Engineering and Technology, doi: https://doi.org/10.1016/j.net.2018.10.004, 2018.

[62] B.S. Collins, A. Godfrey, S. Stimpson, S. Palmtag, "Simulation of the BEAVRS Benchmark Using VERA," *Proc. M&C*, Jeju, Korea, April 16-20, 2017.

Acknowledgements (in Korean)

Curriculum Vitae

Name: Hyunsuk Lee

Data of Birth: January 20, 1990

EDUCATION

2009.03 – 2013.02: B.S. Nuclear Engineering & Thermo-Fluid & Power Engineering, UNIST
2013.03 – 2019.02: Combined M.D./Ph.D. Nuclear Engineering, UNIST

PUBLICATIONS

SCI(E) JOURNAL

1. **Hyunsuk Lee**, Sooyoung Choi, and Deokjung Lee*, "A Hybrid Monte Carlo/Method-of-Characteristics Method for Efficient Neutron Transport Analysis," Nucl. **Sci**. Eng., 180 (1) pp.69-85, http://dx.doi.org/10.13182/NSE13-102 (2015)

2. **Hyunsuk Lee**, Sooyoung Choi, Kyoon-Ho Cha, Kwangho Lee, and Deokjung Lee*, "New Calculational Model for Self-Powered Neutron Detector Based on Monte Carlo Simulation," J. Nucl. Sci. Tech., http://dx.doi.org/10.1080/00223131.2014.975766 (2015)

3. Peng Zhang, **Hyunsuk Lee**, Chidong Kong, Jiwon Choe, Jiankai Yu, Farrokh Khoshahval, Deokjung Lee*, "Practical Monte Carlo Simulation Using Modified Power Method with Preconditioning," Ann. Nucl. Energy, Accepted for publication (2018)

4. Jinsu Park, Peng Zhang, **Hyunsuk Lee**, Sooyoung Choi, Jiankai Yu, Deokjung Lee*, "Performance Evaluation of CMFD on Inter-Cycle Correlation Reduction of Monte Carlo Simulation," Comput. Phys. Commun., 235: 11-119, https://doi.org/10.1016/j.cpc.2018.09.014 (2018)

5. Tuan Quoc Tran, Sanggeol Jeong, Khang Nhat Hoang Nguyen, **Hyunsuk Lee**, Sooyoung Choi, Peng Zhang, Min Jae Lee, Jae-Yong Lim, Deokjung Lee*, "Validation of the MCNP6 code for SFR shielding design analysis," J. Radiol. Prot., 39: 11-37, https://doi.org/10.1088/1361-6498/aae323 (2018)

6. Jiankai Yu, **Hyunsuk Lee**, Hanjoo Kim, Peng Zhang, Deokjung Lee*, "Preliminary Coupling of the Thermal/Hydraulic Solvers in the Monte Carlo Code MCS for Practical LWR Analysis", Ann. Nucl. Energy, 118: 317-335, http://doi.org/10.1016/j.anucene.2018.03.043 (2018)

7. Matthieu Lemaire, **Hyunsuk Lee**, Bamidele Ebiwonjumi, Chidong Kong, Wonkyeong Kim, Yunki Jo, Jinsu Park, Deokjung Lee*, "Verification of Photon Transport Capability of UNIST Monte Carlo Code MCS", Comput. Phys. Commun., 231: 1-18, http://doi.org/10.1016/j.cpc.2018.05.008 (2018)

8. Jaerim Jang, Wonkyeong Kim, Sanggeol Jeong, Eun Jeong, Jinsu Park, Matthieu Lemaire, **Hyunsuk Lee**, Yongmin Jo, Peng Zhang, Deokjung Lee*, "Validation of UNIST Monte Carlo Code MCS for Criticality Safety Analysis of PWR Spent Fuel Pool and Storage Cask," Annals of Nuclear Energy, 114: 495-509. https://doi.org/10.1016/j.anucene.2017.12.054 (2018)

9. Peng Zhang, **Hyunsuk Lee**, Deokjung Lee*, "On the Transfer Matrix of the Modified Power Method," Comput. Phys. Commun., 222: 102-112. https://doi.org/10.1016/j.cpc.2017.09.022 (2018)

10. Peng Zhang, **Hyunsuk Lee**, Deokjung Lee*, "Extension of the Noise Propagation Matrix Method for Higher Mode Solutions," J. Comput. Phys., Published Online. http://dx.doi.org/10.1016/j.jcp.2017.05.007 (2017)

11. Matthieu Lemaire, **Hyunsuk Lee**, Nam-il Tak, Hyun Chul Lee, Deokjung Lee*, "Multi-physics steady state analysis of OECD/NEA Modular High Temperature Gas-cooled Reactor MHTGR-350," J. Nucl. Sci. Technol., Published Online. http://dx.doi.org/10.1080/00223131.2017.1299649 (2017)

12. Jinsu Park, **Hyunsuk Lee**, Taewoo Tak, Ho Cheol Shin, Deokjung Lee*, "Physics Study of Canada Deuterium Uranium Lattice with Coolant Void Reactivity Analysis," Nucl. Eng. Tech., 49 (1): 6-16. http://dx.doi.org/10.1016/j.net.2016.07.003 (2017)

13. Peng Zhang, **Hyunsuk Lee**, Deokjung Lee*, "Calculation of Degenerated Eigenmodes with Modified Power Method," Nucl. Eng. Tech., 49 (1): 17-28. http://dx.doi.org/10.1016/j.net.2016.08.009 (2017)

14. Chidong Kong, **Hyunsuk Lee**, Taewoo Tak, Deokjung Lee*, Si Hwan Kim, Seokjean Lyou, "Accuracy Improvement of Boron Meter Adopting New Fitting Function and Multi-detector", Nucl. Eng. Tech., Published Online. http://dx.doi.org/10.1016/j.net.2016.06.012 (2016)

15. Peng Zhang, **Hyunsuk Lee**, and Deokjung Lee*, "Extension of Modified Power Method to Two-Dimensional Problems," J. Comput. Phys., http://dx.doi.org/doi 10.1016/j.jcp.2016.05.024 (2016)

16. Peng Zhang, **Hyunsuk Lee**, and Deokjung Lee* "A General Solution Strategy of Modified Power Method for Higher Mode Solutions," J. Comput. Phys., 305:387-402 http://dx.doi.org/doi:10.1016/j.jcp.2015.10.042 (2016)

17. Sooyoung Choi, **Hyunsuk Lee**, Ser Gi Hong, and Deokjung Lee*, "Resonance Self-Shielding Methodology of New Neutron Transport Code STREAM," J. Nucl. Sci. Technol., 52(9):1133-1150, http://dx.doi.org/10.1080/00223131.2014.993738, (2015)

PROCEEDING CONFERENCE

1. **Hyunsuk Lee**, Wonkyeong Kim, Peng Zhang, Azamat Khassenov, Jinsu Park, Jiankai Yu, Sooyoung Choi, Hwan Soo Lee and Deokjung Lee*, "Preliminary Simulation Results of BEAVRS Three-dimensional Cycle 1 Wholecore Depletion by UNIST Monte Carlo Code MCS," M&C2017, Jeju, Korea, April 16-20 (2017) [Oral Presentation]

2. **Hyunsuk Lee**, and Deokjung Lee*, "Application of CMFD with Wielandt Method on Continuous Energy Monte Carlo Simulation for Eigenvalue Problems," ANS MC2015, Nashville, TN, USA, April 19-23 (2015)

3. **Hyunsuk Lee**, Chidong Kong, and Deokjung Lee*, "Status of Monte Carlo Code Development at UNIST," PHYSOR2014, Kyoto, Japan, September 28 October 3 (2014) [Oral Presentation]

4. **LEE Hyunsuk**, CHOI Sooyoung, KIM Si Hwan, LYOU Seokjean, and LEE Deokjung *, "Development of MCNPX Model for Boronometer," International Symposium on Symbiotic Nuclear Power Systems for the 21st Century (ISSNP2013), November 22-24, Beijing, China (2013) [Oral Presentation]

5. **Hyunsuk Lee** and Deokjung Lee *, "Hybrid Method of Deterministic and Probabilistic Approaches for Continuous Energy Neutron Transport Problem," M&C2013, Sun Valley, USA, May (2013) [Oral Presentation]

CONFERENCE

1. **Hyunsuk Lee,** Eun Jeong, Hocheol Lee, Hyun Chul Lee, Deokjung Lee*, "Verification of MCS VHTR Modeling Capability," RPHA17, Chengdu, Sichuan, China, August 24-25 (2017) [Oral presentation]
2. **Hyunsuk Lee**, Deokjung Lee, Peng Zhang, and Azamat Khassenov, "Preliminary Solution of BEAVRS Hot Full Power at BOC by Monte Carlo Code" KNS Fall Meeting, Gyeongju, Korea, October 26-28 (2016)
3. **Hyunsuk Lee**, Wonkyeong Kim, Peng Zhang, Azamat Khassenov, Yunki Jo, and Deokjung Lee,"Development Status of Monte Carlo Code at UNIST",KNS   2016 spring, Jeju, Korea, May 11-13 (2016)
4. **Hyunsuk Lee**, Azamat Khassenov, Peng Zhang, and Deokjung Lee*, "Computational Approaches to Large-scale/complex Nuclear Reactor Analysis," CPMMS2016, Bangkok, Thailand, January 24-26 (2016)
5. **Hyunsuk Lee** and Deokjung Lee, Performance Evaluation of CMFD with Superhistory Method on Continuous Energy Monte Carlo Eigenvalue Simulation, KNS Spring Meeting, Jeju, Korea, May 6-8 (2015)
6. **Hyunsuk Lee** and Deokjung Lee*, "Application of CMFD on Continuous Energy Monte Carlo Simulation for Eigenvalue Problems," KNS Fall Meeting, Pyeongchang, Korea, October 30-31 (2014) [Oral Presentation]
7. **Hyunsuk Lee**, Chidong Kong, and Deokjung Lee*, "A New Monte Carlo Neutron Transport Code at UNIST," KNS Spring Meeting, Jeju Convention Center, May 28-30 (2014) [Oral Presentation]
8. **Hyunsuk Lee**, Sooyoung Choi, and Deokjung Lee*, "Development of Boron Meter Model with MCNPX," KNS Fall Meeting, Kyeongju, October (2013) [Oral Presentation]
9. **Hyunsuk Lee** and Deokjung Lee*, "Application of Analytic Slowingdown Kernel for MOC-MC Hybrid Method," ANS Winter Meeting, Washington D.C., November (2013) [Oral Presentation]
10. **Hyunsuk Lee**, Si Hwan Kim, Seokjean Lyou, and Deokjung Lee *, "Performance Evaluation of Boronometer based on MCNPX Model," ANS Winter Meeting, Washington D.C., November (2013) [Oral Presentation]
11. **Hyunsuk Lee**, Chidong Kong, Sooyoung Choi, and Deokjung Lee *, "Hybrid Method of MOC and MC for Efficient Continuous Energy Neutron Transport Analysis," ANS Annual Meeting, Atlanta, GA, June (2013) [Oral Presentation]

PATENT

1. Deokjung Lee, Wonkyeong Kim, Sooyoung Choi, **Hyunsuk Lee**, "Hybrid Depletion Method for Light Water Reactor Analysis," KOR patent: 10-2017-0059904 (2017)
2. Deokjung Lee et al., "보론미터(Boron Meter)," KOR patent: 1014625040000, NOV., 11 (2014)